

**UCGE Reports  
Number 20117**

**Department of Geomatics Engineering**

**Development of A Precision  
Pointing System Using an  
Integrated Multi-Sensor  
Approach**

**By**

**Robert Shaw Harvey**

April, 1998



Calgary, Alberta, Canada

THE UNIVERSITY OF CALGARY

**Development of a Precision Pointing System Using an Integrated Multi-Sensor  
Approach**

by

Robert Shaw Harvey

A THESIS

SUBMITTED TO THE FACULTY OF GRADUATE STUDIES  
IN PARTIAL FULFILMENT OF THE REQUIREMENTS FOR THE  
DEGREE OF MASTER OF SCIENCE

DEPARTMENT OF GEOMATICS ENGINEERING

CALGARY, ALBERTA

APRIL, 1998

© Robert Shaw Harvey 1998

THE UNIVERSITY OF CALGARY

## ABSTRACT

The purpose of this research was to improve on existing GPS dual-antenna baseline systems for the purpose of determining the azimuth and pitch of a vehicle in post-mission. The system developed was unique in that the software architecture followed an aided sensor approach and the orientation parameters were related directly to the GPS carrier phase measurements as opposed to a GPS derived position vector. The sensor array included a fixed baseline GPS dual-antenna system, a fiber-optic gyro, an electronic compass and tilt meter. The combination of non-GPS sensors was unique and was chosen to provide, at a minimum, the information necessary to maintain the azimuth and pitch without GPS. The system was tested under suburban conditions with a 0.919 metre inter-antenna baseline length and provided accuracies of  $0.66^\circ$  rms in azimuth and  $1.51^\circ$  in pitch when compared to an accurate GPS/INS reference. The filter results were compared to the individual sensor results over the test and proven superior. The ability of the integrated system to maintain a solution over long periods of induced GPS outage in the suburban test was also demonstrated.

## ACKNOWLEDGEMENTS

First, I would like to express my gratitude to my supervisor, Dr. Elizabeth Cannon. Her continuous guidance and encouragement are greatly appreciated. Without her support, both academic and financial, this thesis would not have been possible.

Second, I would like to thank my friends and fellow graduate students, Jamie Henriksen, Thom Morley, Susan Skone, Huanqui Sun and Shawn Weisenburger to name a few, who made everything seem to make sense. John Raquet is especially thanked for his time and patience in discussions relating to a variety of my “short questions”.

Third, I would like to thank Dr. K.P. Schwarz for the generous loan of the INS/GPS system used to generate the reference trajectory during testing. Alex Bruton is also thanked for his support of the INS/GPS system during the testing phase and his processing of the reference data using Kingspad™.

Fourth, I would like to thank Jim Stephen and Craig Glennie for helping with the initial data collection and for not going crazy as we drove in small circles attempting to calibrate the electronic compass.

Fifth, and most of all, I would like to thank my parents, Ria and Stuart. More than anything else in my life, they have been a constant source of support, encouragement and inspiration. I could not have gotten this far without them.

## TABLE OF CONTENTS

APPROVAL PAGE .....	ii
ABSTRACT .....	iii
ACKNOWLEDGEMENTS .....	iv
TABLE OF CONTENTS .....	v
LIST OF TABLES .....	viii
LIST OF FIGURES .....	ix
NOTATION .....	xvi
 CHAPTER	
1.0 INTRODUCTION .....	1
.....	
1.1 Background and Objectives .....	1
1.2 Thesis Outline .....	6
2.0 KALMAN FILTER .....	8
2.1 The Linear Discrete Kalman Filter .....	8
.....	
2.2 Discrete Kalman Filter with Linearized Measurement Model .....	12
2.3 Inertial Sensor Aiding .....	15
2.4 Quality Control .....	17
3.0 GLOBAL POSITIONING SYSTEM (GPS) OVERVIEW .....	20
3.1 GPS System Architecture .....	20
3.2 GPS Observables .....	21
3.3 Differenced GPS Observables .....	23
.....	
3.4 Interferometric Techniques for Orientation .....	27
3.5 GPS Error Sources .....	31

3.5.1	Selective Availability .....	32
3.5.2	Ionospheric Propagation Errors .....	33
3.5.3	Tropospheric Propagation Errors .....	35
3.5.4	Multipath and Receiver Measurement Noise Errors .....	35
4.0	GPS CARRIER PHASE AMBIGUITY RESOLUTION .....	38
4.1	GPS Ambiguity Resolution for Attitude Applications .....	39
4.1.1	Ambiguity Search Space and Primary Satellites .....	40
4.1.2	Determination of Primary Ambiguity Sets .....	43
4.1.3	Testing of Primary Ambiguity Sets .....	46
4.2	Aided Ambiguity Resolution .....	48
5.0	SENSOR DESCRIPTIONS .....	51
5.1	Andrew AUTOGYRO™ .....	52
.....		
5.1.1	Andrew AUTOGYRO™ Temperature Effects .....	55
5.1.2	Misalignment of FOG Plane with Horizontal Plane .....	57
5.2	Precision Navigation Inc. TCM2-50 .....	62
5.2.1	Electronic Compass .....	64
5.2.2	Tilt Meter .....	66
6.0	SYSTEM REALIZATION .....	68
6.1	Hardware Architecture .....	68
6.2	Software Architecture .....	73
6.2.1	Estimation of Vehicle Position and Velocity using GPS .....	76
6.2.2	Kalman Filter Measurement and Dynamic Models .....	78
7.0	TEST RESULTS .....	86
7.1	Test Description .....	86
7.2	Individual Sensor Performance .....	89
7.2.1	GPS-Only Results Using HEAD™ .....	90
7.2.2	Andrew Autogyro™ Results .....	91
7.2.3	Precision Navigation Inc. TCM2-50 Results .....	93
7.3	Effect of GPS Acceleration Corrections on Tilt Meter Output .....	96

7.4	Integrated Filter Results .....	101
7.4.1	Suburban GPS Coverage .....	104
7.4.2	Suburban GPS Coverage with Periodic 200 s GPS Outages..	110
7.4.3	Suburban GPS Coverage with Long-Term GPS Outage .....	116
7.4.4	Suburban GPS Coverage using a 25° and 35° Mask Angle	121
8.0	CONCLUSIONS AND RECOMMENDATIONS .....	125
	REFERENCES .....	129
	APPENDIX .....	136

## LIST OF TABLES

Table 3.1 – Spatially correlated and satellite dependent error sources .....	31
Table 3.2 – Receiver and local environment dependent errors .....	32
Table 5.1 – Andrew Autogyro™ 3ARG-D specifications .....	53
Table 5.2 – Precision Navigation TCM2-50 Specifications .....	63
Table 7.1 – GPS-Only error statistics for HEAD™ .....	90
Table 7.2 – Precision Navigation TCM2-50 error statistics .....	93
Table 7.3 – TCM2 pitch and roll error statistics for 180 s test period, before and after applying a GPS derived correction for acceleration .....	99
Table 7.4 – TCM2 pitch and roll error statistics for full test period, before and after applying a GPS derived correction for acceleration .....	100
Table 7.5 – Adaptive scheme for integrated filter spectral densities .....	102
Table 7.6 – Integrated filter azimuth and pitch error statistics for suburban run .....	105
Table 7.7 – Integrated filter azimuth and pitch error statistics for suburban run with 200 s periodic GPS outages .....	111
Table 7.8 – Comparison of raw compass error versus filter error when using the compass and gyro to estimate azimuth, after GPS time 340000 s .....	117





Figure 5.4 – Direction cosine representation of FOG spin axis ( $\omega_{fog}$ ) for a roll angle of $\Delta\phi$ and a pitch angle of $\Delta\theta$	59
.....	
Figure 5.5 – Angular displacement error over 1.0 s period given a misalignment angle ( $\gamma$ ) and assuming equal pitch and roll angular rates ( $\omega$ )	61
.....	
Figure 5.6 – Induced horizontal reference error ( $\eta$ ) due to vehicle accelerations	66
.....	
Figure 6.1 – Pin assignment for Andrew Autogyro™ DB-9 interface	69
.....	
Figure 6.2 – Pin assignment for Precision Navigation TCM2-50 connector	70
.....	
Figure 6.3 – Equipment diagram showing the four sensors and two PCs	71
.....	
Figure 6.4 – Sensor array rigidly mounted on a test vehicle	72
.....	
Figure 6.5 – Mark-time input cable wiring diagram for determining offset between PC clock and GPS time using parallel port strobe pin	73
.....	
Figure 6.6 – Software architecture with extended Kalman filter	75
.....	
Figure 6.7 – Mathematical model for nominal azimuth error ( $\delta\psi$ ) and pitch error ( $\delta\theta$ ) for the case of GPS measurements ( $z_{GPS}$ )	81
.....	
Figure 6.8 – Mathematical model for nominal azimuth error ( $\delta\psi$ ) and magnetic field error ( $\epsilon_{mag}$ ) for the case of a compass measurement ( $z_{cm}$ )	82
.....	
Figure 7.1 – Trajectory of suburban test in NW Calgary, Alberta, Canada in October 1997. Test duration about 40 minutes	87

.....	
Figure 7.2 – Truth values for vehicle azimuth from GPS/INS reference	88
.....	
Figure 7.3 – Truth values for vehicle roll and pitch from GPS/INS reference	88
.....	
Figure 7.4 – Number of visible satellites above 15° elevation mask angle along with PDOP for suburban test run	89
.....	
Figure 7.5 – GPS-Only azimuth and pitch errors for HEAD™	91
.....	
Figure 7.6 – Integrated raw Autogyro™ output using Hayashi (1996) scale factor polynomial versus current polynomial	92
.....	
Figure 7.7 – Comparison of TCM2 compass error with magnetic anomaly detector (MAD) enabled and disabled	94
.....	
Figure 7.8 – Roll and pitch error for TCM2 tilt meter	94
.....	
Figure 7.9 – Autocorrelation of TCM2 compass error	95
.....	
Figure 7.10 – Raw TCM2 pitch error and acceleration based correction using GPS- only and the GPS/INS reference	97
.....	
Figure 7.11 – Raw TCM2 roll error and acceleration based correction using GPS- only and the GPS/INS reference	97
.....	
Figure 7.12 – TCM2 roll and pitch error after GPS acceleration correction	98
.....	
Figure 7.13 – Effectiveness of GPS acceleration based correction at removing low- frequency error in TCM2 tilt meter measurements	100

.....	
Figure 7.14 – Integrated filter azimuth and pitch error results, including $3\sigma$ error envelope for suburban run	104
.....	
Figure 7.15 – Integrated filter estimated gyro rate bias error, including $3\sigma$ error envelope (top) and result of applying estimated bias to raw gyro output (bottom)	106
.....	
Figure 7.16 – Integrated filter estimated magnetic field error, including $3\sigma$ error envelope (top) and comparison of estimated error vs. true compass error (bottom)	107
.....	
Figure 7.17 – Innovation test statistic $T_k$ for integrated filter during suburban run ..	108
Figure 7.18 – Maximum azimuth and pitch errors resulting from a measurement blunder not detected by the innovation sequence test	109
.....	
Figure 7.19 – Maximum gyro rate bias and magnetic field errors resulting from a measurement blunder not detected by the innovation sequence test	110
....	
Figure 7.20 – Integrated filter azimuth and pitch error results including $3\sigma$ error envelope for suburban run with 200 s periodic GPS outages	111
.....	
Figure 7.21 – Integrated filter estimated gyro rate bias error, including $3\sigma$ error envelope (top) and result of applying estimated bias to raw gyro output (bottom)	112
.....	
Figure 7.22 – Integrated filter estimated magnetic field error, including $3\sigma$ error envelope (top) and comparison of estimated error vs. true compass error (bottom)	113

.....  
Figure 7.23 – Innovation test statistic  $T_k$  for integrated filter during suburban run  
with 200 s periodic GPS outages 114

.....  
Figure 7.24 – Maximum azimuth and pitch errors resulting from a measurement  
blunder not detected by the innovation sequence test (200 s periodic  
GPS outages) 115

.....  
Figure 7.25 – Maximum gyro rate bias and magnetic field errors resulting from a  
single undetected measurement blunder (200 s periodic GPS outages) 115

Figure 7.26 – Integrated filter azimuth and pitch error results including  $3\sigma$  error  
envelope for suburban run with no GPS after 340000 s 116

.....  
Figure 7.27 – Integrated filter estimated gyro rate bias error, including  $3\sigma$  error  
envelope (top) and result of applying estimated bias to raw gyro  
output (bottom) 118

.....  
Figure 7.28 – Integrated filter estimated magnetic field error, including  $3\sigma$  error  
envelope (top) and comparison of estimated error vs. true compass  
error (bottom) 119

.....  
Figure 7.29 – Innovation test statistic  $T_k$  for integrated filter during suburban run  
with no GPS after 340000 s 120

.....  
Figure 7.30 – Maximum azimuth and pitch errors resulting from a measurement  
blunder not detected by the innovation sequence test (no GPS after  
340000 s) 120

.....  
Figure 7.31 - Maximum gyro rate bias and magnetic field errors resulting from a  
measurement blunder not detected by the innovation sequence test

(no GPS after 340000 s) .....	121
Figure 7.32 – Number of visible satellites above 25° mask angle	122
Figure 7.33 – Integrated filter azimuth and pitch error results, including 3σ error envelope for suburban run and 25° mask angle.	123
Figure 7.34 – Number of visible satellites above 35° mask angle	124
Figure 7.35 – Integrated filter azimuth and pitch error results, including 3σ error envelope for suburban run and 35° mask angle.	124

## NOTATION

### Symbols

$\mathbf{a}_n$	Net acceleration experienced by liquid in tilt meter
$\mathbf{a}_v$	Component of tilt meter net acceleration ( $\mathbf{a}_n$ ) due to vehicle acceleration
$\alpha$	Inverse of time constant for pitch error <b>or</b> significance level
$b$	GPS inter-antenna baseline length
$\mathbf{b}$	baseline vector in local level
$\beta$	Inverse of time constant for magnetic field error <b>or</b> significance level
$c$	Speed of light in a vacuum
$\mathbf{C}_{v,k}$	Covariance of innovation sequence
$\chi^2(v,\alpha)$	Chi- squared test for $v$ degrees of freedom and an $\alpha$ significance level
$D$	Scaling factor for FOG rate bias error used in filter
$d_{\text{fog}}$	FOG rate measurement bias
$d_{\text{ion}}$	Error due to ionospheric effects
$d_{\text{trop}}$	Error due to tropospheric effects
$dt$	GPS satellite clock error
$dT$	GPS receiver clock error
$\hat{\mathbf{d}}_k$	Estimated vector of least squares corrections to parameters
$\delta_o$	Non-centrality parameter used in external reliability
$\delta\psi$	Error in nominal azimuth estimated by filter
$\delta\theta$	Error in nominal pitch estimated by filter
$\delta d_{\text{fog}}$	FOG rate bias error estimated by filter
$\Delta\theta_{\text{tcm}}$	Tilt meter pitch measurement
$\Delta\phi_{\text{tcm}}$	Tilt meter roll measurement
$\mathbf{e}^i$	Unit vector from receiver to $i^{\text{th}}$ satellite
$\epsilon_{\text{mag}}$	Compass magnetic field error estimated by filter
$\eta$	Tilt meter error due to vehicle acceleration

<b>F</b>	Dynamics matrix
<b>g</b>	Component of tilt meter net acceleration ( $\mathbf{a}_n$ ) due to gravity
<b>G</b>	Noise shaping filter
$\gamma$	Misalignment angle between FOG spin axis and vertical axis in LL
$H_0$	Null hypothesis
$H_a$	Alternate hypothesis
$\mathbf{h}(\mathbf{x}_0)$	Non-linear measurement relation evaluated at $\mathbf{x}_0$
<b>H<sub>k</sub></b>	Design matrix
<b>I</b>	Identity matrix
$k$	time subscript
<b>K<sub>k</sub></b>	Kalman gain matrix
$\lambda$	GPS L1 carrier phase wavelength (~ 19.02 cm)
$\Lambda$	Longitude of user location
$m_k$	Number of degrees of freedom, equal to number of observations
$N$	GPS carrier phase integer ambiguity
<b>N</b>	Normal matrix
$\nabla_{k,i}$	Internal reliability measure, used to calculate MDB
$\nabla_{X_{k,i}}$	External reliability measure, used to calculate ME
$\nu$	number of degrees of freedom, equal to number of measurements minus number of parameters
$\omega_\psi$	Azimuth rotation rate
$\omega_\phi$	Roll rotation rate
$\omega_\theta$	Pitch rotation rate
$\omega_{\text{fog}}$	Rotation rate in plane of FOG
$\omega_{\text{raw}}$	Raw rate measurement from FOG
<b>P<sub>k</sub></b>	Covariance matrix of parameters
$p$	GPS pseudorange measurement
$\rho$	True range from satellite to receiver
$\phi$	GPS carrier phase measurement <b>or</b> roll

$\hat{f}$	GPS Doppler measurement
$\psi$	Azimuth of system in LL frame
$\Psi_{\text{nom}}$	Nominal azimuth value generated from integrated FOG rates
$\Phi_L$	Latitude of user location
$\Phi_k$	Transition matrix
$q$	Spectral density for individual states
$\mathbf{Q}_k$	Process noise matrix
$\mathbf{Q}(\tau)$	Spectral density matrix
$\mathbf{r}$	Baseline vector in ECEF
$\hat{\mathbf{r}}$	Estimated measurement residuals
$\mathbf{R}_k$	Measurement covariance matrix
$s$	FOG temperature dependent scale factor
$\hat{\mathbf{S}}_2^o$	Estimated variance factor
$\mathbf{T}$	Rotation matrix from ECEF to LL
$T_k$	Test statistic for innovation sequence testing
$\theta$	Pitch of system in LL frame
$\theta_{\text{nom}}$	Nominal pitch value generated from tilt meter measurement
$\mathbf{u}$	Unity white noise sequence
$\mathbf{v}_k$	Innovation sequence <b>or</b> additive white noise process in measurement model
$\mathbf{w}_k$	Misclosure vector <b>or</b> additive white noise process in dynamics model
$w$	White noise sequence for individual states
$\mathbf{x}_o$	Approximate point used for linearization in Taylor series
$\mathbf{x}$	state vector of parameters
$\hat{\mathbf{x}}_k$	estimated state vector
$\tilde{\mathbf{x}}_k$	error in estimated state vector
$\mathbf{z}_k$	vector of measurements

## Operators

Matrices are bold and capitalized

Vectors are bold and lower-case

Using  $\mathbf{x}$  as a dummy variable, the remaining operators are given as :

$\Delta\mathbf{x}$  is a single difference of  $\mathbf{x}$  between receivers

$\nabla\mathbf{x}$  is a single difference of  $\mathbf{x}$  between satellites

$\nabla\Delta\mathbf{x}$  is a double difference of  $\mathbf{x}$  between satellites and receivers

$\mathbf{x}^{(+)}$  denotes a filter value that has been updated with measurements

$\mathbf{x}^{(-)}$  denotes a filter value that has been projected ahead

$\hat{\mathbf{x}}$  denotes the filter estimate of  $\mathbf{x}$

$\dot{\mathbf{x}}$  denotes a time derivative

$\frac{\partial\mathbf{x}}{\partial y}$  represents the derivative of  $\mathbf{x}$  with respect to  $y$

$\mathbf{X}^T$  is the transpose of  $\mathbf{X}$

$\mathbf{X}^{-1}$  is the inverse of  $\mathbf{X}$

## Acronyms

2DRMS	95% horizontal positioning accuracy, two multiplied by distance root mean squared
AS	Anti-spoofing
C/A	Coarse acquisition code
DGPS	Differential GPS
DOP	Dilution of precision
ECEF	Earth-centered, Earth-fixed reference frame
EKF	Extended Kalman filter
FOG	Fiber-optic gyro
GPS	Global Positioning System
INS	Inertial Navigation System
L1	Civilian GPS frequency 1575.42 MHz
L2	Military GPS frequency 1227.60 MHz
LL	Local level reference frame
MAD	Magnetic anomaly detector
MDB	Minimum detectable blunder
ME	Maximum error
P	Precise code
PDOP	Positional dilution of precision
PRN	Pseudo random noise code
RPDOP	Relative positional dilution of precision
SA	Selective availability
SPS	Standard positioning service
TEC	Total electron content
URE	User equivalent range error

# CHAPTER 1

## INTRODUCTION

### 1.1 Background and Objectives

Traditionally, precise determination of the orientation of a platform was accomplished using expensive inertial navigation systems (INS). These systems have excellent short-term accuracy but are limited in the long-term by gyro drift and accelerometer biases which, when integrated over time, result in long-term systematic error (Siouris, 1993). This error growth can be limited by aiding the inertial system with additional sensors such as the Global Positioning System (GPS) which have better long-term stability. Aiding an INS using GPS is known as GPS/INS integration wherein INS solution and sensor errors are periodically updated based on GPS derived position and velocity (Schwarz and Wei, 1997). The GPS is an all-weather satellite based radionavigation system designed to provide 24 hour worldwide position information to an unlimited number of users. Parkinson (1994) describes the GPS history and architecture in detail while Wells et al. (1987) and Hofmann-Wellenhof et al. (1994) describe the various GPS measurement observables and their application to the positioning problem.

More recently, it has been demonstrated that the signals received by three or more non-collinear GPS antennas rigidly mounted to a platform can be used to directly estimate attitude (Cohen, 1992). In situations where the high short-term accuracy and data rate of the INS are not required, a GPS attitude determination system can be used instead of an INS for a fraction of the cost. GPS attitude systems have been successfully applied under a wide variety of conditions. These include airborne applications as demonstrated by Cannon et al. (1994) and Kruczynski (1995) and space-borne satellite systems as developed by Cohen (1992) and Chesley and Axelrad (1994). Lu et al. (1993) and

Lachapelle et al. (1994) showed that GPS could be used for shipborne attitude applications while Schwarz et al. (1992) and Dumaine (1996) have successfully applied GPS to vehicular applications.

There are two methods for determining attitude parameters from GPS. The measurements can be used to determine relative antenna positions from which attitude parameters are then derived (position approach), or the measurements can be used to estimate the attitude parameters directly (direct approach). Lu (1995) describes the development of a GPS multi-antenna attitude system that uses the position approach to determine attitude parameters. The direct approach is described in Van Graas and Braasch (1991) and Howell and Tang (1995). El-Mowafy (1994) uses the direct approach and also describes the effect of baseline length and various antenna configurations on GPS attitude determination. Schleppe (1996) presents a robust quaternion attitude parameterization for the direct approach and points out its distinct advantages over the position approach.

The use of GPS dual-antenna, single baseline systems for determining the azimuth and pitch of a platform has also been examined. GPS dual-antenna pointing systems are easier to implement than full attitude systems due to the reduced number of measurements and parameters. They are also less expensive since less hardware is required. Dual-antenna systems can be used as pointing devices in a wide variety of applications to determine a directional vector. Jurgens et al. (1991) proposed a GPS dual-antenna system for the purpose of determining the azimuth and pitch of an artillery piece. Gilkey et al. (1995) described the development of a dual-antenna system using low-cost off-the-shelf receivers for similar applications. Cannon et al. (1992) developed a real-time system for an autonomous vehicle using a dual-antenna GPS system as the primary sensor. Cannon and Haverland (1993) integrated a dual-antenna GPS pointing system with an Attitude and Heading Reference System (AHRS) in a helipod. Vinnins and Gallop (1997) discuss the use of a very short baseline ( $< 95$  cm) dual-antenna system for determining the azimuth and pitch of an air-dropped Arctic in-ice sonobouy. More

recently, a dedicated single receiver dual-antenna pointing system was developed for shipborne applications by NovAtel Inc. (Ford et al., 1997).

Unfortunately, GPS orientation systems have two inherent limitations. First, they are susceptible to satellite line-of-sight blockage and second, since they almost always make use of the precise but ambiguous GPS carrier phase measurement, the unknown integer carrier phase ambiguities must be resolved (Cannon et al., 1992). The GPS carrier phase ambiguity arises since the receiver can only measure the fractional part of the carrier phase, leaving an unknown integer number of cycles between the receiver and satellite.

Resolution of the carrier phase ambiguities is complicated by possible movement of the platform, requiring more complex on-the-fly (OTF) techniques (Chen and Lachapelle, 1994). The carrier wavelength is also fairly small (19.02 cm) resulting in a large number of possible ambiguity sets for a given spatial uncertainty. Fortunately, GPS orientation systems can take advantage of the fact that the baseline length between antennas can be assumed fixed if the platform is rigid enough. This restriction when applied to a series of potential ambiguity sets can significantly decrease ambiguity resolution time (Hatch, 1990). The concept of baseline constraint ambiguity resolution for the case of a moving platform is discussed in Cohen (1992) and Euler and Hill (1995). Lu (1995) and El-Mowafy (1994) present a number of ambiguity resolution variations for the case of multiple antennas and various antenna configurations.

To bridge GPS coverage gaps and reduce the possibility of selecting an incorrect ambiguity set, inexpensive sensors can be integrated with the GPS orientation system, similar to GPS/INS integration but at greatly reduced cost. An acceptable level of solution confidence can then be maintained through periods when GPS carrier phase ambiguities cannot be determined or GPS is not available at all. In Gilkey et al. (1995), a clinometer is used to provide an approximate elevation angle for ambiguity resolution. Chesley and Axelrad (1994) augmented a satellite GPS attitude system with sun sensors

and fiber-optic gyros. In Cannon et al. (1992), a dual-antenna GPS system was integrated with a compass, rate gyros, odometer and altimeter. Hayward et al. (1997) developed an Attitude Heading Reference System (AHRS) based on a three-antenna GPS system and a triad of inexpensive solid state gyros.

The algorithm most often used for optimally estimating a series of parameters based on redundant sensor data is a Kalman filter, described in detail by Gelb (1974) and Brown and Hwang (1992). Since improper estimation of the orientation parameters could have dire consequences, it is important to monitor filter performance. Quality control in Kalman filtering is most often based on testing a series of predicted measurement residuals, known as the innovation sequence. A good description of quality control in dynamic systems using the innovation sequence is given in Teunissen (1990). Based on Teunissen, quality control and reliability for the case of kinematic GPS positioning is investigated by Lu and Lachapelle (1990) and Abousalem (1993). In the critical area of aircraft navigation, significant effort has been poured into quality control in the form of Receiver Autonomous Integrity Monitoring (RAIM) as discussed in Van Graas and Farrel (1993) and Van Graas (1996). The application of augmented or multiple filters and adaptive process noise to the quality control problem is discussed in McBurney (1990) as well as Brown and Hwang (1992). Improvements to the conventional testing techniques have also been investigated (Gao, 1992) to develop more robust systems although they can be significantly more complicated.

The purpose of this research is to build on previous work completed at the University of Calgary using GPS dual-antenna pointing systems. Currently all of these systems use the position approach to determine the attitude parameters. A new system is desired which uses the direct approach to determine orientation parameters and also combines a minimum of redundant external sensor data to aid in ambiguity resolution and bridge GPS coverage gaps.

The objective of this research is to develop and test an integrated multi-sensor system to determine the azimuth and pitch of a land vehicle in post-mission. The sensor array is comprised of a 1 metre fixed baseline, GPS dual-antenna system augmented with a fiber-optic gyro, an electronic compass and a tilt meter. The choice of non-GPS sensors is based on availability, low cost and the ability to provide information regarding both the pitch and azimuth of the vehicle when GPS is not available. The fiber-optic gyro, used to measure the azimuth rotation rate, has high short-term accuracy but suffers from long-term drift. To complement the fiber-optic gyro, a compass is included to provide good long-term azimuth information. The tilt meter provides estimates of pitch and roll referenced to the surface of a conducting liquid. Errors due to movement of the liquid with respect to the horizon plane caused by vehicle accelerations are reduced using GPS derived corrections. This particular combination of sensors has not been applied to the pointing problem previously. The fiber-optic gyro has been used in previous research at The University of Calgary for aiding GPS positioning but the tilt meter and compass, packaged together, are entirely new.

The software architecture follows an aided sensor approach using a Kalman filter to optimally estimate system errors. GPS carrier phase integer ambiguity resolution makes use of the low-cost sensor information to restrict the size of the ambiguity search space resulting in fewer possible ambiguity sets and shorter time to resolution. Filter performance is monitored with an innovation sequence testing procedure, primarily for the purpose of detecting incorrect GPS carrier phase ambiguities. The effectiveness of the system is examined by comparing test results with an accurate independent GPS/INS reference. The ability of the integrated system to maintain an orientation solution without GPS is also examined.

## 1.2 Thesis Outline

Chapter 2 of this thesis examines the algorithms and basic assumptions of the linear discrete Kalman filter as applied to navigation problems. Kalman filtering for the case of a linearized measurement model will also be discussed. The concept of aiding an inertially derived trajectory with external measurements is introduced for the case of feed-forward and feed-back implementations. A statistical testing procedure for quality control is presented along with the concepts of internal and external reliability.

Chapter 3 introduces the Global Positioning System (GPS) starting with an overview the system architecture as developed by the United States Department of Defense. The different GPS observables, including pseudorange, carrier phase and Doppler, are defined along with their measurement equations. The concept of differencing GPS observables to reduce or eliminate various error sources is examined along with GPS interferometric techniques for attitude applications. A discussion of GPS error sources will conclude the chapter.

Chapter 4 presents a GPS carrier phase ambiguity resolution algorithm for fixed baseline orientation applications. The definition of the ambiguity search space, determination of the potential ambiguity sets and a least-squares estimation procedure for isolating the correct ambiguity set are all presented in detail. The concept of using external sensor information for reducing the size of the ambiguity search space is also discussed.

Chapter 5 introduces the remaining sensors, including a fiber-optic gyro, an electronic compass and a bubble level tilt-meter. The possible error sources for each sensor are also examined.

Chapter 6 describes the realization of the integrated system. The hardware architecture for data logging and time tagging of the data is presented along with the physical

description of the mounting system. The dynamic error and measurement models used in the Kalman filter to estimate the orientation of the platform are derived. The determination of the vehicle position and velocity using a GPS single-point solution is also discussed.

Chapter 7 presents the results of a test using the integrated system compared to a precise GPS/INS reference. The performance and error characteristics of the individual sensors are examined in detail. The filter parameters are defined and explained. The integrated filter results for the test run are presented along with the results of the statistical testing and the external reliability. Results for the case of induced long-term and periodic GPS outages in the data are also presented for the integrated filter.

Finally, Chapter 8 will summarize the results, present conclusions and make recommendations for future work.

## CHAPTER 2

### KALMAN FILTER

Modern navigation systems must estimate the location and/or orientation of a platform based on information from a variety of different sensors. The types of sensors used is dependent on the application but, in general, they can be expected to measure or monitor different physical quantities and possess varying levels of accuracy. The difficulty resides in combining these various and often redundant data streams in an efficient and optimal fashion. This remained a problem until Kalman (1960) developed a time-recursive algorithm, known as a Kalman filter, to combine redundant sensor data based on a measurement and a dynamic model. If the dynamic and measurement noise sequences can be fully described as zero-mean Gaussian white noise sequences then the Kalman filter is the optimal estimator in a linear minimum variance (LMV) sense (Gelb, 1974). It has therefore been adopted for application to the sensors used in this thesis. The following sections describe the Kalman filter that is implemented in Chapter 6.

#### 2.1 The Linear Discrete Kalman Filter

A Kalman Filter is an algorithm to estimate the state of a system based on knowledge of the system dynamics and a series of measurements corrupted by noise. The system dynamics can be described by a series of differential equations of the form

$$\dot{\mathbf{x}} = \mathbf{F}\mathbf{x} + \mathbf{G}\mathbf{u} \tag{2.1}$$

where,  $\mathbf{x}$  is the vector of state variables

$\mathbf{F}$  is a dynamics matrix

$\mathbf{G}$  is a type of shaping filter

and  $\mathbf{u}$  is a zero-mean Gaussian white noise sequence.

The state-space solution for equation (2.1) can be written as a function of time ( $t$ ) as (Brown and Hwang, 1992)

$$\mathbf{x}(t_{k+1}) = \Phi(t_{k+1}, t_k)\mathbf{x}(t_k) + \int_{t_k}^{t_{k+1}} \Phi(t_{k+1}, t)\mathbf{G}(t)\mathbf{u}(t)dt \quad (2.2)$$

or in the form of a discrete case difference equation with abbreviated notation as

$$\mathbf{x}_{k+1} = \Phi_k \mathbf{x}_k + \mathbf{w}_k \quad (2.3)$$

where  $\Phi_k$  is the transition matrix and  $\mathbf{w}_k$  is the effect due to the random forcing function  $\mathbf{G}\mathbf{u}$  in equation (2.1). The transition matrix is calculated using the inverse Laplace transform ( $\mathcal{L}^{-1}[f(s)]$ ) as (Gelb, 1974)

$$\Phi_k = \mathcal{L}^{-1} \left\{ [s\mathbf{I} - \mathbf{F}]^{-1} \right\}_{t=\Delta t} \quad (2.4)$$

where  $\mathbf{I}$  is an identity matrix. Measurements can be considered as linear combinations of the system states corrupted by measurement noise

$$\mathbf{z}_k = \mathbf{H}_k \mathbf{x}_k + \mathbf{v}_k \quad (2.5)$$

where,  $\mathbf{z}_k$  is the vector of measurements at time  $k$

$\mathbf{H}_k$  is a design matrix relating the measurements to the system states  $\mathbf{x}_k$

and  $\mathbf{v}_k$  represents random measurement error.

The sequences  $\mathbf{w}_k$  and  $\mathbf{v}_k$  are assumed to be zero-mean, Gaussian and white with statistics

$$E[\mathbf{w}_k] = E[\mathbf{v}_k] = 0 \quad (2.6)$$

$$E[\mathbf{w}_k \mathbf{w}_i^T] = \begin{cases} \mathbf{Q}_k & i = k \\ 0 & i \neq k \end{cases} \quad (2.7)$$

$$E[\mathbf{v}_k \mathbf{v}_i^T] = \begin{cases} \mathbf{R}_k & i = k \\ 0 & i \neq k \end{cases} \quad (2.8)$$

$$E[\mathbf{w}_k \mathbf{v}_i^T] = 0 \quad (2.9)$$

where,  $\mathbf{Q}_k$  is the process noise covariance matrix and  $\mathbf{R}_k$  is the covariance of the measurement errors. For uncorrelated measurements, the  $\mathbf{R}_k$  matrix reduces to a diagonal positive definite matrix. The covariance  $\mathbf{Q}_k$  due to process noise is calculated by taking the expectation of the second term on the right hand side of equation (2.2). Based on the assumption that the noise sequence  $\mathbf{u}(t)$  is white, the covariance calculation can be reduced to the form (Gelb, 1974)

$$\mathbf{Q}_k = \int_{t_k}^{t_{k+1}} \Phi(t_{k+1}, t) \mathbf{G}(t) \mathbf{Q}(t) \mathbf{G}^T(t) \Phi^T(t_{k+1}, t) dt \quad (2.10)$$

where,  $\mathbf{Q}(t)$  is a spectral density matrix, not to be confused with  $\mathbf{Q}_k$  which is a covariance matrix. Obtaining the optimal estimates ( $\hat{\mathbf{x}}_k$ ) of the system states ( $\mathbf{x}_k$ ) in a linear minimum variance sense involves minimizing the covariance matrix ( $\mathbf{P}_k$ ) of the estimation error ( $\tilde{\mathbf{x}}_k$ ) where

$$\tilde{\mathbf{x}}_k = \hat{\mathbf{x}}_k - \mathbf{x}_k \quad (2.11)$$

$$\text{and } \mathbf{P}_k = E[\tilde{\mathbf{x}}_k \tilde{\mathbf{x}}_k^T]. \quad (2.12)$$

Kalman (1960) is credited with the first formulation of this estimation procedure which is well presented in Brown and Hwang (1992) and Gelb (1974). The algorithm, now known

as the Kalman filter, is comprised of a prediction stage based on the dynamic model and an update stage based on the measurement model. The update equations which combine a predicted estimate with the measurements are based on the blending factor  $\mathbf{K}_k$ , known as the Kalman gain. The estimates after prediction are denoted by superscript (-) and after update by superscript (+). The Kalman filter algorithm is given in Figure 2.1 for the case of a linear discrete system (Brown and Hwang, 1992)

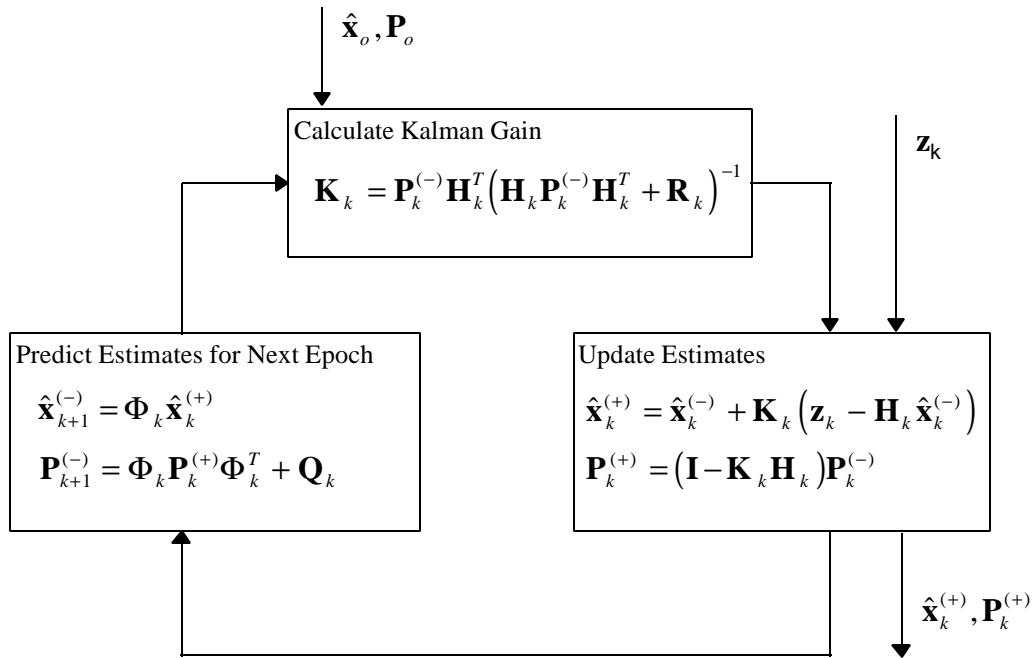


**Figure 2.1 - Linear discrete Kalman filter algorithm.**

The notation for Figure 2.1 is given as,

- $\hat{\mathbf{x}}_k$  is the estimated state vector
- $\Phi_k$  is the transition matrix
- $\mathbf{P}_k$  is the covariance matrix of the estimation error
- $\mathbf{Q}_k$  is the process noise matrix

- $\mathbf{K}_k$  is the Kalman gain matrix
- $\mathbf{H}_k$  is the design matrix
- $\mathbf{R}_k$  is the measurement error covariance
- $\mathbf{I}$  is the identity matrix and
- $\mathbf{z}_k$  is the vector of measurements.

This discrete formulation of the Kalman filter equations is generally too restrictive for the majority of navigation problems because the dynamic and measurement models must be linear. In the majority of navigation problems the measurement model is non-linear and must be expressed as a Taylor series approximation around a point of expansion. The result, as will be shown later, is that the design matrix becomes a function of the expansion point which is usually dependent on the unknown vehicle dynamics. The case for the linearized measurement model is described next.

## 2.2 Discrete Kalman Filter with Linearized Measurement Model

It is common in navigation problems to have a non-linear measurement model that must be linearized before being implemented in a Kalman filter. The non-linear continuous form of the measurement model can be written similar to equation (2.5) as (Brown and Hwang, 1992)

$$\mathbf{z} = \mathbf{h}(\hat{\mathbf{x}}, t) + \mathbf{v}(t) \tag{2.13}$$

where,  $\mathbf{z}$  is the vector of measurements

$\hat{\mathbf{x}}$  is the optimal estimate of the parameters

$\mathbf{v}$  is a zero-mean, Gaussian white noise sequence

and  $\mathbf{h}$  is a non-linear function of the parameters ( $\hat{\mathbf{x}}$ ) and time ( $t$ ).

A set of linear measurement equations can be derived by expanding equation (2.13) about an approximate point ( $\mathbf{x}_o$ ) using a Taylor series and truncating the higher order terms.

$$\mathbf{z} = \mathbf{h}(\mathbf{x}_o, t) + \left[ \frac{\partial \mathbf{h}}{\partial \mathbf{x}} \right]_{\mathbf{x}=\mathbf{x}_o} (\hat{\mathbf{x}} - \mathbf{x}_o) + \mathbf{v}(t) \quad (2.14)$$

The quantity being filtered then becomes the estimated correction ( $\hat{\mathbf{d}}$ ) to the approximate point ( $\mathbf{x}_o$ ) given as

$$\hat{\mathbf{d}} = \hat{\mathbf{x}} - \mathbf{x}_o \quad (2.15)$$

where it is assumed that the corrections are small enough that the higher order terms ignored in equation (2.14) are insignificant. Rearranging and substituting equation (2.15) in equation (2.14) results in

$$\mathbf{z} - \mathbf{h}(\mathbf{x}_o, t) = \left[ \frac{\partial \mathbf{h}}{\partial \mathbf{x}} \right]_{\mathbf{x}=\mathbf{x}_o} \hat{\mathbf{d}} + \mathbf{v}(t) \quad (2.16)$$

The measurement input to the filter, given on the left side of equation (2.16), is then the raw measurement minus the function  $\mathbf{h}$  evaluated at the approximate point  $\mathbf{x}_o$ . The discrete form of equation (2.16) can be written as

$$\mathbf{z}_k - \mathbf{h}(\mathbf{x}_o) = \mathbf{H}_k |_{x_o} \hat{\mathbf{d}}_k + \mathbf{v}_k \quad (2.17)$$

where the linearized design matrix is given as

$$\mathbf{H}_k |_{x_o} = \left[ \frac{\partial \mathbf{h}}{\partial \mathbf{x}} \right]_{\mathbf{x}=\mathbf{x}_o} \quad (2.18)$$

For the case of linear dynamics the differential equations for the corrections are the same as for the total quantities (Brown and Hwang, 1992) and the  $\Phi_k$  matrix can be calculated as described in section 2.1. The measurement input to a filter with a linearized measurement model is called the misclosure vector ( $\mathbf{w}$ ), not to be confused with the dynamic noise sequence used to generate the process noise matrix ( $\mathbf{Q}_k$ ), and is given as

$$\mathbf{w} = \mathbf{h}(\mathbf{x}_o) - \mathbf{z}_k. \quad (2.19)$$

The full equations for the Kalman filter with a linearized measurement model are given in Krakiwsky (1990) as

**Prediction**  $\hat{\mathbf{d}}_{k+1}^{(-)} = \Phi_k \hat{\mathbf{d}}_k^{(+)} \quad (2.20)$

$$\mathbf{P}_{k+1}^{(-)} = \Phi_k \mathbf{P}_k^{(+)} \Phi_k^T + \mathbf{Q}_k \quad (2.21)$$

**Update**  $\mathbf{K}_k = \mathbf{P}_k^{(-)} \mathbf{H}_k^T (\mathbf{H}_k \mathbf{P}_k^{(-)} \mathbf{H}_k^T + \mathbf{R}_k)^{-1} \quad (2.22)$

$$\hat{\mathbf{d}}_k^{(+)} = \hat{\mathbf{d}}_k^{(-)} - \mathbf{K}_k (\mathbf{w}_k - \mathbf{H}_k \hat{\mathbf{d}}_k^{(-)}) \quad (2.23)$$

$$\mathbf{P}_k^{(+)} = (\mathbf{I} - \mathbf{K}_k \mathbf{H}_k) \mathbf{P}_k^{(-)}. \quad (2.24)$$

For vehicle navigation purposes the approximate point of expansion is usually a time varying nominal trajectory ( $\mathbf{x}_o(t)$ ). If the nominal trajectory used for expansion is generated independent of the filter output, the resulting filter is known as a linearized Kalman filter. If the nominal trajectory is updated using filter state estimates the filter is known as an extended Kalman filter (EKF). The Kalman filter is seen to be recursive in the time domain and easily implemented into a computer program on a modern PC.

### 2.3 Inertial Sensor Aiding

The concept of sensor aiding is based on estimating the errors in an inertially based system by comparison with another navigation aid such as GPS. Inertial systems have good short term accuracy characteristics but are subject to long term effects such as gyro drift and integration error. The cost of a stand-alone inertial system that can maintain a good navigation solution for periods of a couple of hours with no external information is prohibitive, about \$100,000 to \$200,000 (Geier, 1996). By combining a less expensive inertial system with sensors that have good long term characteristics it is possible to generate navigation solution accuracies of a similar level but at a fraction of the cost. The combination of these two data streams is an optimal estimation problem ideally suited for a Kalman filter. The feed-forward version of the inertial sensor aiding concept is shown in Figure 2.2 (Brown and Hwang, 1992).

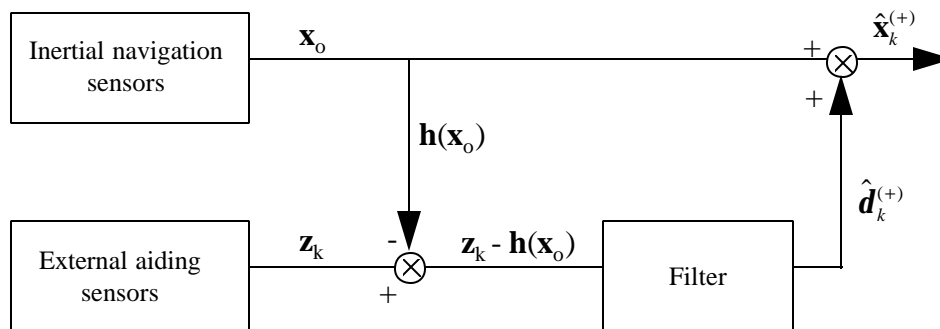


**Figure 2.2 - Feed-forward external aiding implementation.**

The feed-forward sensor aiding configuration is a linearized Kalman filter, wherein the filter estimates corrections to the inertially generated trajectory which are then applied to the navigation output. The sequence  $\mathbf{h}(\mathbf{x}_0)$  represents a series of predicted measurements generated by evaluating the function  $\mathbf{h}$  using the nominal trajectory  $\mathbf{x}_0$ . Note in the summation prior to the filter that the inertial measurement stream and the external aiding

sensor measurement stream are differenced, effectively removing the majority of the vehicle dynamics. The quantity passed to the filter is a combination of inertial sensor error, aiding sensor error and imperfections or limitations in the dynamic model.

If raw measurements ( $\mathbf{z}_k$ ) from the external aiding sensors are directly differenced with the predicted measurements ( $\mathbf{h}(\mathbf{x}_o)$ ) the filter is referred to as a tightly coupled filter. If the measurements from the external aiding sensors are preprocessed and given in the parameter space before differencing then the filter is a loosely coupled filter. If the inertial trajectory can be expected to drift significantly from the true trajectory, the Taylor series linearization may start to be dominated by the higher order terms which are not included in the measurement model. These non-linear effects will cause the filter result to be sub-optimal and possibly divergent. The solution is to use an EKF where the inertial trajectory is adjusted by the current predicted error estimate which is subsequently set to zero ( Since after adjusting the trajectory the predicted error is zero by definition ). This is known as the feed-back configuration and is shown in Figure 2.3 (Brown and Hwang, 1992).

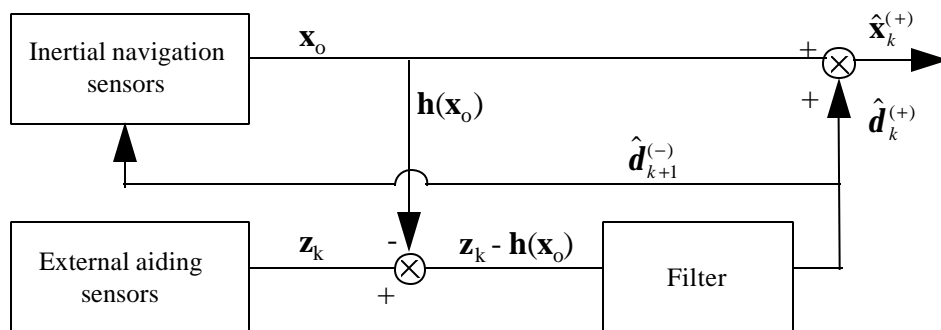


**Figure 2.3 - Feed-back external aiding implementation.**

A concern when using an EKF is that if the filter for some reason fails and generates a faulty error estimate which is subsequently applied to the inertial trajectory, the inertial system output will be corrupted from that point onwards.

## 2.4 Quality Control

The objective of kinematic system quality control in this research is the detection of possible measurement blunders. A property of the Kalman filter is that if the input noise sequences are zero-mean, Gaussian and white then the innovation sequence ( $\mathbf{v}_k$ ), not to be confused with the measurement white noise sequence, is given by (Teunissen, 1990)

$$\mathbf{v}_k = \mathbf{z}_k - \mathbf{H}_k \hat{\mathbf{x}}_k^{(-)} \quad (2.25)$$

and should also be zero-mean, Gaussian and white with covariance given by

$$\mathbf{C}_{\mathbf{v},k} = \mathbf{H}_k \mathbf{P}_k^{(-)} \mathbf{H}_k^T + \mathbf{R}_k. \quad (2.26)$$

The innovation sequence is a set of predicted measurement residuals generated by subtracting the predicted measurements (calculated using the predicted states  $\hat{\mathbf{x}}_k^{(-)}$ ) from the true measurements. Examination of the Kalman filter equations in Figure 2.1 reveals that both the innovation sequence ( $\mathbf{v}_k$ ) and its associated covariance ( $\mathbf{C}_{\mathbf{v},k}$ ) must be calculated during the update stage of the Kalman filter. As a result, the innovation sequence can be used as a computationally efficient and convenient method for monitoring the performance of the filter. Alternatively, if a linearized measurement model is used the innovation sequence would be given by

$$\mathbf{v}_k = \mathbf{w}_k + \mathbf{H}_k \hat{\mathbf{d}}_k^{(-)} \quad (2.27)$$

with the same associated covariance as in equation (2.26). Teunissen (1990) has suggested a test statistic based on the quadratic form of the innovation sequence given as

$$T_k = \mathbf{v}_k^T \mathbf{C}_{v,k}^{-1} \mathbf{v}_k \quad (2.28)$$

which should have the Chi-squared distribution. A blunder is assumed to have occurred if the test statistic fails the null hypothesis ( $H_o$ ) given by

$$H_o \sim \mathbf{c}^2(m_k, 0) \quad (2.29)$$

where  $m_k$  is the number of degrees of freedom, equal to the number of measurements. The process of identifying a measurement which contains a blunder is complicated by the possibility of multiple blunders at the same epoch. If the innovation sequence test indicates a blunder then all measurements from that sensor for that epoch are rejected. Alternatively, a form of robust statistics could have been employed (Gao, 1992) to try and detect multiple blunders, but this still would not have guaranteed proper identification.

Knowledge of the detection threshold for the innovation sequence test is important because it can be used to calculate the effect of the minimum detectable blunder on the navigation solution. This is an indication of the expected reliability of the system and is covered in Krakiwsky and Abousalem (1995). The following analysis deals with the case of a single assumed blunder in the measurements. The size of the minimum detectable blunder in the measurements is given through specification of two significance levels. The significance level  $\alpha$  is the probability of rejecting a good measurement, known as a type I error, while the significance level  $\beta$  is the probability of mistaking a corrupt measurement for a good one, known as a type II error. These two values together define a non-centrality parameter that represents the mean of the alternate hypothesis ( $H_a$ ) for a standardized innovation value. This situation is shown graphically in Figure 2.4.

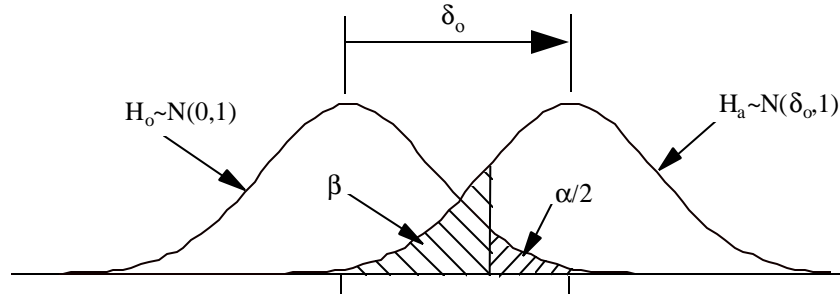


**Figure 2.4 - Determination of mean-centrality parameter  $d_o$  based on specified confidence level (1-a) and significance level (b).**

The minimum detectable blunder (MDB) for a single failure in the  $i^{\text{th}}$  measurement is given by

$$MDB = \nabla l_{k,i} = \frac{d_o}{\sqrt{C_{v,ii}^{-1}}} \quad (2.30)$$

where,  $C_{v,ii}^{-1}$  is the diagonal element in the  $i,i$  location corresponding to the  $i^{\text{th}}$  measurement (Abousalem, 1993). These values represent the internal reliability of the system. The external reliability represents the effect of a blunder on the parameters and is given by

$$\nabla x_{k,i} = -\mathbf{P}_k \mathbf{H}_k^T \mathbf{R}_k^{-1} \mathbf{A}_k \nabla l_{k,i} \quad (2.31)$$

where,  $\mathbf{A}$  is an influence matrix filled with zeros in every location except for a one in the  $i,i$  position. The maximum error (ME) induced due to a single undetected measurement blunder is then determined by cycling through the MDB of every measurement and noting the maximum possible effect in the external reliability calculation.

## **CHAPTER 3**

### **GLOBAL POSITIONING SYSTEM (GPS) OVERVIEW**

The Global Positioning System (GPS) is a satellite based all-weather radionavigation aid developed by the United States Department of Defense (DoD) to provide precise positioning and velocity information to an unlimited number of users anywhere on the planet (Parkinson, 1994). This chapter will give a general overview of GPS, describe the various GPS measurement observables, starting with the single receiver equations, followed by differential measurements and interferometric orientation techniques for the case of two receivers.

#### **3.1 GPS System Architecture**

GPS is comprised of three parts known as the control segment, user segment and space segment (Parkinson, 1994). The control segment is made up of five monitor stations, four ground antenna uplink stations and the Operational Control Center (OCC). The purpose of the control segment is to maintain the GPS. Ground Stations monitor satellite transmissions and orbital behaviour which is then transferred to the OCC. The navigation message to be broadcast by each satellite is formed by the OCC using a Kalman filter algorithm which generates predicted orbits and clock information. This information is then uplinked to the satellites on S-Band for retransmission to the user on L-Band. The space segment consists of 24 satellites orbiting at an approximate height of 20,000 km above the surface of the earth. These are split into six orbital planes each containing four satellites and inclined at  $55^\circ$  to the equator. The satellite constellation has been optimized to provide at least four satellite visibility at any point on the planet at any time.

The user segment consists of all systems which utilize the L-Band transmissions from the GPS satellites. The number of GPS applications has grown exponentially in the last five to ten years with civilian commercial usage and development outstripping military

growth (Parkinson, 1994). The satellites broadcast a coarse acquisition (C/A) code and a precision (P) code ranging message on two frequencies known as L1 (1575.42 MHz) and L2 (1227.60 MHz). The L1 frequency has both C/A and P codes while the L2 frequency has only P code. The P code is encrypted by the DoD and is unavailable to the civilian user while the C/A code, although available to any user, is intentionally degraded. The encryption is known as anti-spoofing (AS) while the intentional degradation is known as selective availability (SA).

For the C/A code, each satellite is assigned an independent 1.023 Mbps pseudo-random noise (PRN) code which is modulated along with a 50 bps navigation message on the L1 carrier. The navigation message contains satellite location and timing information as well as system status messages.

### 3.2 GPS Observables

Current GPS receivers are capable of tracking up to twelve satellites at once. Most GPS receivers are capable of tracking the standard L1 pseudorange positioning measurement, the carrier phase signal and the Doppler. The range measurement to the satellite is referred to as a pseudorange because it is corrupted by a common receiver clock bias. The pseudorange ( $p$ ) from the receiver (subscript  $r$ ) to the  $i^{\text{th}}$  satellite is given as (Wells et al., 1987)

$$p_r^i = \mathbf{r}_r^i + d\mathbf{r}^i + c(dt^i - dT_r) + d_{r,ion}^i + d_{r,trop}^i + \mathbf{e}_r^i(p) \quad (3.1)$$

where,  $p$  is the pseudorange [m],

$\rho$  is the true range to the satellite [m],

$d\rho$  is the satellite orbital error [m],

$c$  is the speed of light [m/s],

$dt$  is the satellite clock error given in the navigation message [s],  
 $dT$  is the receiver clock error [s],  
 $d_{ion}$  and  $d_{trop}$  are the errors due to ionospheric and tropospheric propagation [m]  
 and  $\epsilon$  represents remaining error sources such as multipath and receiver noise [m].

The error sources in equation (3.1) are described in more detail at the end of the chapter. To define a position for a given receiver, the three-dimensional position vector and common receiver clock bias must be estimated, requiring pseudoranges to a minimum four satellites at a given instant. The true range to the  $i^{\text{th}}$  satellite from the receiver ( $r$ ) is given by

$$\mathbf{r}_r^i = \sqrt{(x^i - x_r)^2 + (y^i - y_r)^2 + (z^i - z_r)^2} \quad (3.2)$$

where  $(x^i, y^i, z^i)$  is the position of the satellite given by the navigation message and  $(x_r, y_r, z_r)$  is the unknown position of the receiver in the Earth-centered, Earth-fixed (ECEF) Cartesian frame defined by WGS-84 (Malys et al., 1997). The carrier phase observable ( $\phi$ ), in metres, at the receiver ( $r$ ) for the  $i^{\text{th}}$  satellite is given by

$$\mathbf{f}_r^i - \mathbf{1}N_r^i = \mathbf{r}_r^i + d\mathbf{r}_r^i + c(dt^i - dT_r) - d_{r,ion}^i + d_{r,trop}^i + \mathbf{e}_r^i(\mathbf{f}) \quad (3.3)$$

where  $\lambda$  is the L1 wavelength (19.02 cm),  $N$  is the unknown integer number of cycles between the receiver and the satellite and  $\epsilon(\phi)$  is the effect of carrier phase receiver noise, carrier phase multipath and antenna phase centre instability. The remaining errors are similar to equation (3.1) except for the reversal of sign on the ionospheric error explained in section 3.5.2. Although much more precise than the pseudorange measurement, the carrier phase measurement suffers from the unknown carrier phase ambiguity which must

be determined for every satellite. Ambiguity resolution will be dealt with in Chapter 4. Finally, the Doppler measurement ( $\dot{\mathbf{f}}$ ) is given by

$$\dot{\mathbf{f}}_r^i = \dot{\mathbf{r}}_r^i + d\dot{\mathbf{r}}_r^i + c(\dot{dt}^i - d\dot{T}_r) - \dot{d}_{r,ion}^i + \dot{d}_{r,trop}^i + \mathbf{e}_r^i(\dot{\mathbf{f}}) \quad (3.4)$$

where the dots represent the time derivatives. The Doppler measurement can be used for velocity estimation as well as for cycle slip detection, when a known carrier phase ambiguity is lost due to line of sight interference or high dynamics (Lachapelle, 1995). An estimate ( $\hat{\mathbf{f}}_k$ ) of the new carrier phase at time  $k$  is generated based on the Doppler ( $\dot{\mathbf{f}}_k$ ) and the time interval ( $\Delta t$ ) as shown in equation (3.5).

$$\hat{\mathbf{f}}_k = \mathbf{f}_{k-1} + \frac{\dot{\mathbf{f}}_k + \dot{\mathbf{f}}_{k-1}}{2} \Delta t \quad (3.5)$$

The result is subtracted from the true carrier phase measurement and compared to a threshold based on the expected vehicle dynamics. If the threshold is exceeded, a cycle slip has occurred and the carrier phase ambiguity may have to be redetermined. This is known as the phase rate prediction method (ibid.).

### 3.3 Differenced GPS Observables

Certain errors such as those caused by atmospheric effects and improperly modeled orbits can be highly spatially correlated over distances up to about 25 km (Lachapelle, 1995). Other errors such as mismodeled satellite clock are common to all range measurements to that satellite. To eliminate or greatly reduce these error sources, GPS observables can be differenced across receivers and/or satellites. This process is known as differential GPS (DGPS) and is shown in Figure 3.1. The between receiver single difference pseudorange equation for the  $i^{\text{th}}$  satellite is given by

$$\Delta p_{rm}^i = \Delta \mathbf{r}_{rm}^i + c\Delta dT_{rm} + \Delta \mathbf{e}_{rm}^i(p) \quad (3.6)$$

where,  $\Delta_{ij}$  is the single difference operator defined as  $\Delta a_{ij} = a_i - a_j$ . The  $r$  subscript denotes the remote receiver while the  $m$  subscript denotes the monitor receiver where the monitor location is assumed known and the relative vector between the monitor and receiver is the desired information. The satellite clock error has been canceled while the satellite orbit term and atmospheric terms are assumed eliminated based on their spatial correlation. Note that for longer distances between receivers, the correlation is less and some residual error could remain after differencing. The  $\varepsilon$  term for each receiver is in general uncorrelated and the difference operation thus increases the measurement noise by a factor of  $\sqrt{2}$ .

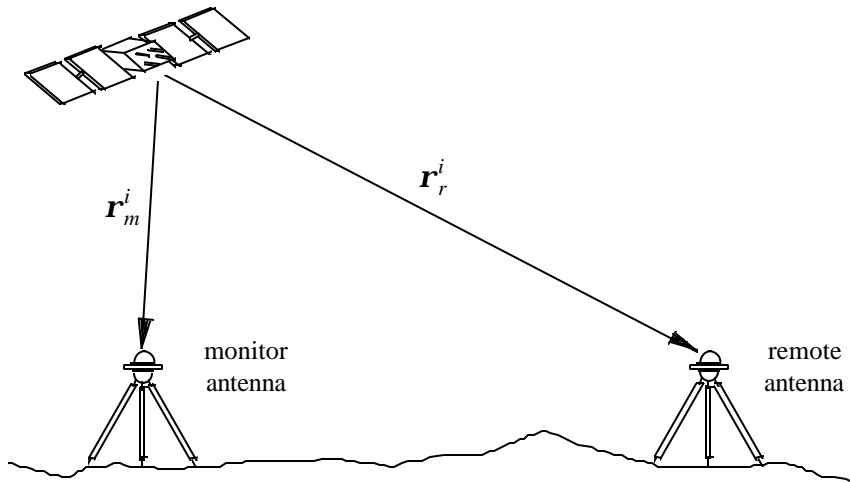


**Figure 3.1 - Single difference between receiver measurement.**

The carrier phase single difference equation is given by

$$\Delta \mathbf{f}_{rm}^i - \mathbf{I} \Delta N_{rm}^i = \Delta \mathbf{r}_{rm}^i + c\Delta dT_{rm} + \Delta \mathbf{e}_{rm}^i(\mathbf{f}) \quad (3.7)$$

where the satellite clock error has canceled and the orbital error and atmospheric terms have once again been assumed eliminated. In order to use this equation the single difference ambiguity term must be estimated as an unknown or determined independently. In a similar manner, the single difference Doppler or phase-rate equation is given by

$$\Delta \dot{\mathbf{f}}_{rm}^i = \Delta \dot{\mathbf{r}}_{rm}^i + c\Delta dT_{rm} + \Delta \mathbf{e}_{rm}^i(\dot{\mathbf{f}}). \quad (3.8)$$

To eliminate the relative receiver clock term in the above three single difference equations, the results are differenced across satellites as demonstrated in Figure 3.2.

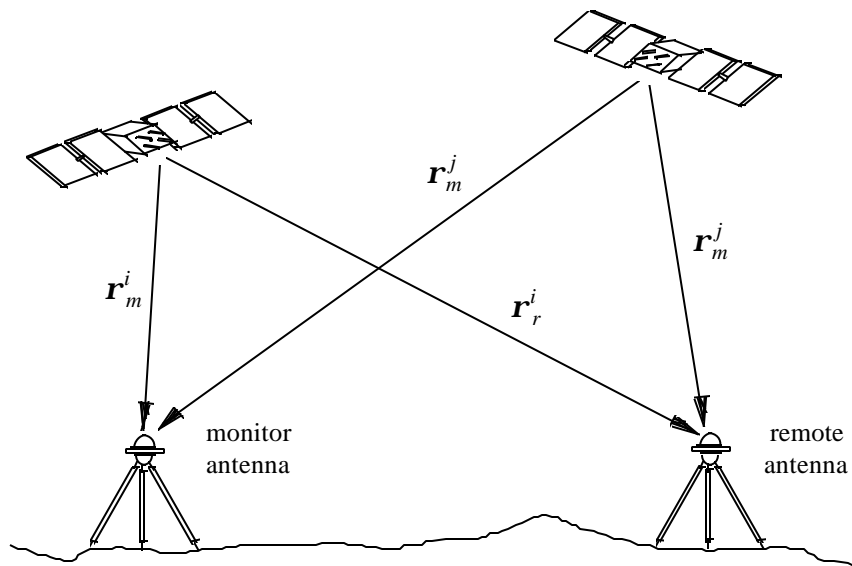


**Figure 3.2 - Double difference between satellite, between receiver measurement.**

In a double difference situation the number of measurements is equal to  $(n-1)$  where  $n$  is the number of tracked satellites. The satellite chosen for differencing is generally the one with the highest elevation as this type of measurement tends to be less noisy due to a

shorter path through the atmosphere and decreased chance of a reflected signal. This is known as the base satellite. The double difference measurement for the pseudorange is given by

$$\nabla\Delta p_{rm}^{ij} = \nabla\Delta\mathbf{r}_{rm}^{ij} + \nabla\Delta\mathbf{e}_{rm}^{ij}(p). \quad (3.9)$$

The  $\nabla\Delta$  is the double difference operator, which for a given quantity  $a$  is defined as  $\nabla\Delta a_{rm}^{ij} = (a_r^i - a_m^i) - (a_r^j - a_m^j)$  where the superscript denotes satellite and the subscript denotes receiver. The  $\varepsilon$  term has increased by  $\sqrt{2}$  once more to account for the noise in the difference such that the total multiplier is two. The carrier phase equation for the double difference case is

$$\nabla\Delta\mathbf{f}_{rm}^{ij} - I\nabla\Delta N_{rm}^{ij} = \nabla\Delta\mathbf{r}_{rm}^{ij} + \nabla\Delta\mathbf{e}_{rm}^{ij}(\mathbf{f}), \quad (3.10)$$

while the double difference equation for the Doppler measurement is

$$\nabla\Delta\dot{\mathbf{f}}_{rm}^{ij} = \nabla\Delta\dot{\mathbf{r}}_{rm}^{ij} + \nabla\Delta\dot{\mathbf{e}}_{rm}^{ij}(\dot{\mathbf{f}}). \quad (3.11)$$

In general, pseudorange measurements are best used with a single difference model while carrier phase based measurements are more effective with a double difference model. For the pseudorange case, the advantage of removing the receiver clock term through double differencing is eclipsed by the growth in the measurement noise of the system. In the carrier phase case, the presence of the relative receiver clock term after only a single difference makes it difficult to establish the integer ambiguities. Some systems with short (~1-10 m) baselines have attempted to use a common oscillator to overcome this problem but this still fails to remove differential propagation delays in the hardware of the two receivers due to different cable lengths and differential heating of amplifiers (Van

Graas and Dutton, 1997). Calibration of this differential hardware bias is complicated by its long-term instability. In double differenced carrier phase measurements the differential hardware delays are removed along with the clock bias.

### 3.4 Interferometric Techniques for Orientation

When two or more GPS antennas are rigidly mounted to a platform, they can be used to determine the orientation of the platform with respect to a given reference frame (Knight and Hatch, 1990), (Cohen, 1992). The achievable accuracy of a GPS orientation system is a function of the baseline length (El-Mowafy, 1994) between the GPS antennas which is, in general, only limited by the size of the platform. In practice, larger structures can be subject to differential flexing which can negate the rigid-body assumption (Cannon and Sun, 1994). If three or more non-collinear antennas are mounted on the vehicle then three-dimensional attitude determination is possible. If two or any number of collinear antennas are mounted on the platform then only two attitude parameters can be estimated, generally an azimuth and a pitch angle. The short baselines in orientation applications are best resolved using the most precise measurement available, namely the GPS carrier phase (Schleppe, 1996). If the baselines are sufficiently short, then the unit vector from each antenna to a given satellite can be assumed identical (Van Graas and Braasch, 1991). This is known as GPS interferometry and is shown in Figure 3.3.

The single difference measurement can then be approximated as the dot product of the baseline vector with the satellite unit vector as given by

$$\Delta f_{rm}^i - I \Delta N_{rm}^i \approx -\mathbf{e}^i \cdot \mathbf{r} + c \Delta T_{rm} \quad (3.12)$$

where,  $\mathbf{r}$  is the antenna baseline vector in the Earth-Centered, Earth Fixed (ECEF) WGS-84 Cartesian coordinate frame, and  $\mathbf{e}^i$  is the unit vector to the  $i^{\text{th}}$  satellite again in the

WGS-84 frame. The single difference ambiguity term ( $\Delta N$ ) and the relative receiver clock error ( $c\Delta dT$ ) are the same as for equation (3.7). Schleppe (1996) has shown that the interferometric assumption for baselines up to 100 metres induces only a 0.02 mm error in the single difference carrier phase measurement.

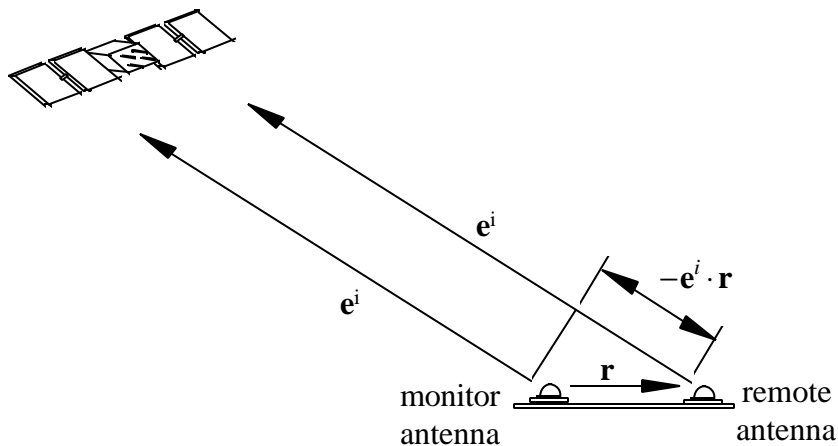


**Figure 3.3 - Single difference interferometric observation,  $\mathbf{e}^i$  assumed identical for each receiver.**

The relative receiver clock error in equation (3.12) can be eliminated by subtracting the single difference for the  $j^{\text{th}}$  satellite from the  $i^{\text{th}}$  satellite to form a double difference interferometric observation

$$\nabla\Delta\mathbf{f}_{rm}^{ij} - I\nabla\Delta N_{rm}^{ij} \approx -(\mathbf{e}^i - \mathbf{e}^j) \cdot \mathbf{r} \quad (3.13)$$

where,  $\nabla\Delta$  is the double difference operator and the double difference ambiguity ( $\nabla\Delta N$ ) is the same as found in equation (3.10). Conceptually, the orientation of a platform is most easily visualized when it is referenced to a horizon-based or local level (LL) coordinate frame centered at the user's approximate position. Considering a dual antenna

GPS system, the baseline vector (  $\mathbf{r}$  ) in the ECEF frame can be transformed to the local level system by (Lu, 1995)

$$\mathbf{r} = \mathbf{T} \cdot \mathbf{b} \quad (3.14)$$

where,  $\mathbf{T}$  is the rotation matrix from the LL to the ECEF frame and  $\mathbf{b}$  is the baseline vector in the local level frame. The rotation matrix  $\mathbf{T}$  is given by

$$\mathbf{T} = \begin{bmatrix} -\sin\Phi_L \cos\Lambda & -\sin\Lambda & \cos\Phi_L \cos\Lambda \\ -\sin\Phi_L \sin\Lambda & \cos\Lambda & \cos\Phi_L \sin\Lambda \\ \cos\Phi_L & 0 & \sin\Phi_L \end{bmatrix} \quad (3.15)$$

where,  $\Phi_L$  is the latitude of the user location and  $\Lambda$  is the longitude of the user location. The local level baseline vector can be written as

$$\mathbf{b} = \begin{bmatrix} \Delta N \\ \Delta E \\ \Delta U \end{bmatrix} = \begin{bmatrix} b \cdot \cos\psi \cdot \cos\theta \\ b \cdot \sin\psi \cdot \cos\theta \\ b \cdot \sin\theta \end{bmatrix} \quad (3.16)$$

where two possible representations have been shown. The first is a local level Cartesian coordinate frame and the second is a curvilinear representation where  $b$  is the baseline length,  $\psi$  is the azimuth angle, measured clockwise from North in the horizon plane and  $\theta$  is the pitch angle, defined as the inclination angle of the baseline vector with respect to the horizontal plane. This is shown graphically in Figure 3.4.

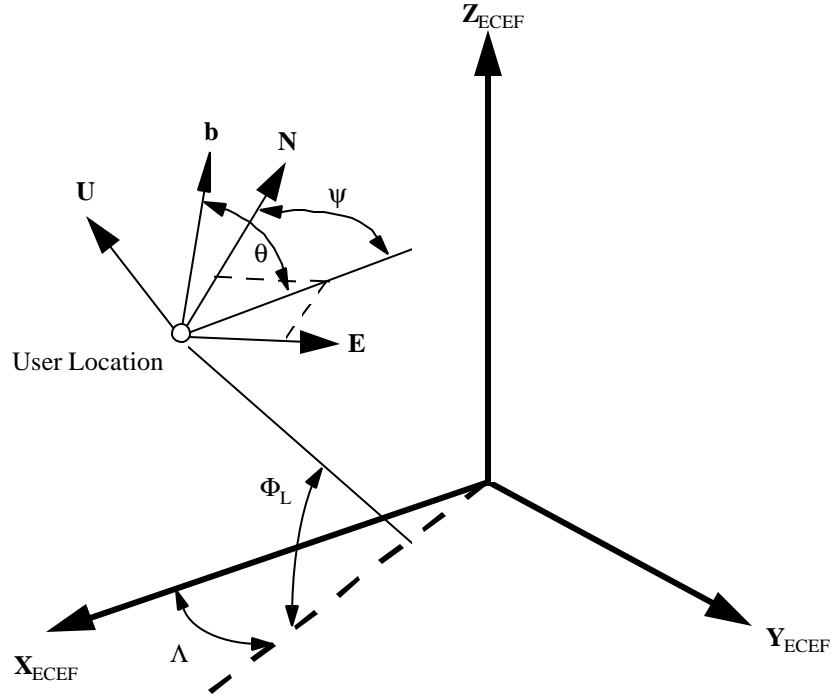


**Figure 3.4 - Azimuth ( $\psi$ ) and pitch ( $\theta$ ) of baseline vector  $\mathbf{b}$  in local level (E,N,U) frame. The Earth-centered, Earth-fixed (ECEF) frame is also shown.**

Substitution of equation (3.14) into (3.13) yields

$$\nabla \Delta \mathbf{f}_{rm}^{ij} - I \nabla \Delta N_{rm}^{ij} \approx -(\mathbf{e}^i - \mathbf{e}^j) \cdot \mathbf{T} \cdot \mathbf{b} \quad (3.17)$$

where the carrier phase measurement ( $\nabla \Delta \phi$ ) and associated double difference ambiguity ( $\nabla \Delta N$ ) have been directly related to the orientation parameters ( $\psi$ ,  $\theta$ ) and baseline length ( $b$ ) of the dual-antenna GPS system in the local level frame. This research is focused on the use of a dual-antenna single baseline GPS system for the estimation of azimuth ( $\psi$ ) and pitch ( $\theta$ ) as represented in Figure 3.4.

### 3.5 GPS Error Sources

In order to fully realize the potential of GPS, the error sources in equations (3.1), (3.3) and (3.4) must be reduced through modeling or additional measurements. Certain errors are also spatially correlated or common to a specific receiver or satellite and can be reduced by differencing measurements as shown in section 3.3. The magnitude of the various error sources is shown in Table 3.1 for the spatially correlated and satellite dependent errors (Lachapelle, 1995).

**Table 3.1 - Spatially correlated and satellite dependent error sources.**

Error Source	Standard Positioning Service (SPS) 1- $\sigma$ range error
Selective Availability (SA)	24.0 m
Atmospheric Error	
Ionospheric	7.0 m
Tropospheric	0.7 m
Satellite Clock and Orbit Error	3.6 m
Accumulated Range Error (1- $\sigma$ )	25.3 m

The remaining error sources, multipath, receiver noise and antenna phase centre variation are dependent to a large degree on the quality of the user equipment and localized environment. The antenna phase center is the point to which all GPS measurements are referenced. Ideally, this phase center is invariant but in practice can be a function of satellite elevation and azimuth. For micro-strip patch antennas, such as those used in this research, the resulting range error can be 1-2 mm (Lachapelle, 1995). Fortunately, the antenna phase variations are a function of the manufacturing process and are relatively similar between antennas of the same make. The effect of antenna phase center variation

can be virtually eliminated by using the same make of antenna for both receivers and orientating them in the same direction. The remaining errors, multipath and receiver noise, are shown in Table 3.2 (Lachapelle, 1995) and are much larger for the pseudorange as opposed to the carrier phase.

**Table 3.2 - Receiver and local environment dependent errors.**

Error Source	Pseudorange (p)	Carrier Phase ( $\phi$ )
Receiver Noise	10 → 300 cm	0.5 mm → a few mm
Multipath	≤ 1 chip (300 m)	≤ 0.25 $\lambda$ ( 5 cm)

While the pseudorange is an absolute measurement, the carrier phase suffers from the unknown carrier phase ambiguity as described in section 3.1. In order to take full advantage of the carrier phase measurement precision, these ambiguities must be resolved. For orientation applications, the short baseline lengths ensure that virtually all of the error from Table 3.1 is eliminated. The dominant error sources are then carrier phase receiver measurement noise and carrier phase multipath (Cohen, 1992).

### 3.5.1 Selective Availability

The dominant error source in GPS positioning when using a single receiver is selective availability (SA). When the first operational results of GPS were available it became apparent that the civilian frequency was capable of providing a level of accuracy which exceeded the design criteria. Selective availability, the intentional degradation of the system through satellite orbit and clock manipulation in the navigation message, is to prevent potential hostile users from using GPS effectively against the United States. The

current implementation of SA, primarily found in the mismodeling of the satellite clock, has a level of accuracy guaranteed horizontally to 100 m 2DRMS (95% of the time) and vertically to 140 m (95%) (Van Graas and Braasch, 1994). The specifications were chosen to be comparable to the accuracy currently achievable with existing VHF omnidirectional range (VOR) stations (ibid.) and can only be changed through order of the President of the United States.

In real-time, since SA is common to a particular satellite, its effect can be eliminated by differencing across receivers as long as the data transmission latency between stations is kept as low as possible. The rate of change of the SA induced clock error can cause ranging error rates on the order of 30 cm/s (Lachapelle, 1995). For carrier phase positioning requiring ambiguity resolution the data latency should be less than two seconds (Lan, 1996). For post-mission processing of differential data, SA can be eliminated through the use of precise satellite orbits and satellite clock data calculated by various civilian agencies (Duval et al., 1996). The U.S. government has decided to discontinue the use of SA over the next decade (Presidential Decision Directive from the White House, 1996) leaving the ionosphere as the largest single error source.

### **3.5.2 Ionospheric Propagation Errors**

When SA is not operational, the largest source of error in the GPS budget is the ionosphere as shown in Table 3.1. The ionosphere is a dispersive medium consisting of that region of the atmosphere extending from an altitude of about 250 km to about 500 km. It is made up of a weakly ionized gas, formed when solar radiation strikes the planet and ionizes particles in the atmosphere. The resulting free electron density is therefore a function of solar activity and location, with the equatorial and polar regions being most active while the temperate regions are more stable. The effect of the ionosphere on a GPS signal is proportional to the total electron content (TEC) measured as the number of electrons per square metre along the line of sight vector between receiver and satellite

(Klobuchar, 1996). GPS signals which transit the ionosphere are subjected to refraction, Faraday rotation, scintillation effects, a velocity advance in the carrier phase and a velocity delay in the modulated signal (ibid.). The delay in the modulated signal is a timing error which results in an incorrect receive time at the receiver and a corresponding range error. The amount of delay is dependent on the refractive index which, to first order, is proportional to the TEC and inversely proportional to the frequency squared. The effects of Faraday rotation and refraction were minimized in the GPS design phase by choosing a high (1.6 GHz) frequency and a right-hand circularly polarized transmission pattern (ibid.). Scintillation effects are caused by localized ionospheric anomalies that can cause local TEC values to change drastically in a short period of time and severely stress a receiver's ability to track a satellite signal ( Wanninger, 1993).

The problem with the ionosphere is the high day-to-day variability of the TEC which is currently impossible to estimate without some form of real-time data (Klobuchar, 1996). DGPS positioning can rely on the spatially correlated property of ionospheric errors to remove much of the effect. For single receiver positioning, the error must be either modeled, measured or provided by an outside source. Embedded in the GPS navigation message are a series of coefficients based on a simple ionospheric model. When applied to a GPS range measurement, this model is expected to eliminate at least 50% of the ionospheric range error (Klobuchar, 1996). Certain high-end receivers are capable of making a limited measurement on L2 even with anti-spoofing engaged (Lachapelle, 1995). The dispersive nature of the ionosphere means that the differential delay between the two GPS frequencies (L1 and L2) can be used to estimate the ionospheric error as well. Finally, the ionospheric corrections could be computed by an outside organization and then made available to the single-frequency user through some data-link such as a cellular phone or FM sub-carrier.

### **3.5.3 Tropospheric Propagation Errors**

GPS signal propagation errors in the atmosphere which are not frequency dependent, and therefore non-dispersive, are grouped under the heading of tropospheric errors and generally occur in the region of the atmosphere from 0-60 km (Lachapelle, 1995). Tropospheric effects are not as severe as ionospheric effects and are caused by a combination of the wet and dry parts of the troposphere. The dry part, which accounts for about 90% of the total error (Spilker, 1994), consists of various gases such as nitrogen, oxygen and carbon dioxide. The effect of the dry part at GPS frequencies (1.6 GHz) is due to oxygen content and concentration which is fortunately highly predictable (ibid.). The wet part of the troposphere accounts for about 10% of the total error and is caused by water vapour which is generally found in the region 0-12 km above sea level. The water vapour composition of the troposphere is highly variable and hence difficult to predict. Tropospheric errors are greatest for satellites of extremely low elevation ( $\leq 10^\circ$ ) due to the longer path length in the troposphere (Qiu, 1993). By not using satellites that are below a  $10^\circ$  cut-off, much of the tropospheric error can be avoided.

Tropospheric errors can be reduced or eliminated through differential GPS or by applying tropospheric models. The various tropospheric models available are excellent at predicting the dry part contribution to the error (within 1%) but are much less effective for the wet part, leaving a 3-4 cm error (Wells et al., 1987). For short baselines used in orientation applications, the differential technique along with a sufficient mask angle can remove all tropospheric effects.

### **3.5.4 Multipath and Receiver Measurement Noise Errors**

Multipath and receiver measurement noise errors are unique from the point of view that, in general, they cannot be removed through modeling or differencing. Receiver

measurement noise is highly dependent on the quality of the user equipment and is not correlated spatially, across receivers or across satellites and cannot be removed through differencing or modeling (Lachapelle, 1995). The orientation application in this research is dependent on the carrier phase observable as described in section 3.4. Receiver carrier phase noise is a function of the GPS signal strength and the dynamics of the vehicle (Qiu, 1993). GPS signal strength for a given satellite depends on the elevation of the satellite, the gain of the antenna and any line-of-sight interference such as foliage. For high dynamics the bandwidth of the tracking loops must be increased to maintain lock on the satellite signal which increases the amount of wideband noise and hence the measurement noise.

A common way of determining the carrier phase noise of a receiver is through a zero-baseline test, where two GPS receivers are connected to the same antenna. The resulting error, when the results are double differenced, is due only to the receiver carrier phase noise since all other error sources are common to the antenna and removed. The actual value is equal to twice the carrier phase noise due to the multiplication of the error by  $\sqrt{2}$  after each difference. A zero-baseline test for the NovAtel MiLLennium™ receiver used in this research was completed by Newby et al. (1996) with L1 frequency carrier phase accuracies better than 1 mm.

Multipath, the reception of an unwanted reflected GPS signal in addition to, or in place of, the line of sight GPS signal is the largest source of error for orientation or attitude applications (Cohen, 1992). Multipath is primarily a function of the localized antenna environment and can be reduced through proper site location (Braasch, 1995). Establishing a DGPS reference site or undertaking a precise static survey are examples of

situations where site selection demands a high priority. Time invested in proper site selection can drastically reduce the possibility of multipath before it occurs.

In kinematic situations it is often only possible to optimize the antenna location with respect to the mounting platform. The environment through which the platform will pass is often unknown and could have poor multipath characteristics. Unlike static multipath which in general has a period of a few minutes (Geier, 1995), kinematic multipath could be highly variable and is often difficult to distinguish from actual platform motion. Most of the methods for reducing multipath are based on the fact that multipath is most common on low elevation satellites (Braasch, 1995). GPS antennas tend to have low gain for small elevation angles and can be situated on ground planes or chokerings to cut down or eliminate low elevation signals (Lachapelle, 1995). Some advanced receivers attempt to reduce pseudorange multipath through estimation of its effect. NovAtel's multipath elimination technology (MET) and multipath estimating delay lock loop (MEDLL) are examples of this type of technology (Townsend et al., 1995).

For an orientation application using a GPS inter-antenna distance of 1m, and assuming a 2 cm positional error on one antenna due to carrier phase multipath, the resulting angular error is on the order of 1.2 arcmin.

## **CHAPTER 4**

### **GPS CARRIER PHASE AMBIGUITY RESOLUTION**

GPS receivers are only capable of measuring the fractional part of the GPS carrier phase observable. The result is that between the receiver and the satellite there are an unknown number of initial integer cycles that must be determined before a precise carrier-phase based range measurement can be formed (Lachapelle, 1995). This cycle ambiguity remains constant as long as no carrier phase tracking errors occur.

In a growing number of applications, it is necessary to be able to resolve the integer ambiguities while the GPS receiver is in motion. This is not, in general, a trivial process and is known as on-the-fly (OTF) ambiguity resolution. Significant effort has been devoted to the problem of OTF ambiguity resolution resulting in a variety of possible algorithms. These include the least squares ambiguity search technique (Hatch, 1990), the ambiguity function method (AFM) originally proposed by Counselman and Gourevitch (1981) and used by Remondi (1984) and Mader (1990), the fast ambiguity resolution approach (FARA) (Frei et al., 1990) and the fast ambiguity search filter (FASF) (Chen and Lachapelle, 1994). Regardless of the method chosen there are essentially three steps in determining the correct integer ambiguity set. The first is to choose an ambiguity search space, the second to generate a list of all possible ambiguity combinations within that space and the last is to isolate the correct ambiguity set.

The determination of the search space is probably the single most important step because the process involves weighing two conflicting criteria. The search space should be defined so that, given a normal error distribution, the correct ambiguity set will always be contained within the search volume. On the one hand, a small search volume will generate only a small number of potential ambiguity sets which will reduce the computation time required for statistical testing. On the other hand, a larger search volume has a higher probability of containing the correct ambiguity set. The search

volume defines a finite number of possible integer ambiguity combinations, the most likely potential ambiguity set is then identified through a series of tests.

#### **4.1 GPS Ambiguity Resolution for Attitude Applications**

The carrier phase ambiguity resolution problem for attitude applications has been examined by many, including Hatch (1990), Cohen (1992), El-Mowafy (1994), Lu (1995), Euler and Hill (1995) and Schleppe (1996). Differencing GPS carrier phase measurements over the short baselines found in attitude applications essentially cancels the spatially correlated errors such as ionosphere, troposphere and mismodeled orbits. Another advantage for GPS attitude systems is that the baselines between antennas are rigidly fixed in most cases. These distances can be measured *a priori* and used as a constraint in carrier phase ambiguity resolution.

The carrier phase ambiguity resolution procedure used in this research is based on a least squares method developed by Hatch (1990). Figure 4.1 is a block diagram of the ambiguity resolution algorithm. At least one degree of freedom is necessary for statistical testing, corresponding to a minimum of five satellites, giving four double difference carrier phase measurements for three position unknowns. The steps involved are listed below and described in detail later.

1. Determine ambiguity search space, equivalent to an approximate position of the remote antenna with respect to the monitor antenna with a given uncertainty. The three-dimensional attitude vector in this case is defined as the direction from the monitor to the remote antenna.
2. Chose four primary satellites, generally the highest elevation satellites that still exhibit reasonable geometry. The highest satellite is designated the base satellite for differencing. The three resulting double differences form a unique relative position solution.

3. Compute all potential ambiguity sets of the primary satellites defined in the search volume. The position solution of the primary ambiguity set is used to set the ambiguities of the non-primary satellites (designated secondary satellites). A new relative position vector is then generated using least squares estimation. The resulting baseline length is compared to the *a priori* length in a baseline test. The estimated variance factor is also calculated.
4. If more than one ambiguity set still exists, they are stored until more GPS measurements are available. The baseline test is then performed again. If all but one of the potential ambiguity sets cannot be eliminated then the sum of the squared residuals for each remaining set must be used in a ratio test to select the best set.

The first three steps of the resolution procedure require the most computation time. With current computer technology it is possible to perform all calculations in much less than one second. The procedure is thus suitable for real-time implementation in situations where GPS data is collected at a 1 Hz rate. The University of Calgary has developed a real-time GPS-only system, known as HEAD<sup>TM</sup> (Sun and Cannon, 1995), that uses a modified least squares method based on Hatch (1990). This approach was also used by Schleppe (1996) in a slightly different form.

#### **4.1.1 Ambiguity Search Space and Primary Satellites**

The choice of primary satellites is a trade-off between obtaining measurements with very low noise and having a good satellite distribution. Generally, the highest elevation satellites have the least noise, but four high elevation satellites would provide poor geometry for a position solution. The primary satellites are initially chosen as the four highest visible satellites and then tested to determine their geometric merit. Satellite geometry is measured in terms of relative dilution of precision (RDOP), in this case relative position DOP or RPDOP. All RDOP measures are based on the normal matrix (**N**) given by

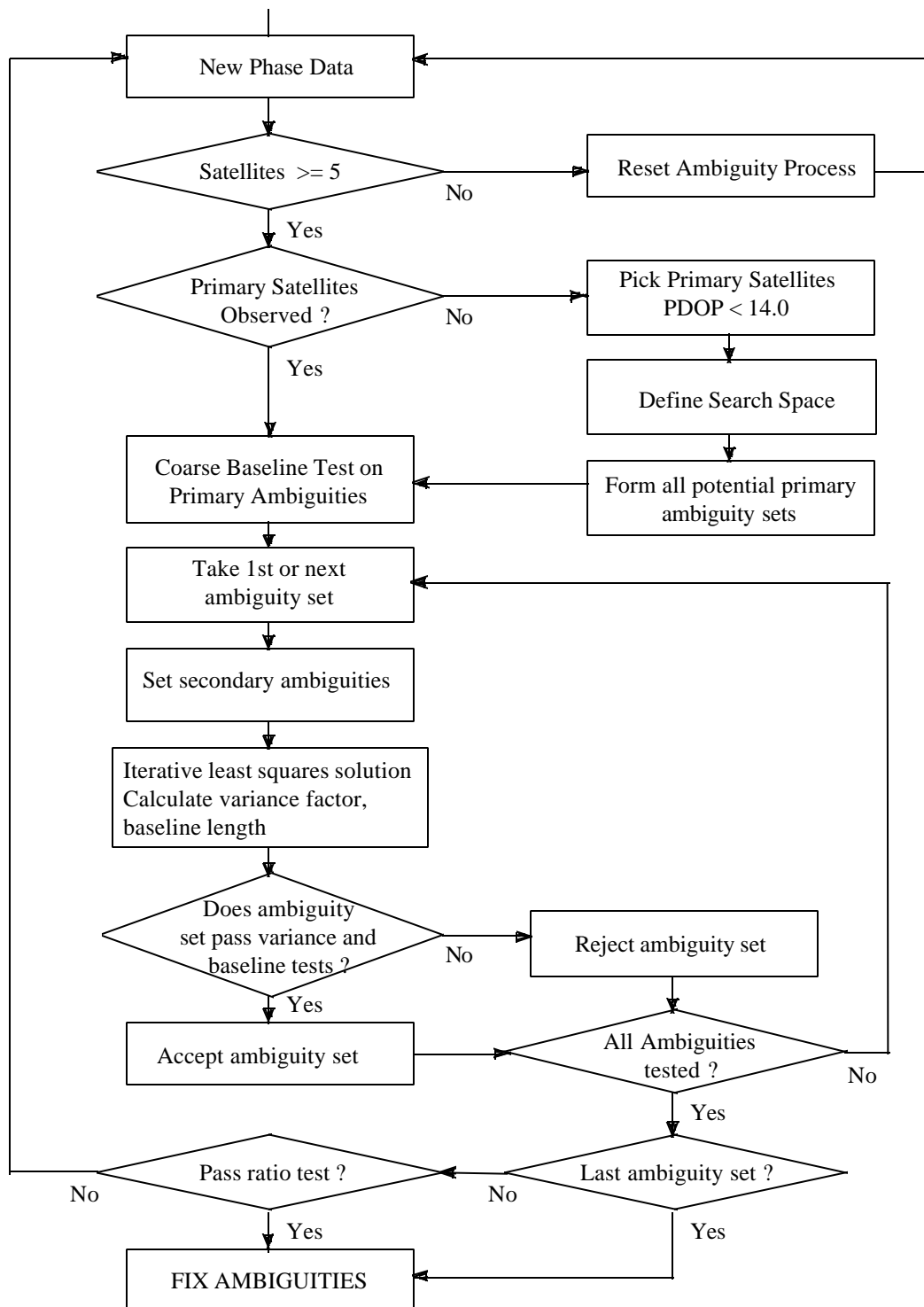


**Figure 4.1 - Ambiguity resolution flow chart.**

$$\mathbf{N} = \mathbf{H}^T \mathbf{H} \quad (4.1)$$

where  $\mathbf{H}$  is the double difference carrier phase design matrix for the four primary satellites and the superscript  $T$  denotes transpose. The  $\mathbf{H}$  matrix is calculated using equation (2.18) because the carrier phase measurement in equation (3.3) must be linearized. The result is shown in equation (4.2) where the superscript denotes satellite and the subscript denotes receiver.

$$\mathbf{H} = \begin{bmatrix} \frac{(x^b - x_r)}{\mathbf{r}_r^b} - \frac{(x^1 - x_r)}{\mathbf{r}_r^1} & \frac{(y^b - y_r)}{\mathbf{r}_r^b} - \frac{(y^1 - y_r)}{\mathbf{r}_r^1} & \frac{(z^b - z_r)}{\mathbf{r}_r^b} - \frac{(z^1 - z_r)}{\mathbf{r}_r^1} \\ \frac{(x^b - x_r)}{\mathbf{r}_r^b} - \frac{(x^2 - x_r)}{\mathbf{r}_r^2} & \frac{(y^b - y_r)}{\mathbf{r}_r^b} - \frac{(y^2 - y_r)}{\mathbf{r}_r^2} & \frac{(z^b - z_r)}{\mathbf{r}_r^b} - \frac{(z^2 - z_r)}{\mathbf{r}_r^2} \\ \frac{(x^b - x_r)}{\mathbf{r}_r^b} - \frac{(x^3 - x_r)}{\mathbf{r}_r^3} & \frac{(y^b - y_r)}{\mathbf{r}_r^b} - \frac{(y^3 - y_r)}{\mathbf{r}_r^3} & \frac{(z^b - z_r)}{\mathbf{r}_r^b} - \frac{(z^3 - z_r)}{\mathbf{r}_r^3} \end{bmatrix} \quad (4.2)$$

The superscript  $b$  denotes the base satellite used for differencing, subscript  $r$  is the remote receiver and  $\mathbf{r}_r^i$  is the range from the  $j^{\text{th}}$  receiver to the  $i^{\text{th}}$  satellite. The vector  $(x^i, y^i, z^i)$  is the ECEF position of the  $i^{\text{th}}$  satellite provided in the navigation message and  $(x_j, y_j, z_j)$  is the approximate ECEF position of the desired receiver location.

The RPDOP is calculated by inverting the normal matrix ( $\mathbf{N}$ ) and then taking the square root of the sum of the diagonal elements. The RPDOP multiplied by the user-equivalent range error (UERE) gives a measure of the relative positioning accuracy (Parkinson, 1994). Given the correct set of ambiguities for the primary satellites, the resulting relative vector should have a length that is within the RPDOP estimated accuracy of the *a priori* baseline length. This forms the basis for the coarse baseline test used in section 4.1.2. For the GPS carrier phase the UERE is on the order of 2 cm based on the

assumption that the correlated errors in Table 3.1 are eliminated or greatly reduced and the errors in Table 3.2 dominate. In choosing the primary satellites, a maximum RPDOP of 14.0 is imposed resulting in a maximum baseline error of roughly 30 cm. If the RPDOP of the chosen satellites is greater than this threshold, the lowest primary satellite is replaced by the next lowest and the RPDOP calculated again.

Once the primary satellites have been chosen, the ambiguity search space must be defined. The primary advantage of an attitude system is that the baseline length can be assumed fixed and measured *a priori*. When there is no *a priori* information regarding the orientation of the system then the remote antenna could be in any direction from the monitor station at a distance of the known baseline length. The search volume is then a sphere, centered at the monitor antenna, with a radius roughly equal to the *a priori* baseline length. The search volume is then used to define the range for each of the three primary satellite double difference ambiguities.

#### **4.1.2 Determination of Primary Ambiguity Sets**

The search volume defines a minimum and maximum value for each of the three primary double difference ambiguities. Given that the range (  $r$  ), in L1 cycles (19.02 cm), defined by the maximum and minimum values for each primary ambiguity is  $r_1$ ,  $r_2$  and  $r_3$  respectively, the total number of potential primary ambiguity sets is equal to  $r_1 \times r_2 \times r_3$ . For a spherical search volume of radius one metre, the number of potential ambiguity sets would be about 600. The centre of the spherical search volume is calculated using the monitor antenna GPS pseudoranges in a single point solution, described in Chapter 6.

In a least squares sense, the objective is to estimate a correction vector ( $\hat{\mathbf{d}}$ ) to the approximate position  $\mathbf{x} = (x_j, y_j, z_j)$  of the remote antenna. For the first iteration, with the short distances involved, the position of the monitor and remote antenna can be

considered coincident. The result is that the estimated correction vector represents the true relative vector. Further information regarding the least squares estimation procedure can be found in Krakiwsky (1990). The estimated correction vector ( $\hat{\mathbf{d}}$ ) representing the difference between the monitor and remote positions is given by

$$\hat{\mathbf{d}} = -(\mathbf{H}^T \mathbf{R}^{-1} \mathbf{H})^{-1} \mathbf{H}^T \mathbf{R}^{-1} \mathbf{w} \quad (4.3)$$

where,  $\mathbf{H}$  is the design matrix given in equation (4.2),

$\mathbf{R}$  is the covariance matrix of the GPS measurements

and  $\mathbf{w}$  is the misclosure vector.

For a double difference carrier phase position model as described by equation (3.10), the misclosure vector is given as the difference between the computed measurements based on the approximate position and the true measurements, i.e.

$$\mathbf{w} = \begin{bmatrix} (\mathbf{r}_r^1 - \mathbf{r}_r^b) - (\mathbf{r}_m^1 - \mathbf{r}_m^b) - [(\mathbf{f}_r^1 - \mathbf{f}_r^b) - (\mathbf{f}_m^1 - \mathbf{f}_m^b)] + \mathbf{I} \cdot \nabla \Delta N_1 \\ (\mathbf{r}_r^2 - \mathbf{r}_r^b) - (\mathbf{r}_m^2 - \mathbf{r}_m^b) - [(\mathbf{f}_r^2 - \mathbf{f}_r^b) - (\mathbf{f}_m^2 - \mathbf{f}_m^b)] + \mathbf{I} \cdot \nabla \Delta N_2 \\ (\mathbf{r}_r^3 - \mathbf{r}_r^b) - (\mathbf{r}_m^3 - \mathbf{r}_m^b) - [(\mathbf{f}_r^3 - \mathbf{f}_r^b) - (\mathbf{f}_m^3 - \mathbf{f}_m^b)] + \mathbf{I} \cdot \nabla \Delta N_3 \end{bmatrix} \quad (4.4)$$

where,  $b$  is for the base satellite,  $r$  is for the remote receiver and  $m$  is for the monitor receiver.  $\mathbf{r}_j^i$  is the approximate distance in metres to the  $i^{\text{th}}$  satellite from the  $j^{\text{th}}$  receiver calculated using the satellite ephemeris data and the approximate monitor position.  $\mathbf{f}_j^i$  is the integrated carrier phase measurement in metres,  $\lambda$  is the wavelength of the L1 carrier phase signal (19.02 cm) and  $\nabla \Delta N$  is the double difference carrier phase ambiguity in cycles.

For a given set of primary satellites, the approximate correction for each potential ambiguity set can be generated by substituting the selected ambiguity integers into equation (4.4) and the result into equation (4.3). An examination of this procedure reveals that the majority of calculations are redundant and need only be performed once for a given series of potential ambiguity sets. The design matrix ( $\mathbf{H}$ ) does not have to be recalculated because small changes in the remote receiver position (here, on the order of metres) will not change the receiver-satellite vector significantly and thus will have little or no effect on equation (4.2). If instead of relative position, the design matrix was given in terms of attitude parameters as described in Schleppe (1996), the design matrix could change drastically over the search space. The result is that the design matrix must be recalculated for every ambiguity set. The position approach was selected because it is more efficient from a computational point of view. A mechanization procedure for this approach can be defined as follows.

The misclosure vector for the three primary double difference is calculated as in equation (4.4) but without including the ambiguity term, yielding  $\mathbf{w} = (w_1, w_2, w_3)^T$  where  $w_1$ ,  $w_2$  and  $w_3$  are the scalar misclosure values for the three primary double differences. The right side of equation (4.3) excluding the misclosure vector can be written in terms of a series of column vectors ( $\mathbf{x}_1, \mathbf{x}_2, \mathbf{x}_3$ ) known as the three primary solutions. The estimated correction vector or equivalently, the relative monitor-remote vector can be rewritten in terms of the unknown primary ambiguities as

$$\hat{\mathbf{d}} = \begin{bmatrix} \mathbf{x}_1 & \mathbf{x}_2 & \mathbf{x}_3 \end{bmatrix} \begin{bmatrix} w_1 + \mathbf{I}\nabla\Delta N_1 \\ w_2 + \mathbf{I}\nabla\Delta N_2 \\ w_3 + \mathbf{I}\nabla\Delta N_3 \end{bmatrix}. \quad (4.5)$$

The coarse baseline test described in section 4.1.1 can now be applied. The ambiguity set under consideration is rejected if it results in a baseline length that is greater than 30 cm different from the *a priori* length. This test is conservative to avoid potentially rejecting

the correct ambiguity set. The remaining primary ambiguity sets must be tested using the non-primary satellites in a least squares adjustment.

### 4.1.3 Testing of Primary Ambiguity Sets

Once the coarse baseline test has eliminated as many ambiguity sets as possible the remaining satellites can be used to further reduce the number of potential ambiguity sets. The satellites that are not chosen as primary satellites are known as secondary satellites. The following procedure takes advantage of the fact that if the three primary double differences are assumed fixed, the range for any remaining secondary ambiguities is severely restricted. The secondary satellite double difference ambiguities can then be set based upon the primary satellite solution. The design matrix ( $\mathbf{H}$ ) and misclosure vector ( $\mathbf{w}$ ) given in equations (4.2) and (4.4) are augmented to include all double difference measurements. The estimated correction is iteratively calculated using equation (4.3) and subsequently tested under two criteria, the *a priori* baseline length and estimated variance factor.

The final adjusted position of the remote antenna again provides an estimate of the baseline length. The ambiguity set is rejected if this length differs from the *a priori* baseline length by more than 2 cm (based on the accuracy of the carrier phase measurement).

If no biases or blunders (including wrong ambiguities) exist in the measurement data and the observation model is correctly specified then the estimated measurement residuals ( $\hat{\mathbf{r}}$ ) should be zero-mean and have a Gaussian distribution. For an overdetermined solution, the vector of measurement residuals is given by

$$\hat{\mathbf{r}} = \mathbf{H}\hat{\mathbf{d}} + \mathbf{w} . \tag{4.6}$$

The test statistic used to verify the zero-mean, Gaussian behaviour of the measurement residuals is the estimated variance factor given by

$$\hat{\mathbf{s}}_o^2 = \frac{\hat{\mathbf{r}}^T \mathbf{R}^{-1} \hat{\mathbf{r}}}{n} \quad (4.7)$$

where,  $v$  is the degrees of freedom defined as the number of measurements minus the number of parameters,  $\hat{\mathbf{r}}$  is the vector of measurement corrections and  $\mathbf{R}$  is the covariance matrix of the measurements. This value is subjected to the two-tailed Chi-square test ( $\chi^2$ ) given by (Vanicek and Krakiwsky, 1981)

$$\chi^2_{c^2\left(n, \frac{a}{2}\right)} < \frac{n\hat{\mathbf{s}}_o^2}{\mathbf{s}_o^2} < \chi^2_{c^2\left(n, 1-\frac{a}{2}\right)} \quad (4.8)$$

where,  $\mathbf{s}_o^2$  is the *a priori* variance factor in this case assumed to be one. If the test fails then the potential ambiguity set is rejected. This assumes that the error is due to an unmodeled bias, namely an incorrect ambiguity. If the test passes then the primary ambiguity set is stored. If all ambiguity sets have been tested and more than one set still remains then additional GPS measurements will be required to resolve the ambiguities.

Over time, the estimated variance factors of the incorrect ambiguity sets will increase as the effect of the unmodeled bias error causes the distribution of the measurement residuals to drift from the normal distribution due to changing satellite geometry. At this point, the minimum summed variance factor can be compared to the second minimum as follows

$$\frac{\sum_{i=1}^n \hat{\mathbf{r}}_i^T \mathbf{R}_i^{-1} \hat{\mathbf{r}}_i (2nd \text{ min})}{\sum_{i=1}^n \hat{\mathbf{r}}_i^T \mathbf{R}_i^{-1} \hat{\mathbf{r}}_i (1st \text{ min})} > Threshold \quad (4.9)$$

where  $n$  is the number of GPS measurement epochs. This straight summation of the consecutive variance factors is possible if the measurements are assumed uncorrelated from epoch to epoch. The threshold is usually set to around three (Lachapelle, 1995) with a total time interval of about ten seconds.

## 4.2 Aided Ambiguity Resolution

As mentioned in the beginning of this chapter, the definition of the ambiguity search space is extremely important. When there is no *a priori* information regarding the orientation of the system then the remote antenna could be in any direction from the monitor antenna at a distance of the known baseline length. This generates a sphere for the search space centered at the monitor antenna and is known as the non-aided case. If external sensors are available that can provide an estimate of the relative vector between the two antennas, then the ambiguity search space can be drastically reduced (Cannon et al., 1992).

The external sensors can provide an approximate position of the remote antenna with a given uncertainty. The search volume is then centered on this approximate remote antenna position and has dimensions dependent on the external sensor accuracy. The search volumes for the aided and non-aided case are shown in Figure 4.2. The advantage of the smaller search space and corresponding fewer number of ambiguity sets is two fold. First, the computation time to check the potential sets is decreased and second, the probability of picking the right one is increased. This approach can therefore be quicker and more reliable (Harvey and Cannon, 1997).

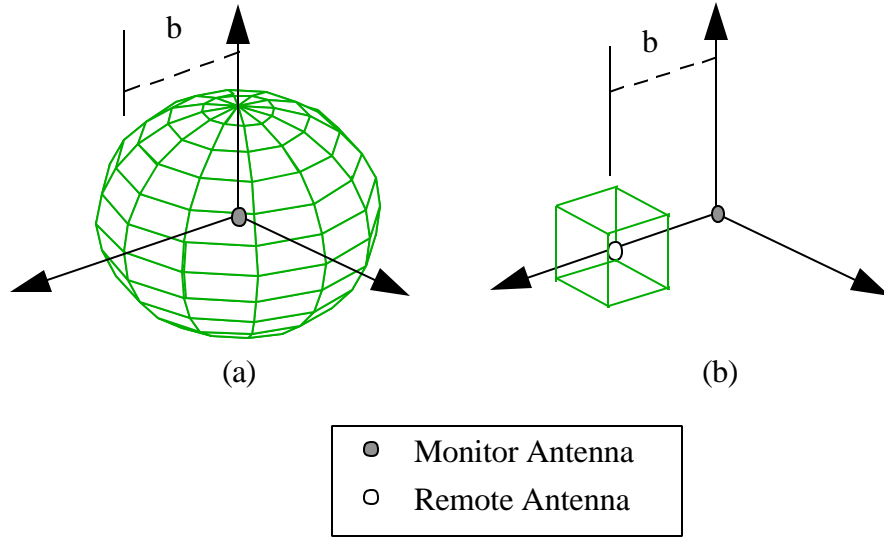


**Figure 4.2 - Ambiguity search volumes for the non-aided (a) and aided (b) case.**

The size of the aided search volume is based on the estimated accuracy of the aiding system which can be expressed in terms of an azimuth ( $\psi$ ), elevation ( $\theta$ ) and baseline length ( $b$ ) standard deviation. The corners of the search cube can then roughly be defined in the local level system as

$$x = x_o \pm 3(\mathbf{s}_b \cdot \sin \mathbf{y} + \mathbf{s}_y \cdot b \cdot \cos \mathbf{y}) \quad (4.10)$$

$$y = y_o \pm 3(\mathbf{s}_b \cdot \cos \mathbf{y} - \mathbf{s}_y \cdot b \cdot \sin \mathbf{y}) \quad (4.11)$$

$$z = z_o \pm 3 \cdot \mathbf{s}_q \cdot b \quad (4.12)$$

where,  $(x_o, y_o, z_o)$  is the approximate position of the remote receiver. The above equations assume that the pitch angle is not extreme which is valid for the vehicular applications dealt with in this research.

For a 1 m baseline, a  $5^\circ$  uncertainty in azimuth and elevation and 5 cm baseline uncertainty, the  $3\sigma$  ambiguity search space would be about  $0.26\text{m}\times 0.26\text{m}\times 0.15\text{m}$  in volume. For the L1 wavelength this corresponds to about eleven possible ambiguity combinations.

## CHAPTER 5

### SENSOR DESCRIPTIONS

The integrated system used in this research consisted of four different types of sensors, namely two GPS receivers, an Andrew 3ARG-D Autogyro™ and a Precision Navigation TCM2-50 electronic compass combined with a bubble level tilt meter. The primary sensor for the integrated system was GPS, in the form of a fixed baseline, dual antenna system with two independent L1 GPS receivers. The single baseline approach is capable of measuring azimuth and pitch as described in Chapter 3. The combination of non-GPS sensors was to be capable of determining the orientation parameters if GPS was unavailable. The choice of the specific sensors was also driven in large part by availability and price.

For this research, an L1 only GPS receiver capable of outputting pseudorange and carrier phase measurements at a minimum rate of 1 Hz was desired (Schleppe, 1996). Two L1-only NovAtel GPS receivers were desired but were not available at the time of testing. Two L1/L2 NovAtel MiLLenniums™ were available with similar L1 performance except for a lower maximum data rate of 4 Hz instead of 10 Hz. The MiLLenniums were used with the L2 disabled. The data rate was set to 1 Hz to cut down on the processing load of the logging computer and avoid missing or corrupting the FOG measurements which had no checksum. This also saved processing power for potential real-time implementation in the future. Model 501 NovAtel antennas were used for both receivers and were mounted facing the same direction to cut down on antenna phase variation errors. The NovAtel also had a TTL I/O connector which could be used in time matching operations. The implementation of the hardware is discussed in more detail in Chapter 6.

In terms of the non-GPS sensors, an Andrew Autogyro™ which determines vehicular angular rate was used and was previously tested by Hayashi (1996) and Zhang (1998). The Autogyro™ has good short term stability but suffers from bias drift making it

unsuitable for long term azimuth determination. Other problems associated with the gyro include errors due to the gyro being misaligned with respect to the local level plane and its inability to estimate pitch. An investigation into other relatively low cost (~\$500 to \$1000 CAN) sensors resulted in the selection of the Precision Navigation TCM2-50, consisting of an electronic compass capable of determining azimuth with respect to magnetic North and a two-axis bubble tilt meter. The compass provided long term stability in the azimuth while the tilt meter provided pitch and roll estimates which could be used to correct for the gyro misalignment. The absolute noisy measurements of the compass and tilt meter also provided a rough estimate of the current platform orientation which could be used to limit the size of the GPS carrier phase ambiguity search space (see Chapter 4) and to initialize the filter.

## **5.1 Andrew Autogyro™**

The Andrew Autogyro™ is a single axis fiber-optic gyro (FOG) angular rate sensor designed and built by Andrew Corporation (Andrew Corp., 1994). A FOG consists of a coil of fiber-optic cable and a coherent light source, the beam of which is passed through a beamsplitter and then directed through either end of the fiber-optic coil. If the coil is not rotating, the two beams will be in phase when they exit the ends of the cable. If the coil is rotated during this period, the two beams will have different path lengths and thus will be out of phase when they exit either end of the coil. The interference pattern formed when the two beams are recombined is used to determine the amount of rotation experienced by the coil. A good description of this technique is given by Liu and Adams (1990) and Martinelli and Ikeda (1995). The specifications of the gyro are given in the Andrew Autogyro™ Manual (Andrew Corp., 1994) and are listed in Table 5.1.

The gyro outputs a three-byte data packet every 0.1 s in RS-232 format at 9600 Baud. The first bit of every byte is a sync bit, having a value of one for the first byte and zero for the second and third bytes. The second bit of the first byte is an operational indicator,

a value of one representing failure and a zero indicating normal operation while the remaining twenty bits are for data. The first twelve data bits contain the angular rotation data while the remaining eight form a temperature record.

**Table 5.1 - Andrew Autogyro™ 3ARG-D specifications.**

	DESCRIPTION	SPECIFICATION
PERFORMANCE	Input Rotation Rate	$\pm 100$ deg/s
	Minimum Detectable Rotation Rate (100 Hz Bandwidth)	$\pm 0.02$ deg/s (Angle Random Walk)
	Bias Drift (Stable Temperature)	0.005 deg/s, rms
	Scale Factor Nonlinearity	0.25%, rms
	Scale Factor Temperature Stability (Over Temperature Range)	0.5%, rms
PHYSICAL	Dimensions	77 mm (diameter) $\times$ 88 mm
	Weight	0.63 kg
	Operating Temperature	-40 °C to +70°C
INTERFACE	Power	+9 to +16 VDC, 0.65 A
	Output	RS-232E, 9600 Baud

The sync bit approach is intended to ensure proper reception of the data but is not very robust. As an example, consider a situation where the first and second bytes are received correctly but the third byte is corrupted. If the first bit of the third byte is a one, then all information in the three bytes would be rejected. The problem is that the corrupted byte could just as easily have a zero as the first bit, in which case the byte would be accepted and the incorrect data extracted in the normal manner. There is also no provision for RS-

232 hardware (CTS/RTS) or software (XON/XOFF) handshake protocol which would help eliminate data transmission problems.

The data output from the gyro is the scaled incremental angular displacement over 0.1 s, equivalent to the average rotation rate over that period (Andrew Corp., 1994). Similar to Abbot (1995) and McLellan (1992), the gyro output can be modeled with a scale factor ( $s$ ) and measurement bias ( $d_{fog}$ ). The bias in the angular rate measurement results in an azimuth drift error as the bias is integrated over time. The rotation rate in the plane of the gyro for the 0.1 s period is given by

$$\mathbf{w}_{fog} = s(\mathbf{w}_{raw} - d_{fog}) \quad (5.1)$$

where,  $s$  is the scale factor [ $^{\circ}$ /bit],

$d_{fog}$  is the gyro rate bias estimate [bit/s],

$\omega_{raw}$  is the raw 12-bit gyro measurement [bit/s]

and  $\omega_{fog}$  is the actual rotation rate in the gyro plane for the 0.1 s period [ $^{\circ}$ /s].

The effects of g-sensitivity and cross-axis sensitivity have been ignored for the same reasons as in Abbot (1995), namely the effects are expected to be relatively small and only high-end gyroscope manufacturers publish these specifications. McLellan (1992) also included a term to account for earth rate ( $\omega_e = 0.004$   $^{\circ}$ /s), but this value was an order of magnitude less than the minimum detectable rotation rate in Table 5.1 and was ignored.

If the gyro plane remains fixed and the initial heading is known, the angular displacement at any future time can be determined by summing all consecutive gyro outputs up until the desired time. This realization is complicated by the fact that both the bias and scale factor are functions of temperature as described in Hayashi (1996). As well, since the

purpose of the gyro is to determine the azimuth of a vehicle in the horizontal plane, any inclination of the gyro plane with respect to the horizontal must be taken into account. This situation would develop for the case of a gyro rigidly mounted to a vehicle that was experiencing body roll or pitch. The temperature effects were assumed to be repeatable and calibration was used to remove much of this error. The bias was assumed to have a random walk component which was estimated in the filter while the tilt meter estimates of pitch and roll were used to account for the misalignment of the gyro plane with respect to the horizontal plane. The temperature and misalignment problems are now addressed in more detail.

### 5.1.1 Andrew Autogyro™ Temperature Effects

The scale factor and bias values shown in equation (5.1) are functions of temperature. Andrew Corporation supplies a bias temperature correction table for every gyro manufactured but does not provide any temperature variation for the scale factor. The factory calibrated bias compensation values were provided in an ASCII data file by Andrew Corp. and are plotted in Figure 5.1.

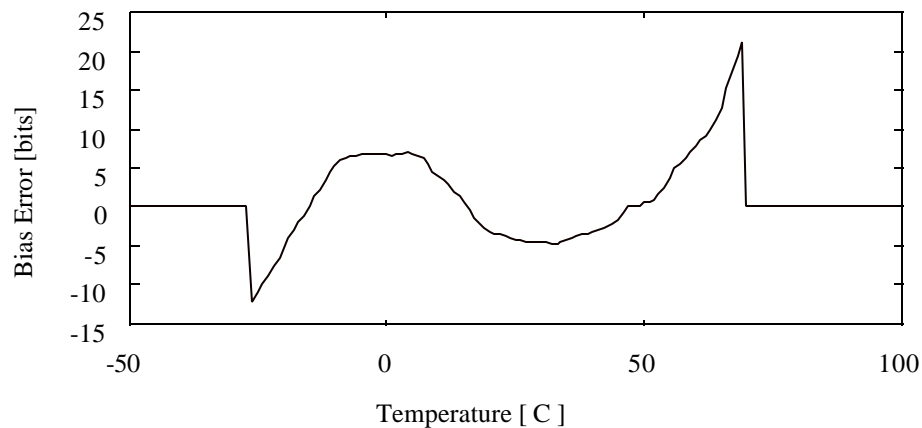


**Figure 5.1 - Factory calibrated bias temperature compensation values.**

The nominal scale factor for a 12 bit quantization and a maximum rate of  $\pm 100$  °/s is 0.048828 [°/s]/bit. Hayashi (1996) showed significant deviation from this number over the temperature range and suggested a quadratic polynomial, the coefficients of which were determined from experimental data in the range 24°C to 56°C. Unfortunately, the majority of this research was conducted at temperatures which were below this experimental range. A new cubic polynomial was created through comparison of the raw integrated FOG output with a high quality INS/GPS system. The temperature ( $T$ ) dependent scale factor  $s(T)$  for this research was then taken as

$$s(T) = b_0 + b_1 \cdot T + b_2 \cdot T^2 \quad (5.2)$$

where,  $T$  is the temperature in °C, and  $b_0$ ,  $b_1$  and  $b_2$  are the coefficients given by

$$b_0 = 0.0486972010810$$

$$b_1 = -0.0003749484972$$

$$b_2 = 0.0000142854916$$

The polynomial used by Hayashi (1996) and the polynomial used for this research are shown in Figure 5.2. The temperatures recorded by the gyro for the test period showed a range of between 15°C and 23°C. Examination of Figure 5.3 reveals that there is significant deviation between the two polynomials at this temperature range. This is again attributable to the fact that the experimental data used in the Hayashi (1996) polynomial did not extend into this temperature region. Both polynomials were applied to the raw integrated FOG output to test their relative effectiveness with the results shown in Chapter 7.

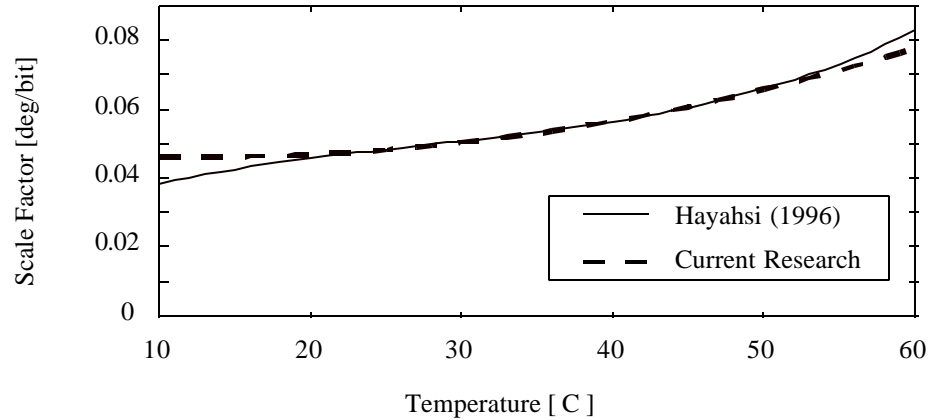


**Figure 5.2 - Scale factor polynomials to account for temperature effects.**

### 5.1.2 Misalignment of FOG Plane with Respect to Horizontal Plane

The purpose of the FOG is to measure the azimuth angular rotation in the horizon plane ( $\omega_\psi$ ). If the FOG is misaligned with respect to the horizon plane it will only detect the vector component of the azimuth rate that can be projected from the horizon spin axis ( $\omega_\psi$ ) to the gyro spin axis ( $\omega_{fog}$ ). The FOG will also detect any other components of rotation that can be projected onto its spin axis, even if they are perpendicular to the azimuth rate. This situation is shown in Figure 5.3.

The horizon plane is defined by the  $X$  and  $Y$  axes, where  $Y$  is along the azimuth of the vehicle,  $Z$  is in the up direction as defined by the local level frame and  $X$  completes the right-handed system. The FOG is rigidly fixed to the vehicle frame, which is defined by the  $x_{fog}$ ,  $y_{fog}$  and  $z_{fog}$  axes, where the rotation detected by the FOG ( $\omega_{fog}$ ) would be in the plane defined by the  $x_{fog}$  and  $y_{fog}$  axes. The pitch rotation rate ( $\omega_\theta$ ) and the roll rotation rate ( $\omega_\phi$ ) are perpendicular to the desired azimuth rate ( $\omega_\psi$ ) but components of each can be detected by the gyro. The angles  $\gamma$  and  $\beta$  are defined by the pitch and roll of the vehicle obtained from the tilt meter.

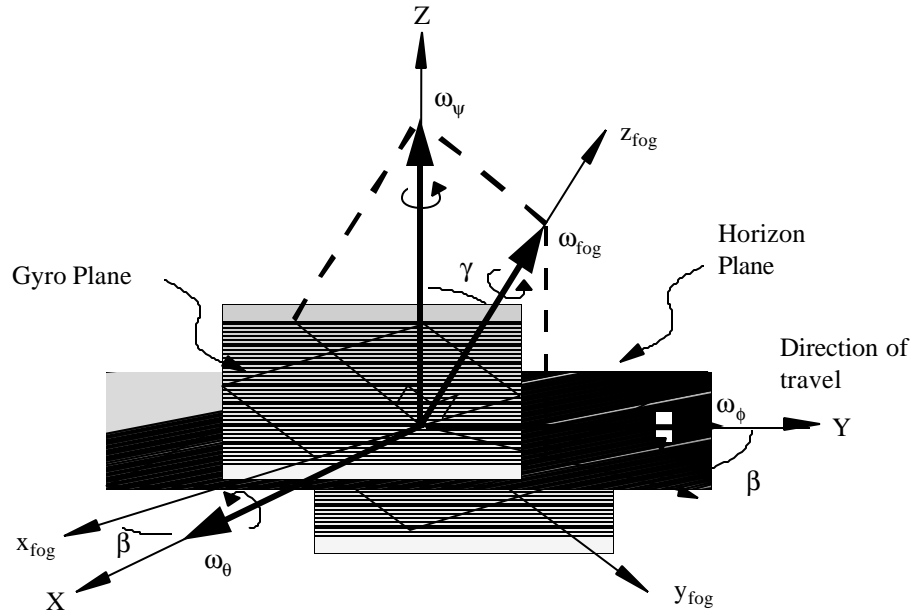


**Figure 5.3 - Misalignment of FOG plane with respect to horizon plane.**

The angular rate measured by the FOG and shown in Figure 5.3, can be written similar to Zhang (1997) as

$$\mathbf{w}_{fog} = \mathbf{w}_y \cos \mathbf{g} + \mathbf{w}_f \cos \mathbf{b} \sin \mathbf{g} + \mathbf{w}_q \sin \mathbf{b} \sin \mathbf{g} \quad (5.3)$$

which can be rearranged in terms of the desired azimuth rate as

$$\mathbf{w}_y = \frac{\mathbf{w}_{fog}}{\cos \mathbf{g}} - \left[ \frac{\mathbf{w}_f \cos \mathbf{b} \sin \mathbf{g} + \mathbf{w}_q \sin \mathbf{b} \sin \mathbf{g}}{\cos \mathbf{g}} \right]. \quad (5.4)$$

To obtain the proper azimuth rate, the FOG-detected rate must be corrected for the misalignment angle  $\gamma$  and for any contribution due to  $\omega_\theta$  and  $\omega_\phi$ . The pitch and roll estimates provided by the tilt meter can be used to generate the values of  $\gamma$  and  $\beta$ , but with the current hardware there is no way to estimate the roll and pitch angular rates and

thus no compensation for the term in the brackets of equation (5.4) is possible. The magnitude of this error contribution is examined later. The angles  $\gamma$  and  $\beta$  can be equated as follows (St. Lawrence, 1993) where the unit vector representing the FOG spin axis is written in terms of three direction cosines  $(l,m,n)$  related to the  $X,Y$  and  $Z$  axes respectively where

$$l^2 + m^2 + n^2 = 1 \quad (5.5)$$

Given that the angle between the spin axis and the  $Z$  axis is  $\gamma$ , the roll angle is  $\Delta\phi$  and the pitch angle is  $\Delta\theta$ , then the spin axis unit vector can be represented as shown in Figure 5.4.

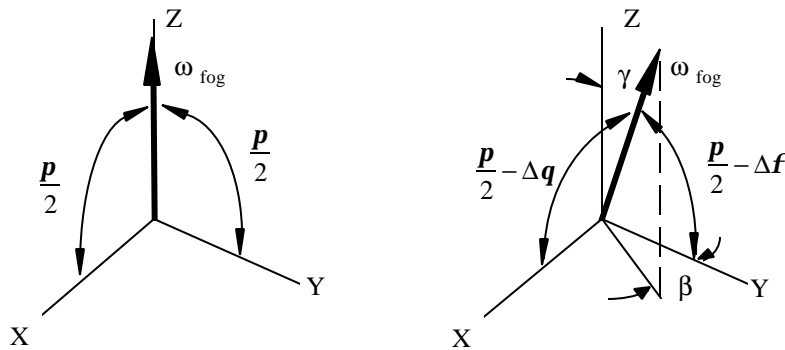


**Figure 5.4 - Direction cosine representation of FOG spin axis ( $\omega_{fog}$ ) for a roll angle of  $Df$  and a pitch angle of  $Dq$ .**

The direction cosines corresponding to Figure 5.4 which define the spin axis unit vector with respect to the  $(X,Y,Z)$  frame are

$$l = \cos\left(\frac{p}{2} - \Delta q\right), \quad m = \cos\left(\frac{p}{2} - \Delta f\right), \quad n = \cos(\gamma). \quad (5.6)$$

Using some trigonometric identities, these direction cosines can be rewritten as

$$l = \sin(\Delta\mathbf{q}), \quad m = \sin(\Delta\mathbf{f}), \quad n = \cos(\mathbf{g}). \quad (5.7)$$

Using the small angle approximation,  $\sin(x) \approx x$ , and equation (5.7), equation (5.5) can be rewritten as

$$\Delta\mathbf{q}^2 + \Delta\mathbf{f}^2 + \cos^2(\mathbf{g}) = 1 \quad (5.8)$$

or

$$\cos(\mathbf{g}) = \left(1 - \Delta\mathbf{q}^2 - \Delta\mathbf{f}^2\right)^{\frac{1}{2}}. \quad (5.9)$$

The angle ( $\beta$ ) between the true azimuth and projected tilt vector in the horizon plane is given by (ibid.)

$$\mathbf{b} = \tan^{-1}\left(\frac{\Delta\mathbf{q}}{\Delta\mathbf{f}}\right). \quad (5.10)$$

The best estimate of the azimuth angular rate over the 0.1 s period ( $\omega_\psi$ ) is then taken by combining the result of equations (5.9), (5.4) and (5.1) to give

$$\mathbf{w}_y = \frac{s(\mathbf{w}_{raw} - d_{fog})}{(1 - \Delta\mathbf{q}^2 - \Delta\mathbf{f}^2)^{\frac{1}{2}}} \quad (5.11)$$

where the components of the gyro measurement due to pitch and/or roll angular rotation rates have been left out. Again, these rates give rise to the bracketed term in equation (5.4) based on Figure 5.3 and it is important to understand the effect that ignoring these rates could possibly have on the angular displacement accuracy. The error term as given in equation (5.4) is

$$rate\ error = \left[ \frac{w_f \cos b \sin g + w_q \sin b \sin g}{\cos g} \right]. \quad (5.12)$$

The problem with the rate error as described in equation (5.12) is that it is a function of four variables ( $\omega_\psi$ ,  $\omega_\theta$ ,  $\gamma$  and  $\beta$ ) and therefore difficult to plot. To remove some of the variables, the pitch and azimuth angular rates will be assumed non-zero and equal in value ( $\omega = \omega_\theta = \omega_\phi$ ) which reduces equation (5.12) to

$$rate\ error = w \tan g (\cos b + \sin b) \quad (5.13)$$

where the term in the brackets has a maximum value at  $\beta = 45^\circ$ . By setting the value of  $\beta$  at its maximum value, it is possible to plot the induced error as a function of tilt angle ( $\gamma$ ) for a series of angular rate ( $\omega$ ) values as shown in Figure 5.5.

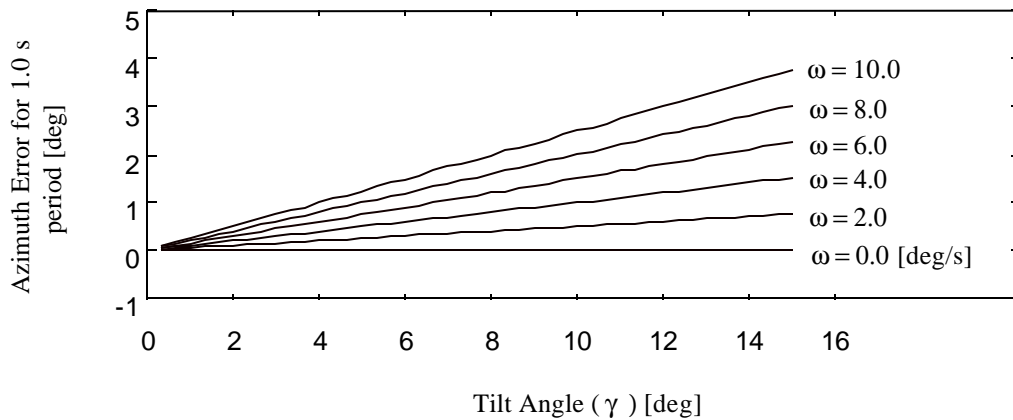


**Figure 5.5 - Angular displacement error over 1.0 s period given a misalignment angle ( $g$ ) and assuming equal pitch and roll angular rates ( $w$ ).**

It can be seen that for the case of zero misalignment ( $\gamma = 0$ ) or zero angular rate ( $\omega = 0$ ) there is no induced error in the azimuth angular displacement calculation. However, for

the extreme case of a  $15^\circ$  tilt angle and a  $10^\circ/\text{s}$  pitch and roll rotation rate maintained for a full second the induced error would be  $3.4^\circ$ . For the vehicular application in this research, this type of error would be most evident when the vehicle was turning or accelerating. For a vehicle traveling along a straight road, the roll and pitch rotation rates would probably be due to bumps or imperfections in the road and the time constant would be significantly shorter. The result would be that over time the rate errors would tend to cancel out. This is equivalent to assuming that the rotation rate errors are a white noise sequence such that integration will give a random walk behaviour (Gelb, 1974).

## **5.2 Precision Navigation Inc. TCM2-50**

The Precision Navigation Inc. TCM2-50 is a combined electronic compass and twin axis bubble level tilt meter. The TCM2-50 was chosen for this application because it is capable of estimating three different orientation parameters, namely azimuth, pitch and roll. The measurements, being based on either the earth's magnetic or gravity field which can be considered invariant, are highly stable in the long term even though other error sources may degrade accuracy in the short term. The TCM2-50 was rigidly mounted beside the FOG and subsequently experienced the same roll and pitch. Estimates of the roll ( $\Delta\phi_{\text{tcm}}$ ) and pitch ( $\Delta\theta_{\text{tcm}}$ ) from the tilt meter could therefore be used to correct the FOG as explained in section 5.1.2. Physically, the TCM2-50 is a 5 cm by 6.5 cm circuit board mounted with three orthogonal magnetometers, a bubble level and support electronics. The open circuit board was enclosed in a plastic box with nylon offsets and aluminum screws to avoid any magnetic field interference.

The specifications as provided by Precision Navigation are shown in Table 5.2 (Precision Navigation Inc., 1997).

**Table 5.2 - Precision Navigation TCM2-50 specifications.**

	Description	Specification
HEADING	Accuracy when level	$\pm 1.0^\circ$ RMS
	Accuracy when tilted	$\pm 1.5^\circ$ RMS
	Resolution	$0.1^\circ$
	Repeatability	$\pm 0.3^\circ$
TILT	Accuracy	$\pm 0.4^\circ$
	Resolution	$0.3^\circ$
	Repeatability	$\pm 0.3^\circ$
	Range	$\pm 50^\circ$
TEMPERATURE	Accuracy	$\pm 1^\circ$ C
	Resolution	$\pm 1^\circ$ C
	Range	$-20^\circ$ to $70^\circ$ C
PHYSICAL	Dimensions	635mm $\times$ 508mm $\times$ 318mm
	Weight	0.5 kg
	Operating Temperature	$-20^\circ$ to $70^\circ$ C
INTERFACE	Power	6 to 18 VDC, 20 mA
	Digital	RS-232, NMEA 0183
	Analog	0-5 V linear, quadrature

The TCM2-50 is capable of outputting TTL analog or RS-232 ASCII data at up to 40 Hz. The RS-232 interface was chosen because the TTL analog output did not include tilt information. The output rate was set to 10 Hz to match the output of the FOG and was transmitted at 9600 Baud through an RS-232 interface equipped with a DB-9 connector

for interfacing with a PC. The ASCII output included azimuth, roll, pitch, temperature and a magnetic anomaly alarm flag. Unlike the Autogyro™, the data messages contained a 1-byte XOR checksum to eliminate corrupted data. The TCM2-50 was set to continuous mode whereby the data messages were immediately enabled and output at 10 Hz after power-up.

### **5.2.1 Electronic Compass**

The TCM2 contains a triad of orthogonal magnetometers that can detect the magnitude of the local magnetic field. If this field is due solely to the magnetic field of the earth then the horizontal component of the resultant vector represents magnetic North or true North if corrected for magnetic declination. If the orientation of the magnetometer triad is known with respect to the vertical and the platform, then the azimuth of the vehicle can be determined. The TCM2-50 board was mounted such that the magnetometer triad had one axis aligned with the longitudinal axis of the vehicle, another with the vertical axis and the final one completing a right-handed system. The deflection from the vertical was given by the tilt meter estimates of roll and pitch, similar to the process of correcting the deflection of the FOG spin axis as described in section 5.1.2.

The dominant error source for the electronic compass is magnetic field anomalies which corrupt the magnetic field measurements. These anomalies can be divided into two categories, static and random. Static, in this sense, refers to magnetic field contributions that are constant or fixed with respect to the TCM2-50 magnetometers. For a TCM2-50 mounted in a car, the car would represent a large but constant magnetic field. The advantage to static magnetic field disturbances is that they can in large part be calibrated and removed (Precision Navigation Inc., 1997). Random anomalies represent any magnetic field disturbances which cannot be calibrated. If the car in the previous example was used in kinematic mode, then the fields created by such items as passing cars or trucks, maintenance hole covers, underground power lines and even metal light posts would be considered random and could all adversely affect the compass reading.

To effectively use the TCM2-50, the static field of the platform must be calibrated out after the initial mounting (Precision Navigation Inc., 1997). Precision Navigation has incorporated a calibration procedure for the TCM2-50 that includes a calibration rating out of nine for both the horizontal and vertical directions. The procedure involves completing one or two circles over the course of several minutes while changing the roll and pitch as much as possible. The calibration area should be free from random magnetic field sources such that only the vehicle and earth magnetic fields are detectable. With calibration complete, the magnetic anomaly detector (MAD) feature of the TCM2 can be enabled. The TCM2 utilizes an algorithm that compares the instantaneous magnetic field against the stored static reference. If significant deviations are noted then the MAD flag in the output message is raised.

During early testing, it was found that events such as opening the car door or even engaging the rear window defrost could trigger the MAD. This was complicated by the fact that at one time, three out of four doors would trigger the alarm, but the fourth would not. A possible reason for this behaviour was the difficulty in obtaining the pitch and roll angles needed for vertical calibration while driving in a short circle with the TCM2 mounted to the vehicle. The final calibration procedure developed over the course of four separate days of testing resulted in a perfect horizontal calibration score, but only a 5 out of 9 for the vertical. After these initial tests, all measurements taken by the compass and the ability to detect random anomalies were treated with some skepticism. Results using the MAD are shown in more detail in Chapter 7.

### 5.2.2 Tilt Meter

The tilt meter portion of the TCM2 is realized by an enclosed vial, roughly half-filled with a conducting liquid. Equally spaced on the inside wall of the vial are four vertical electrodes. When the TCM2 is tilted then the electrodes will have different immersed depths and different electrical properties. The two orthogonal tilt values are determined by the voltage differential across opposite pairs of electrodes. The TCM2 tilt meter is referenced to the gravity vector and is highly stable in the long term. During initial testing, the largest error source for the tilt meter was the inability of the TCM2 to distinguish the gravity vector ( $\mathbf{g}$ ) from other accelerations due to motion ( $\mathbf{a}_v$ ). The result was that the liquid surface could be tilted from the true horizontal by an angle  $\eta$ , as shown in Figure 5.6.

The vector sum of the gravity vector ( $\mathbf{g}$ ) and the acceleration vector due to vehicle motion ( $\mathbf{a}_v$ ) in Figure 5.6 gives a net acceleration ( $\mathbf{a}_n$ ) which will be perpendicular to the surface of the liquid.

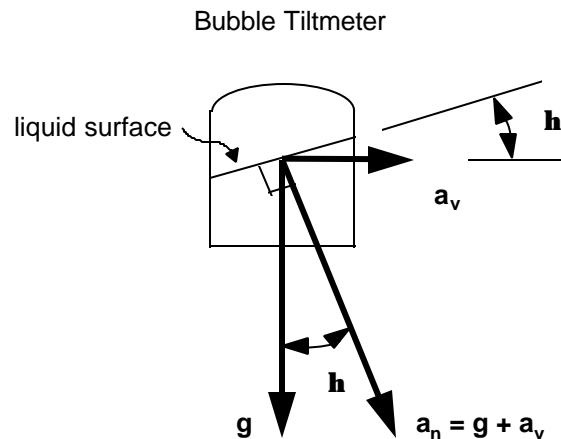


**Figure 5.6 - Induced horizontal reference error ( $h$ ) due to vehicle accelerations.**

It can be seen that the bubble tilt meter could indicate a tilt angle even when the TCM2 is aligned with the vertical if accelerations are present. The angle  $\eta$  can be equated as

$$\mathbf{h} = \tan^{-1}\left(\frac{\mathbf{a}_v}{\mathbf{g}}\right) \quad (5.14)$$

The tilt error due to vehicle acceleration could therefore be estimated if the vehicle accelerations were available. An examination of Figure 5.6 reveals that the tilt error will occur along the axis perpendicular to the vehicle acceleration. The along-track acceleration of the vehicle corresponds to a pitch error, while the cross-track acceleration corresponds to a roll error.

This treatment of the error due to vehicle acceleration assumes an impulse acceleration results in an impulse error in the tilt angle. In reality, the surface of the liquid will have some causal behaviour that should be modeled along the lines of a damped, possibly harmonic, oscillator. The simplified treatment was adopted because the only available source for determining accelerations was the integrated Doppler of the 1 Hz GPS measurements while the frequency of the vehicle accelerations can be assumed to reach 10 Hz (Skaloud, 1995). The sampling theorem would preclude eliminating these higher frequency components with GPS alone unless the logging system could handle a higher data rate. The effectiveness of the GPS acceleration corrections and the assumptions regarding cross-track and along-track corrections affecting roll and pitch respectively are examined in more detail in Chapter 7.

## **CHAPTER 6**

### **SYSTEM REALIZATION**

Following sensor selection, the next requirement was to assemble the hardware and associated logging software to accurately time-tag and store all data collected during the test period. For this research, there was no requirement for real-time operation as processing was to be done in post-mission. This removed the restriction of having to log all four sensors to the same computer. A post-mission processing software package based on the Kalman filter algorithm described in Chapter 2 was developed to optimally estimate the orientation parameters from the data. The software was written so that only the data logging portion would have to be redeveloped if a real-time system was desired. For real-time operation, the programming routines which input the sensor data from different file streams would have to be replaced by new routines which would collect the sensor data directly and place it in a form of a circle buffer for use by the processing routines. The addition of the GPS acceleration derived correction for the tilt meter induced a one-second lag in the data processing and would consequently involve the same delay if used in real-time operation. Verification of proper system operation was facilitated through use of a post-mission approach since data logging (hardware) versus data processing (software) errors could be isolated.

#### **6.1 Hardware Architecture**

The purpose of the hardware set-up was to deliver one accurately time-tagged data file for the FOG, TCM2 and each of the two GPS receivers. The GPS receivers were configured to provide pseudorange, carrier phase and Doppler measurements at 1 Hz using a NovAtel RGEC compressed binary format message (NovAtel, 1995). The receivers were also configured to output individual satellite orbital and clock information contained in the broadcast navigation message. Receiver output for this information was in the form of a NovAtel REPB binary ephemeris message (NovAtel, 1995) whenever a

new satellite was acquired or a currently held ephemeris was updated. The PC interface protocol was RS-232 using a 57600 Baud rate and a manufacturer supplied ‘Y’ type null-modem cable. An advantage of GPS is that the measurements are time-stamped with respect to the GPS atomic time standard. The GPS time of measurement, limited to 340 ns (95%) in accuracy by SA (Van Graas and Braasch, 1994), is included in the RGEC record and simplifies data collection since external timing hardware is not required. The NovAtel receiver came equipped with a TTL I/O port that was used to provide precision timing information for the other sensors as described below.

The FOG output consisted of the incremental 10 Hz angular rate at 9600 Baud on an RS-232 interface. The TCM2 was designed with more operational flexibility, allowing for either analog output or digital RS-232 output at various Baud rates. As discussed in Chapter 5, the chosen TCM2 configuration was RS-232 10 Hz digital data using a 9600 Baud rate to match that of the FOG. The interface cables for both the TCM2 and FOG were non-standard, requiring 12 V power, and had to be either modified or constructed to ensure proper operation. The FOG interface cable used a subminiature DB-9 connector at the sensor with a non-standard wiring pin assignment as shown in Figure 6.1 (Andrew Corp., 1994).

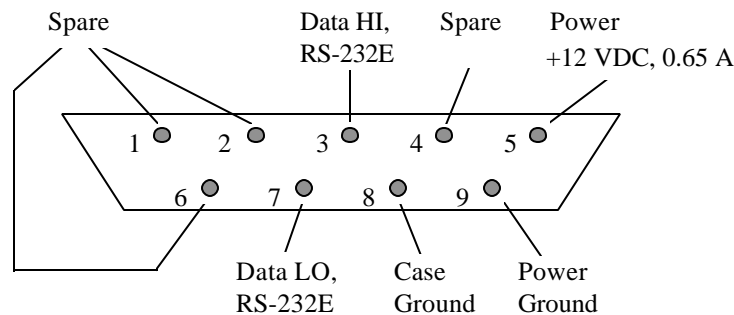


**Figure 6.1 - Pin assignment for Andrew Autogyro™ DB-9 interface.**

From the sensor end the interface cable was split into a power and a data transmission cable. The data transmission cable terminated at the PC in the form of a DB-9 connector wired to RS-232 standard to match the COM serial interface. The power cable was run to a 12 V power supply in the form of a car battery. The TCM2 interface cable was wired in a similar fashion except for a unique connector at the sensor end with a pin assignment as shown in Figure 6.2 (Precision Navigation Inc., 1997).

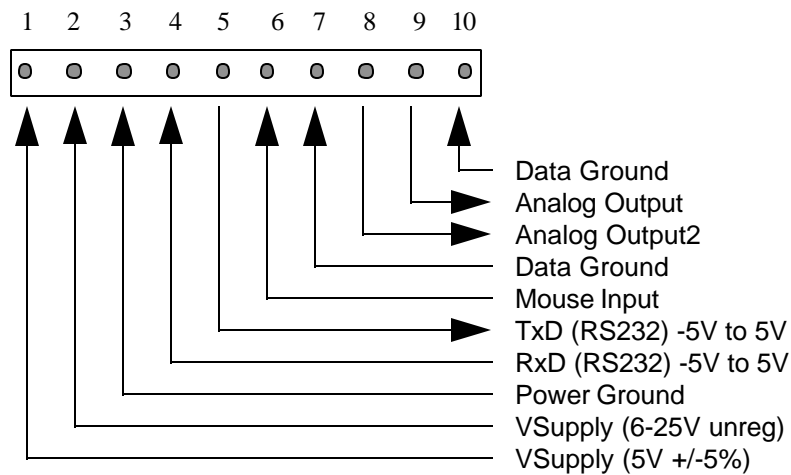


**Figure 6.2 - Pin assignment for Precision Navigation TCM2-50 connector.**

To capture the data streams from the four different sensors, two Pentium laptops with one COM port each and equipped with PCMCIA Quatech SSP-100 RS-232 serial port adapters were used. Each Pentium was responsible for logging data from two sensors, namely one GPS receiver and either the TCM2 or FOG.

The FOG and TCM2 data streams were output according to the independent local sensor oscillator, and were therefore asynchronous with respect to GPS time. To align the FOG and TCM2 measurements with GPS time, the data messages had to be time-tagged by the PC. An interrupt driven service routine written in the C programming language was available from Andrew Corp. to convert the FOG data stream into an ASCII record. This

routine was modified by Hayashi (1996) to allow for software buffering of the FOG data while other operations were taking place. It was further modified by the author to time-tag the record using the PC clock. Further work at the University of Calgary resulted in a series of routines to time-tag the TCM2 records with the PC clock as well. The offset between the PC clock and GPS time was determined by sending an active low pulse every 5 s through the PC parallel port strobe pin to the mark input I/O connector on the GPS receiver. The receiver was configured to output a data message containing the arrival time of the pulse in GPS time. The offset was applied to the PC time-stamp for the TCM2 and FOG records by the interrupt service routines. The dominant error source for this operation was the 55 ms quantization of the PC clock. The equipment set-up is shown in Figure 6.3.

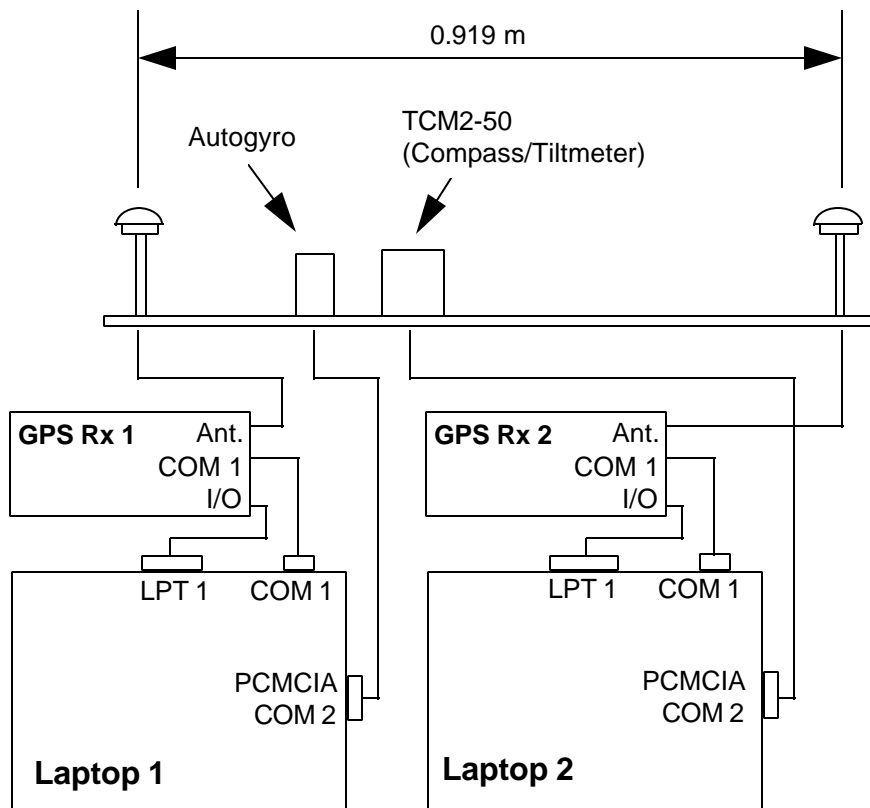


**Figure 6.3 - Equipment diagram showing the four sensors and two PCs.**

A picture of the hardware setup is shown in Figure 6.4 where the GPS antennas, TCM2 and Autogyro™ are visible on the top of the car. Figure 6.5 shows the wiring used to connect the PC and the GPS receiver I/O port for time tagging operations.

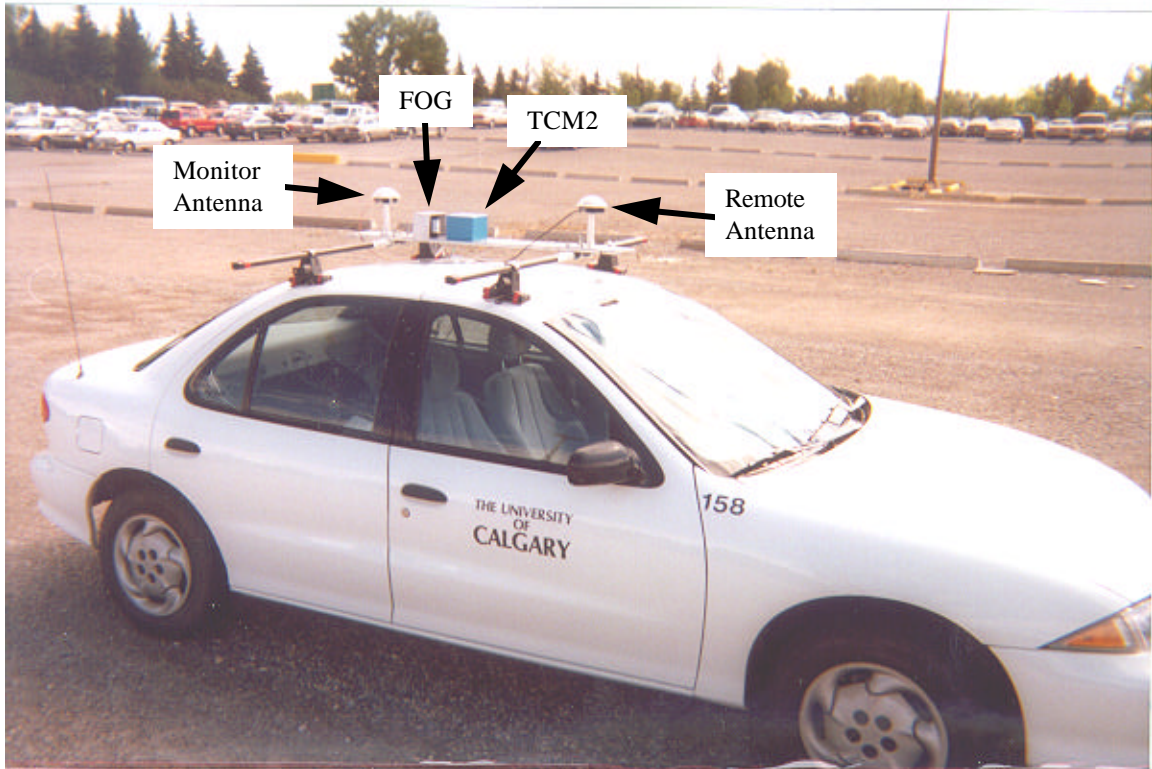


**Figure 6.4 - Sensor array rigidly mounted on a test vehicle.**

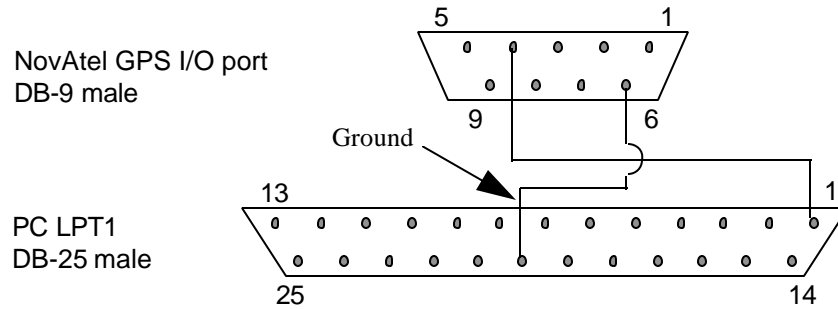


**Figure 6.5 - Mark-time input cable wiring diagram for determining offset between PC clock and GPS time using parallel port strobe pin.**

## 6.2 Software Architecture

The post-mission software package developed for this research consisted of all routines necessary to decode the sensor data and optimally estimate a series of parameters using a Kalman filter. The ambiguity resolution routines used in the software were taken from HEAD™ (Sun and Cannon, 1995) and slightly modified while all other routines were written by the author. The filter design was based on a feed-back aided sensor approach as described in Chapter 2. Continuous measurements from the FOG and tilt meter were used to generate a 10 Hz nominal trajectory comprised of azimuth ( $\psi_{nom}$ ) and pitch ( $\theta_{nom}$ ). GPS measurements, which could suffer from line-of-sight blockages, and compass measurements, suffering from magnetic anomalies, were used in a 1 Hz Kalman filter to estimate errors in the nominal trajectory. The gyro measurement rate bias error and compass magnetic field error were also included as states for estimation.

In order to use GPS measurements in the filter and correct the tilt meter for acceleration, the software had to resolve GPS carrier phase ambiguities and determine the vehicle position and velocity. The ambiguities were resolved using the techniques discussed in

Chapter 4. Pseudorange and Doppler measurements collected at the GPS monitor antenna were used in an epoch-by-epoch least-squares estimation procedure to determine the position and velocity of the antenna and hence the vehicle. In the next two sections the estimation of vehicle position and velocity along with filter design will be covered in detail. The full software architecture is illustrated in Figure 6.6. The filter architecture on the right-hand side of the diagram follows the feed-back aided sensor approach presented in Figure 2.3. The variables listed in Figure 6.6 are repeated below along with the chapter they were first mentioned.

$\omega_{\text{raw}}$	[Chpt 5]	raw gyro measurement [bits/s]
$\Delta\theta_{\text{tcm}}$	[Chpt 5]	TCM2 pitch measurement, corrected for acceleration if GPS is available [°]
$\Delta\phi_{\text{tcm}}$	[Chpt 5]	TCM2 roll measurement, corrected for acceleration if GPS is available [°]
$\mathbf{z}_{\text{tcm}}$	[Chpt 2]	TCM2 compass measurement (Filter input) [°]
$\mathbf{z}_{\text{GPS}}$	[Chpt 2]	vector of GPS carrier phase measurements with fixed ambiguities [m]
$\Phi_{\text{L}}$	[Chpt 3]	Latitude from GPS single point solution [°]
$\Lambda$	[Chpt 3]	Longitude from GPS single point solution [°]
$\mathbf{x}_o$	[Chpt 2]	Nominal trajectory calculated from gyro and tilt meter pitch [°]
$\mathbf{h}(\mathbf{x}_o)$	[Chpt 2]	Predicted measurements given by evaluating $\mathbf{h}$ at $\mathbf{x}_o$ [m]
$\hat{\mathbf{x}}_k^{(+)}$	[Chpt 2]	Optimal estimate of azimuth and pitch at time $k$ [°]
$\hat{\mathbf{d}}_k^{(+)}$	[Chpt 2]	Optimal estimate of correction to nominal trajectory at time $k$ [°]
$\hat{\mathbf{d}}_k^{(-)}$	[Chpt 2]	Optimal estimate of predicted correction for time $k$ [°]

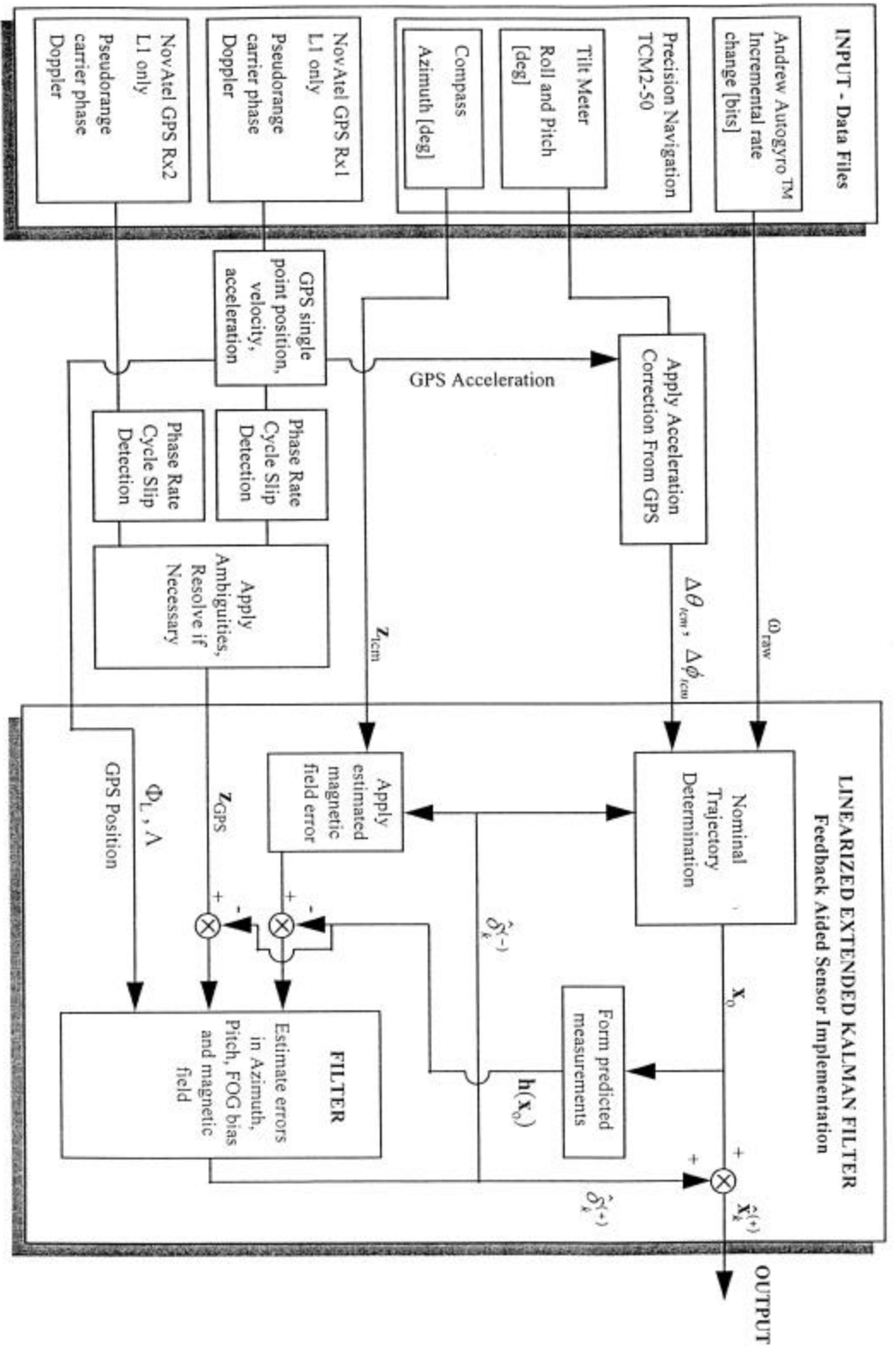


Figure 6.6 - Software architecture with extended Kalman filter.

### 6.2.1 Estimation of Vehicle Position and Velocity using Single-Point GPS

The vehicle position was needed during ambiguity resolution to define the ambiguity search space, determine the satellite unit vectors and to calculate the transformation from the WGS-84 Earth-centered, Earth-fixed (ECEF) frame used by GPS to the horizon based local level (LL) frame. Accelerations derived from the estimated vehicle velocity were used to correct the tilt meter results. A batch least squares adjustment using the monitor antenna pseudorange and Doppler measurements was used to estimate the vehicle position and velocity. In Chapter 4 a similar process was used to determine the relative vector between the two GPS antennas. As mentioned in Chapter 2, solving for a three dimensional position using GPS requires estimating the receiver clock error. The time derivative of the clock error must also be estimated if Doppler measurements are used to calculate receiver velocity. Since both the pseudorange in equation (3.1) and Doppler in equation (3.4) must be linearized, the state vector for the least squares procedure is a set of corrections ( $\hat{\mathbf{d}}$ ) to the point of linearization ( $\mathbf{x}_0$ ). The result is

$$\hat{\mathbf{d}} = \{ \mathbf{d}x \quad \mathbf{d}y \quad \mathbf{d}z \quad \mathbf{d}cdT \quad \mathbf{d}\dot{x} \quad \mathbf{d}\dot{y} \quad \mathbf{d}\dot{z} \quad \mathbf{d}cd\dot{T} \}^T \quad (6.1)$$

where,  $(\mathbf{d}x, \mathbf{d}y, \mathbf{d}z)$  is the correction to the approximate receiver position [m]

$(\mathbf{d}\dot{x}, \mathbf{d}\dot{y}, \mathbf{d}\dot{z})$  is the correction to the approximate receiver velocity [m/s]

$\mathbf{d}cdT$  is the correction to the receiver clock bias [m],

and  $\mathbf{d}cd\dot{T}$  is the correction to the receiver clock bias rate of change [m/s].

For the case of  $m$  GPS visible satellites, there will be  $m$  pseudorange measurements and  $m$  Doppler measurements. With eight parameters in equation (6.1) to estimate, there must be a minimum of four satellites, resulting in  $2*m = 8$  measurements. For the case of  $m > 4$ , a least squares adjustment must be used to estimate the eight parameters based on

minimizing the sum of the squared measurement error. Given an approximate vector ( $\mathbf{x}_o$ ), the misclosure vector ( $\mathbf{w}$ ) is given by (Krakiwsky, 1990)

$$\mathbf{w} = \mathbf{h}(\mathbf{x}_o) - \mathbf{z} \quad (6.2)$$

where,  $\mathbf{z}$  is the vector of GPS measurements and  $\mathbf{h}$  is given by equation (3.1) and (3.4) depending on the measurement. The estimated correction is given by equation (4.3), repeated here for convenience

$$\hat{\mathbf{d}} = -(\mathbf{H}^T \mathbf{R}^{-1} \mathbf{H})^{-1} \mathbf{H}^T \mathbf{R}^{-1} \mathbf{w} \quad (6.3)$$

where,  $\mathbf{H}$  is the design matrix and  $\mathbf{R}$  is the measurement variance matrix. The solution is calculated iteratively until  $\hat{\mathbf{d}}$  converges. The error covariance for the final estimate is given by

$$\mathbf{P} = \mathbf{H}^T \mathbf{R}^{-1} \mathbf{H}. \quad (6.4)$$

Since the measurement relations in equation (3.1) and (3.4) must be linearized,  $\mathbf{H}$  is calculated based on equation (2.18). The result can be represented as a hypermatrix given by

$$\mathbf{H} = \begin{bmatrix} \mathbf{H}_{11} & \vdots & \mathbf{0} \\ \dots & & \dots \\ \mathbf{H}_{21} & \vdots & \mathbf{H}_{22} \end{bmatrix} \quad (6.5)$$

where,  $\mathbf{H}_{11}$  is based on the pseudorange measurement equation while  $\mathbf{H}_{21}$  and  $\mathbf{H}_{22}$  are based on the Doppler measurement equation. The full derivation of the design matrix  $\mathbf{H}$  is given in the Appendix. The acceleration of the vehicle is calculated by fitting a relaxed

cubic spline to three consecutive velocity estimates and then taking the derivative. In order to do this a one second delay is introduced into the filter design. If less than four GPS satellites are visible, no position or velocity solution is computed. The filter continues to use the last available GPS position for computing the rotation matrix ( $\mathbf{T}$ ) defined in equation (3.15) to rotate the Earth-centered, Earth-fixed (ECEF) vector to the local level (LL) frame. Considering the radius of the Earth at 6,738 km, a 1 km error in the GPS position would still only result in a  $0.009^\circ$  misalignment error which is two orders of magnitude less than the expected accuracy of the system.

## 6.2.2 Kalman Filter Measurement and Dynamic Models

In order to implement a Kalman filter as described in Chapter 2, the nominal trajectory equations as well as the differential equations describing the dynamics must be defined. Continuous measurements at 10 Hz from the FOG and TCM2 compass are used to generate the nominal trajectory. The GPS measurements and TCM2 compass measurements are used in a 1 Hz extended Kalman filter (Gelb, 1974) to generate corrections every integer second to the nominal trajectory as well as predict selected sensor errors. The sensor errors included the effect of magnetic anomalies on the compass measurement as well as the drift of the FOG bias.

The nominal azimuth value ( $\psi_{nom}$ ) at time  $k$  is calculated as the azimuth at time  $k-1$  plus the angular displacement over one second, equal to ten consecutive integrated gyro measurements as defined in equation (5.11). The result is then

$$\mathbf{y}_{nom,k} = \mathbf{y}_{nom,k-1} + \sum_{i=1}^n \mathbf{w}_{y,i} \Delta t_i \quad (6.6)$$

where,  $\Delta t_i$  is the time interval for the  $i^{\text{th}}$  measurement and  $n$  is the number of gyro measurements over the integer second. The value of  $n$  was nominally ten, but the inability to synchronize the FOG measurements with GPS ( Chapter 5 ) meant that the value could sometimes be nine or eleven. The nominal pitch value ( $\theta_{\text{nom}}$ ) was taken as the current tilt meter pitch measurement after a possible GPS correction for acceleration given as

$$\mathbf{q}_{\text{nom},k} = \Delta \mathbf{q}_{\text{tcm},k} \cdot \quad (6.7)$$

The error in the nominal azimuth ( $\delta\psi$ ) is attributable to gyro measurement errors. This can be quantified as the integrated effect of an error ( $\delta d_{\text{fog}}$ ) in the rate bias ( $d_{\text{fog}}$ ) and a white noise sequence ( $w_\psi$ ) representing other unmodeled errors, given in differential form as

$$d\dot{\mathbf{y}} = D d d_{\text{fog}} + w_y \quad (6.8)$$

$$d d_{\text{fog}} = w_{\text{fog}} \quad (6.9)$$

where the rate bias error has been modeled as random walk (Gelb, 1974). The random walk assumption for gyro drift was used successfully by Zhang (1995) in the development of a low cost INS/GPS system which used low-end solid state gyros. As described in Chapter 5, the gyro plane may be misaligned with respect to the azimuth plane requiring a correction for roll and pitch. The factor  $D$  is introduced to account for the misalignment when determining the effect of the rate bias error on the azimuth error. It is calculated as the average of the multiplier used in equation (5.11) to determine the effect of the rate bias ( $d_{\text{fog}}$ ) on the azimuth over the last second, given as

$$D = \frac{\sum_{i=1}^n s_i (1 - \Delta \mathbf{q}_i^2 - \Delta \mathbf{f}_i^2)^{-1/2}}{n} \quad (6.10)$$

where  $n$  is the number of gyro measurements over the last second. Note that the modeling of the nominal azimuth error presented here is similar to a GPS/INS implementation where the attitude misalignment errors are a function of the angular rate errors (Schwarz and Wei, 1997).

The possible time-correlated acceleration error in the tilt meter pitch measurement, used to generate the nominal pitch, prompts the use of a Gauss-Markov error model (Gelb, 1974) given by

$$d\dot{\mathbf{q}} = -\alpha d\mathbf{q} + w_q \quad (6.11)$$

where,  $\delta\theta$  is the error in the nominal pitch,  $w_\theta$  is a white noise sequence,  $\alpha$  is the inverse of the time constant and the dot denotes time derivative. The magnetic field error ( $\epsilon_{\text{mag}}$ ) affecting the compass measurement ( $\psi_{\text{tcm}}$ ) is estimated based on the assumption that the compass measurement is the sum of the true azimuth ( $\psi_{\text{true}}$ ) and the magnetic field error given by

$$\mathbf{y}_{\text{tcm}} = \mathbf{y}_{\text{true}} + \mathbf{e}_{\text{mag}} \quad (6.12)$$

Based on the assumption that the magnetic error can be slowly-varying, and therefore correlated in time, it is also modeled as a Gauss-Markov process

$$\dot{\mathbf{e}}_{\text{mag}} = -\beta \mathbf{e}_{\text{mag}} + w_{\text{mag}} \quad (6.13)$$

where,  $\beta$  is the inverse of the time constant and  $w_{\text{mag}}$  is a white noise sequence. For the case when GPS measurements are available, the full mathematical model of the nominal trajectory error is given in Figure 6.7.

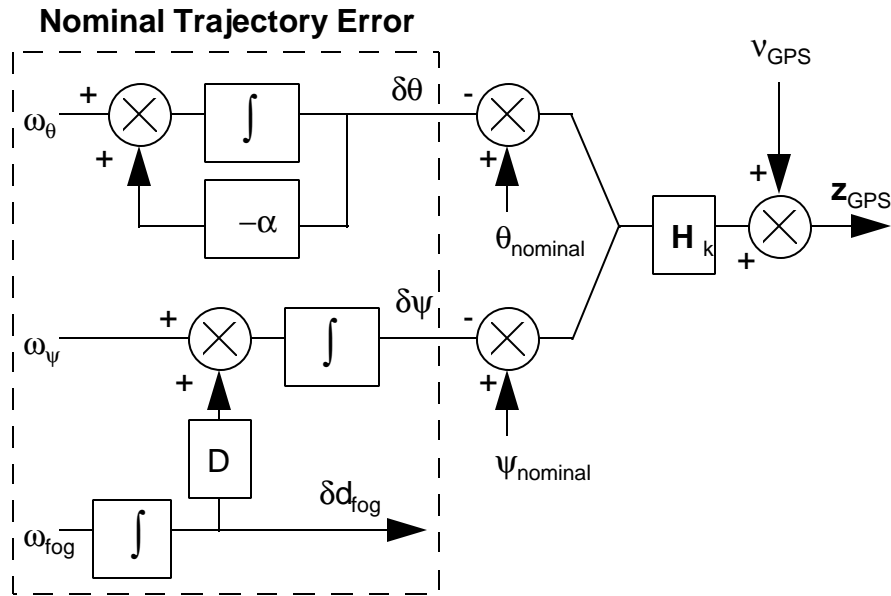


**Figure 6.7 - Mathematical model for nominal azimuth error ( $\delta y$ ) and pitch error ( $\delta q$ ) for the case of GPS measurements ( $z_{\text{GPS}}$ ).**

The mathematical model for the compass measurements does not include the nominal pitch but must include the magnetic field error as shown in Figure 6.8. The states for the filter are then taken as the output of the integrators in Figures 6.7 and 6.8 (Gelb, 1974). Eliminating redundant states, the result is

$$\hat{\mathbf{x}}_k = \{ \mathbf{d}y \quad \mathbf{d}q \quad \mathbf{d}d_{\text{fog}} \quad \mathbf{e}_{\text{mag}} \}^T. \quad (6.14)$$

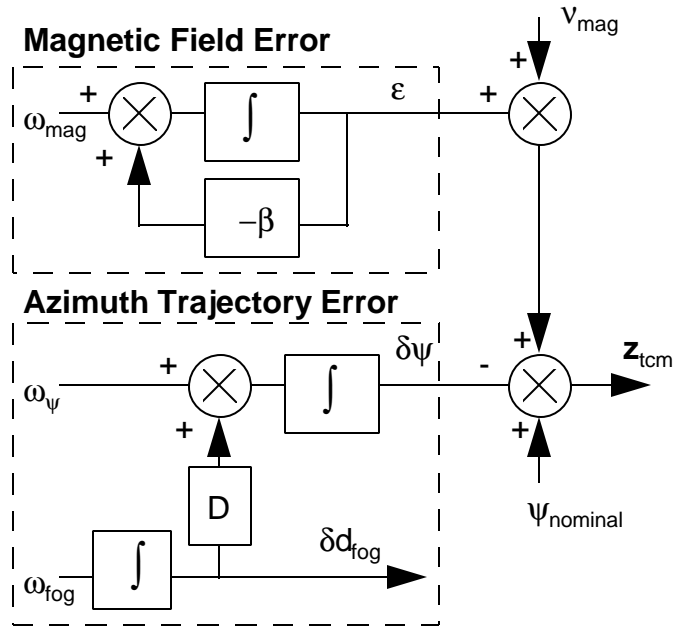


**Figure 6.8 - Mathematical model for nominal azimuth error ( $\delta y$ ) and magnetic field error ( $e_{mag}$ ) for the case of a compass measurement ( $z_{tcm}$ ).**

The corresponding set of differential equations in the form of equation (2.1) for the state vector in equation (6.14), and based on Figures 6.7 and 6.8, is then given by

$$\begin{bmatrix} \dot{d}y \\ \dot{d}q \\ \dot{d}d_{FOG} \\ \dot{e}_{mag} \end{bmatrix} = \begin{bmatrix} 0 & 0 & D & 0 \\ 0 & -a & 0 & 0 \\ 0 & 0 & 0 & 0 \\ 0 & 0 & 0 & -b \end{bmatrix} \begin{bmatrix} dy \\ dq \\ dd_{FOG} \\ e_{mag} \end{bmatrix} + \begin{bmatrix} w_y \\ w_q \\ w_{fog} \\ w_{mag} \end{bmatrix}. \quad (6.15)$$

The transition matrix necessary for the Kalman filter prediction stage, described in Chapter 2, is calculated using equation (2.4) resulting in

$$\Phi_k = \begin{bmatrix} 1 & 0 & D\Delta t & 0 \\ 0 & e^{-a\Delta t} & 0 & 0 \\ 0 & 0 & 1 & 0 \\ 0 & 0 & 0 & e^{-b\Delta t} \end{bmatrix}. \quad (6.16)$$

The process noise matrix ( $\mathbf{Q}_k$ ) can be calculated using equation (2.10) where  $\mathbf{G}(\tau)$  is an identity matrix and the spectral density matrix is diagonal and given by

$$\mathbf{Q}(t) = \text{diag}\{q_y \quad q_q \quad q_{fog} \quad q_{mag}\} \quad (6.17)$$

where,  $q$  represents the spectral density of the corresponding white noise sequence. The elements of the corresponding process noise matrix are given by

$$\mathbf{Q}_{k,11} = q_y \Delta t + q_{fog} D^2 \frac{\Delta t^3}{3} \quad (6.18)$$

$$\mathbf{Q}_{k,22} = \frac{q_q}{2a} (1 - e^{-2a\Delta t}) \quad (6.19)$$

$$\mathbf{Q}_{k,31} = \mathbf{Q}_{k,13} = q_{fog} D \frac{\Delta t^2}{2} \quad (6.20)$$

$$\mathbf{Q}_{k,33} = q_{fog} \Delta t \quad (6.21)$$

$$\mathbf{Q}_{k,44} = \frac{q_{mag}}{2b} (1 - e^{-2b\Delta t}) \quad (6.22)$$

where the numbers beside the time subscript  $k$  indicate row and column and all other elements are zero. Since the measurement relation for the interferometric GPS carrier phase measurement given in equation (3.17) is non-linear, the design matrix ( $\mathbf{H}_k$ ) must be calculated using equation (2.18). The result is given in equation (6.23) for the case of  $m$  GPS measurements where the vectors  $\mathbf{b}$  and  $\mathbf{e}$  as well as the matrix  $\mathbf{T}$  are defined in equations (3.12), (3.15) and (3.16).

$$\mathbf{H}_{k,GPS} = \begin{bmatrix} -(\mathbf{e}_1 - \mathbf{e}_b) \cdot \mathbf{T} \cdot \frac{\mathcal{I}\mathbf{b}}{\mathcal{I}\mathbf{y}} & 0 & -(\mathbf{e}_1 - \mathbf{e}_b) \cdot \mathbf{T} \cdot \frac{\mathcal{I}\mathbf{b}}{\mathcal{I}\mathbf{q}} & 0 \\ -(\mathbf{e}_2 - \mathbf{e}_b) \cdot \mathbf{T} \cdot \frac{\mathcal{I}\mathbf{b}}{\mathcal{I}\mathbf{y}} & 0 & -(\mathbf{e}_2 - \mathbf{e}_b) \cdot \mathbf{T} \cdot \frac{\mathcal{I}\mathbf{b}}{\mathcal{I}\mathbf{q}} & 0 \\ \vdots & \vdots & \vdots & \vdots \\ -(\mathbf{e}_m - \mathbf{e}_b) \cdot \mathbf{T} \cdot \frac{\mathcal{I}\mathbf{b}}{\mathcal{I}\mathbf{y}} & 0 & -(\mathbf{e}_m - \mathbf{e}_b) \cdot \mathbf{T} \cdot \frac{\mathcal{I}\mathbf{b}}{\mathcal{I}\mathbf{q}} & 0 \end{bmatrix}. \quad (6.23)$$

The design matrix for the case of a compass measurement is given based on equation (6.12) as

$$\mathbf{H}_{k,TCM2} = [1 \ 0 \ 0 \ 1]. \quad (6.24)$$

Actual values for the filter parameters, including the spectral densities and time constants are discussed in Chapter 7 after an examination of the individual sensors.

When less than four satellites were available, no GPS measurements were used in the filter. Theoretically, it should be possible to use GPS measurements for the case of two or three satellites corresponding to one or two double differences. This could happen if ambiguity resolution with a minimum of five satellites had taken place and subsequently two or three satellites were lost. Instead, the chosen approach was to use GPS, when available, to calibrate the compass and FOG sensor errors and thus improve bridging between GPS coverage gaps. The non-GPS sensors were used to coast through periods of GPS outage, reduce the GPS carrier phase ambiguity search space and increase the chance of detecting a wrong carrier phase ambiguity.

The research could then focus on developing and verifying the proper dynamic error models and determining the full range of filter performance under the two extreme conditions, namely with full GPS coverage and without. This approach is more

conservative than a filter trying to use reduced GPS coverage but the decrease in complexity results in a better overall estimate of possible filter performance since fewer variations are introduced. The reduced complexity of the filter design also resulted in an opportunity to examine the performance limits and error behaviour of the individual sensors to quantify the advantage of filtering. Chapter 7 starts with an in-depth analysis of the individual sensor errors and then examines the performance of the filter under varying durations of GPS outage as well as the ability to estimate sensor error sources.

## **CHAPTER 7**

### **TEST RESULTS**

The testing procedure had two goals, first to ensure the integrity of the logging software and second, to develop and evaluate the post-mission processing software. Three independent tests over different days were used to validate the system. The first two tests were conducted in large parking lots with an unobstructed view of the sky and no local magnetic anomalies present. The integrated system was tested against an independent GPS-only post-mission processing software package called HEAD<sup>TM</sup> which was developed at The University of Calgary (Sun and Cannon, 1995). GPS sensor outages in the integrated system were simulated in post-mission. The purpose of these first two, near-ideal, tests was to determine sensor limitations, eliminate data collection problems and develop sensor models.

Results from the first two days showed the need for a more accurate and reliable reference trajectory against which to evaluate the integrated system (Harvey and Cannon, 1997). An additional requirement for the new reference trajectory generator was the ability to maintain an accurate solution in operational as opposed to near-ideal conditions. GPS-only systems were precluded since sky visibility and hence solution availability would be limited. Therefore, a more extensive test under operational conditions was planned and executed with a highly accurate GPS/INS system mounted in the test vehicle along with the integrated sensor system under examination. In this chapter, a full description of this operational test is given, along with an examination of the raw sensor behaviour, followed by a performance evaluation of the integrated filter.

#### **7.1 Test Description**

The operational test was conducted in a suburban area of Calgary, Alberta in October, 1997. The test route was under medium foliage conditions and in several spots lined with

parked cars which were expected to adversely affect the TCM2 magnetic compass measurement. The GPS/INS reference system consisted of two Ashtech Z-12 GPS receivers and a Litton LTN90-100 inertial navigation system. The LTN90-100 and one Ashtech receiver were placed in the vehicle while the other Ashtech was used as a stationary reference for differential corrections. Raw measurements were processed using KINGSPAD™, a post-mission GPS/INS processing software package developed at The University of Calgary (Skaloud, 1995). The KINGSPAD™ output included the vehicle position, velocity, acceleration and attitude at 64 Hz. A low-pass filter was used to reduce the data files from 64 Hz to 16 Hz to decrease the file sizes. An examination of the orientation accuracy of the GPS/INS system was carried out by Skaloud (1995) and was shown to be well below one arc-minute, which is an order of magnitude better than early results obtained with the current system (Harvey and Cannon, 1997). The trajectory of the test track is shown in Figure 7.1 and was repeated a number of times over a period of about forty minutes.

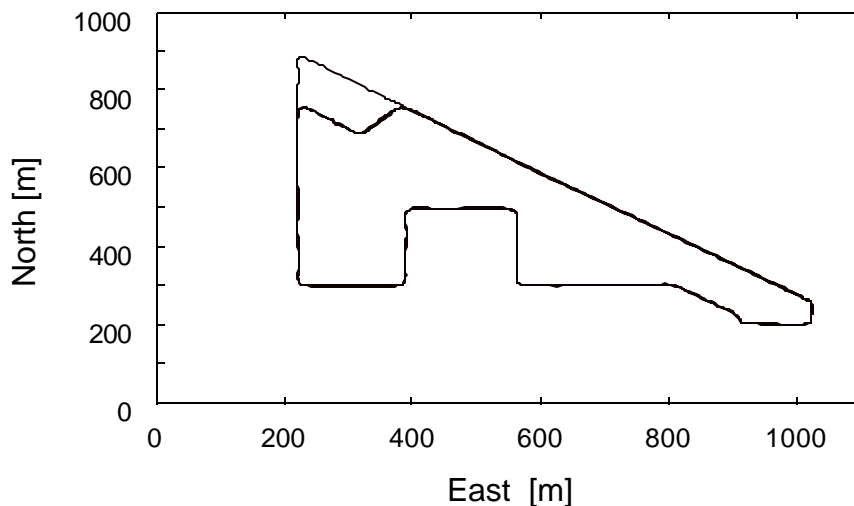


**Figure 7.1 - Trajectory of suburban test in NW Calgary, Alberta, Canada in October 1997. Test duration about 40 minutes.**

Results from the GPS/INS were used as the reference during data analysis. The azimuth truth values are shown in Figure 7.2, where the repeated test track is clearly visible. The pitch and roll truth values are shown in Figure 7.3. For the period between GPS time 341000 s and 341350 s the vehicle was stationary.

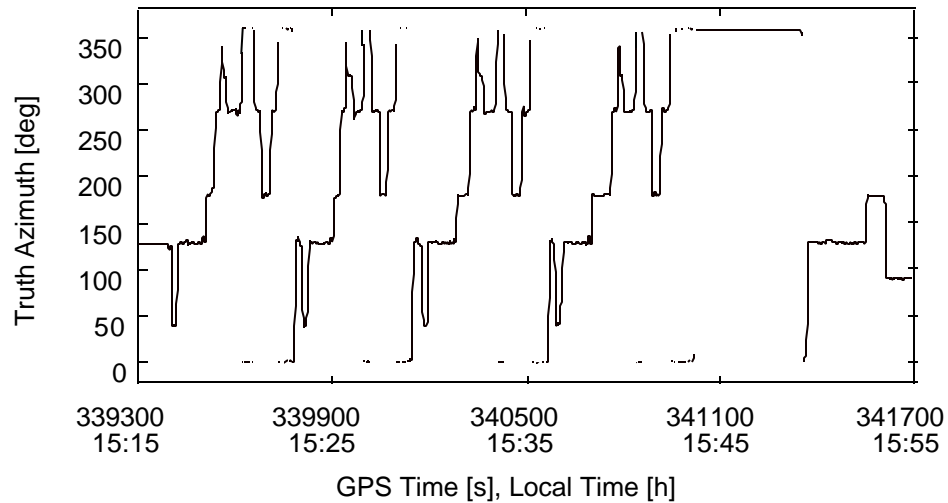


**Figure 7.2 - Truth values for vehicle azimuth from GPS/INS reference.**

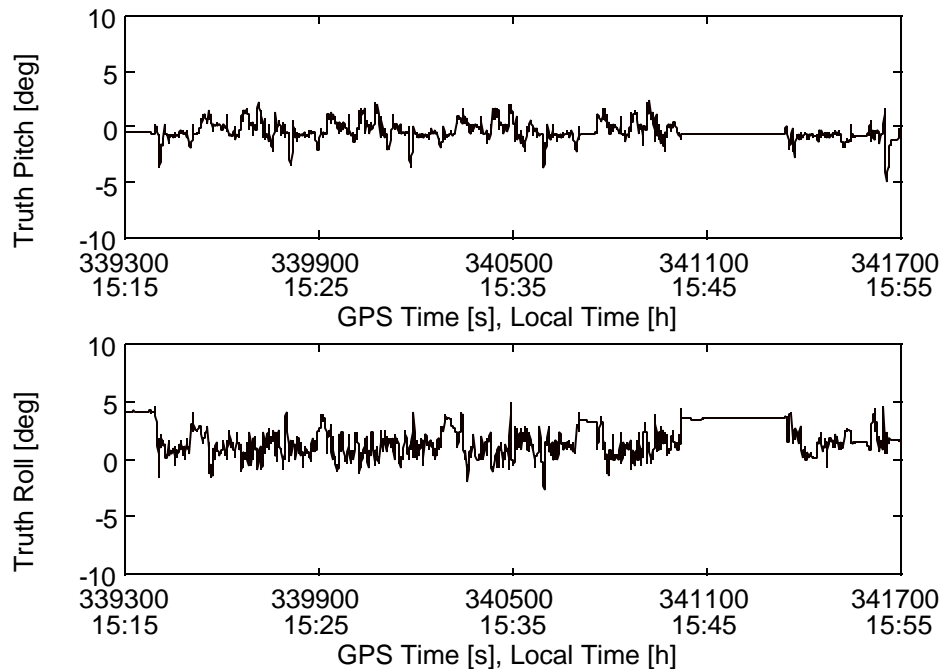


**Figure 7.3 - Truth values for vehicle roll and pitch from GPS/INS reference.**

Misalignment angles between the reference, TCM2 roll and pitch axes and GPS baseline were determined during a 30 minute static period prior to the commencement of the test and after the INS initial alignment. The number of visible GPS satellites above a 15° mask angle during the test period is given in Figure 7.4.

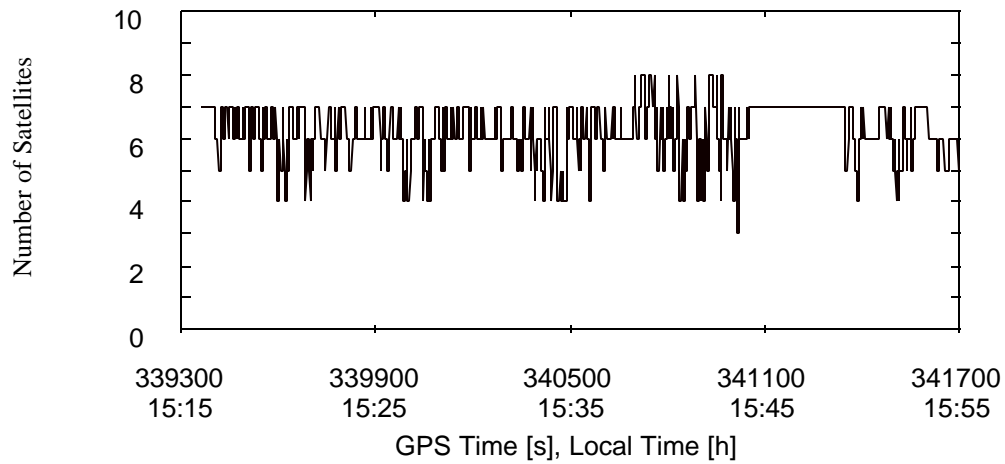


**Figure 7.4 - Number of visible satellites above 15° elevation mask angle for suburban test run.**

## 7.2 Individual Sensor Performance

Beyond determining the performance limits of the integrated filter, it was important to establish the benefit of the integrated approach versus using the individual sensors. Comparison of the raw sensor output to the reference was used to establish the accuracy of the sensors before filtering and to quantify error behaviour. Increased knowledge of the filter input was helpful for selecting filter parameters. In the next section, output from the four different sensors, GPS, FOG, tilt meter and compass is compared to the reference.

### 7.2.1 GPS-Only Results Using HEAD™

The GPS data collected during the test was run through an independent epoch-by-epoch GPS-only software package called HEAD™ which was developed at The University of Calgary (Sun and Cannon, 1995). In HEAD™, precise GPS carrier phase measurements with fixed ambiguities are used to establish the inter-antenna baseline vector in the ECEF frame which is then rotated to the local level to provide azimuth and pitch. The least squares ambiguity resolution procedure used in HEAD™ is based on Hatch (1990) as described in Chapter 4 and was the basis for the procedure used in the current software package. The azimuth and pitch errors for HEAD™ over the course of the test run are shown in Figure 7.5. The test statistics for the HEAD™ errors are shown in Table 7.1.

**Table 7.1 - GPS-Only error statistics for HEAD™.**

	Azimuth Error		Pitch Error	
	Outliers Removed	With Outliers	Outliers Removed	With Outliers
Mean	0.139 °	-0.734 °	0.021 °	-0.350 °
Std. Dev.	0.582 °	31.934 °	1.361 °	3.153 °
RMS	0.599 °	31.934 °	1.361 °	3.172 °

The outliers in the errors are caused by resolving to incorrect ambiguities and can be seen to exceed 100° in azimuth and 40° in pitch. In addition, HEAD™ was only able to provide an orientation solution for 83% of the test period due to line-of-sight obstruction or the inability to resolve ambiguities. With the outliers removed from the solution the availability dropped to 77%.

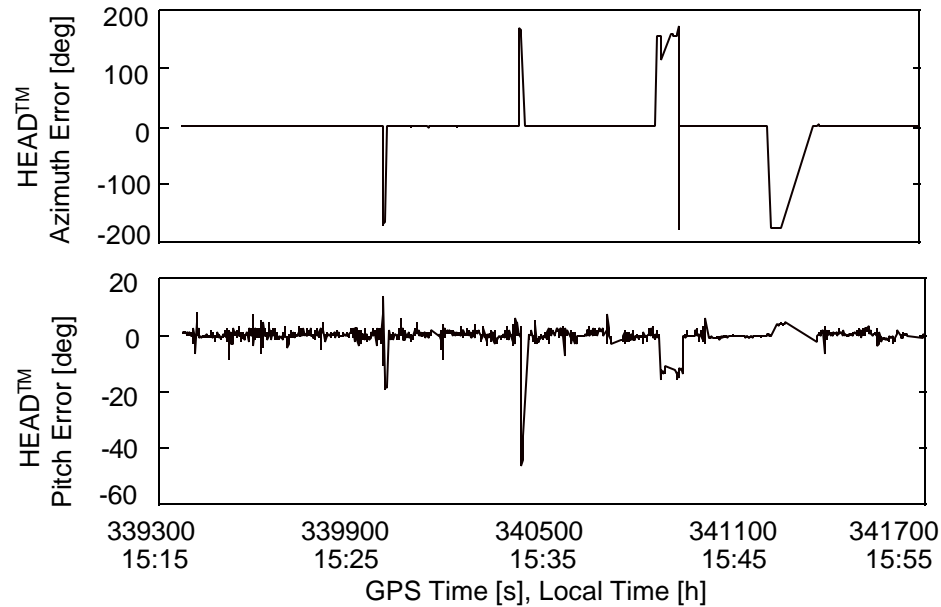


**Figure 7.5 - GPS-Only azimuth and pitch errors for HEAD™.**

### 7.2.2 Andrew Autogyro™ Results

Starting with the initial azimuth, the vehicle azimuth at a later time was estimated by integrating the output of the Autogyro™ given by equation (6.6). The first graph in Figure 7.6 shows the resultant error in the Autogyro™ estimate based on the temperature dependent scale factor estimated by Hayashi (1996). Two different types of errors are evident, a long term drift and abrupt jumps that correspond to the vehicle changing direction. The long term drift resulted from integrating a slowly varying measurement bias while the abrupt jumps were due to a scale factor error. As explained in Chapter 5, research indicated that the Hayashi (1996) scale factor polynomial was based on experimental data collected above the operating temperature for this test. A new polynomial was developed based on matching the Autogyro™ output during known vehicle turns at various temperatures with the reference. The result is shown as the second graph in Figure 7.6 where the abrupt jumps are much less evident. The drift in

the lower graph of Figure 7.6 is seen to be about  $45^\circ$  in 2400 s or  $0.019^\circ/\text{s}$  which is at the level of the minimum detectable rotation rate for the Autogyro™ given in Table 5.1.

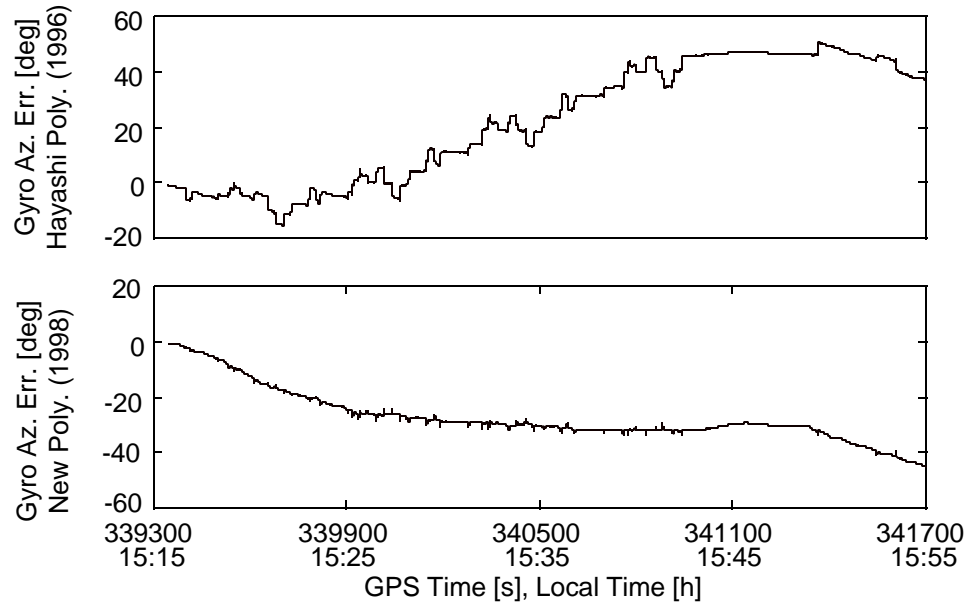


**Figure 7.6 - Integrated raw Autogyro™ output using Hayashi (1996) scale factor polynomial versus current polynomial with temperature range  $15^\circ$  to  $20^\circ$  C.**

The advantage of developing another scale factor polynomial is not immediately evident from Figure 7.6 since this actually results in a greater error after the 2400 s period. In order to understand the benefit of removing the abrupt jumps it must be remembered that the filter developed in Chapter 6 is designed to estimate the measurement bias based on the assumption that it varies slowly with time and is also the dominant Autogyro™ error source. If the Hayashi (1996) polynomial was used, this assumption would be invalid and the filter would try to estimate the measurement bias error based on an incorrect

model. This situation highlights the advantage of examining the filter input in detail to reduce complications during filtering.

### 7.2.3 Precision Navigation Inc. TCM2-50 Results

The TCM2 azimuth output, being derived from magnetic field measurements, was expected to suffer from magnetic anomalies as described in Chapter 5. The TCM2 was equipped with a magnetic anomaly detector (MAD), designed to indicate when solution integrity might be compromised, but early testing left some doubt as to its level of effectiveness. With precise reference data available, a more thorough examination was possible. The upper graph in Figure 7.7 shows the TCM2 compass error when the MAD was ignored. The error is seen to be continuous and bounded over the entire test period. The lower graph represents the same error stream except with measurements removed whenever the MAD was triggered. Effectively, the MAD reduced the availability of the compass measurements from 100% to 39% over the test period with no corresponding gain in accuracy. The effect of the MAD was therefore ignored, under the assumption that the error was bounded regardless of magnetic anomaly effects and could be described by a conservative measurement variance. The TCM2 tilt meter roll and pitch error is shown in Figure 7.8. The statistics for Figures 7.7 and 7.8 are given in Table 7.2.

**Table 7.2 - Precision Navigation TCM2-50 error statistics.**

	Azimuth Error		Pitch Error	Roll Error
	MAD disabled	MAD enabled		
Mean	-1.223 °	-1.272 °	0.252 °	0.331 °
Std. Dev.	5.847 °	6.235 °	3.206 °	3.251 °
RMS	5.974 °	6.363 °	3.216 °	3.268 °

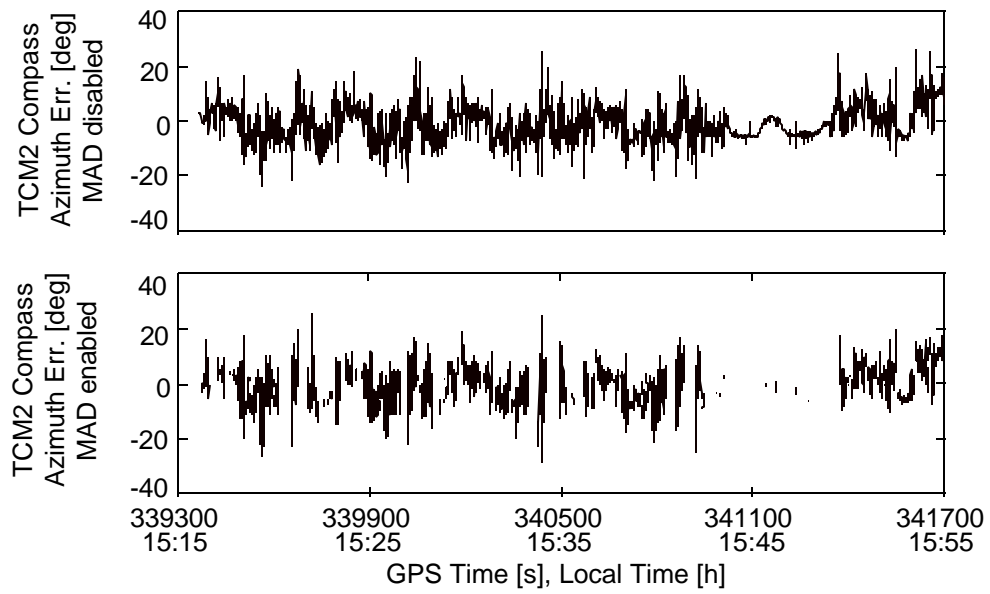


**Figure 7.7 - Comparison of TCM2 compass error with magnetic anomaly detector (MAD) enabled and disabled.**

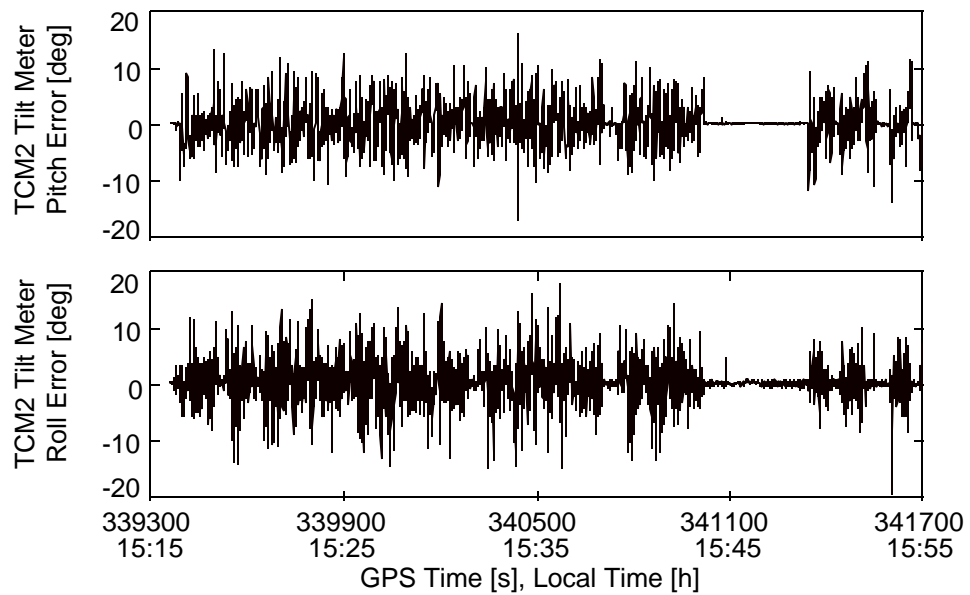


**Figure 7.8 - Roll and pitch error for TCM2 tilt meter.**

The difference in Table 7.2 between the compass error standard deviation with MAD enabled and MAD disabled is due to the exclusion of the static data (GPS time 341000 s to 341350 s) seen in the lower graph of Figure 7.7. The large value in Table 7.2 for the mean of the azimuth error is due to the difficulty in determining the true azimuth of the vehicle with respect to the compass heading in the presence of so much noise, and the possibility that the probability distribution of the error is not Gaussian. A physical explanation for this could be the presence of magnetic anomalies due to parked cars always being closer to the right hand side of the vehicle as opposed to the left hand side. The magnetic field effect of the closer cars would be constantly larger in magnitude and introduce a bias in the error. The time-correlation of the TCM2 compass error was examined through use of the autocorrelation function, given as the inverse Fourier transform of the power spectral density, and is shown in Figure 7.9.

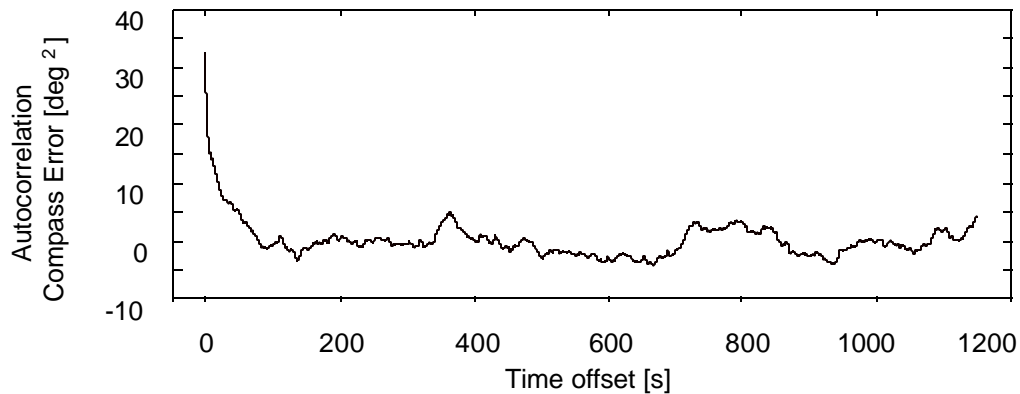


**Figure 7.9 - Autocorrelation of TCM2 compass error.**

It can be seen that there is significant correlation in the compass error, assumed to be due to magnetic interference. Care must be taken when using the autocorrelation function in this fashion as the power spectral density is based on a single set of experimental data. It is, however, useful to gain insight into possible errors and the behaviour of sensor data before filtering takes place. Since the effect of magnetic anomalies during operation was unpredictable, the true correlation time varied in a manner which was not deterministic.

When the autocorrelation function is evaluated for a zero-time offset, the result is the variance of the error. Examination of Figure 7.9 reveals a variance of  $34^\circ$  squared corresponding to a standard deviation of  $5.8^\circ$  which agrees with the results in Table 7.2.

Evident from Figure 7.8 is the difference in tilt meter error behaviour between when the vehicle was static ( 341000 s to 341350 s ) and when the vehicle was in motion. As described in Chapter 5, the larger error associated with vehicle motion was due to movement of the reference liquid surface inside the tilt meter. The next section will examine the correlation between vehicle acceleration and tilt meter error as well as examine the effect of the correction proposed in Chapter 5.

### **7.3 Effect of GPS Acceleration Corrections on Tilt Meter Output**

In Chapter 5, an acceleration based correction for the tilt meter was derived and given in equation (5.14). The roll error was assumed to be correlated with the cross-track acceleration and the pitch error correlated with the along-track acceleration. A three-minute section of data was selected that was known to contain vehicle motion to test the effect of the correction. The length of the data set was based on the assumption that the various motion-based accelerations affecting the vehicle would have a much shorter correlation time than three minutes.

Figure 7.10 shows the raw pitch error versus the along-track acceleration correction generated from equation (5.14) for the GPS-only case and the reference GPS/INS case. Figure 7.11 shows the same information for the roll error versus the cross-track acceleration correction.

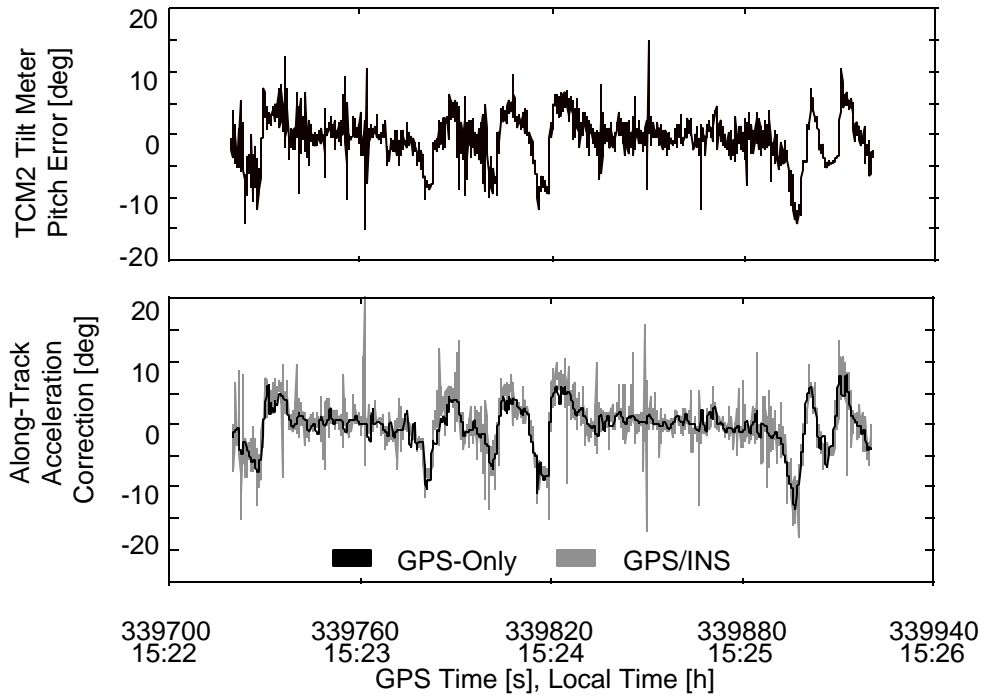


**Figure 7.10 - Raw TCM2 pitch error and acceleration based correction using GPS-only and the GPS/INS reference.**

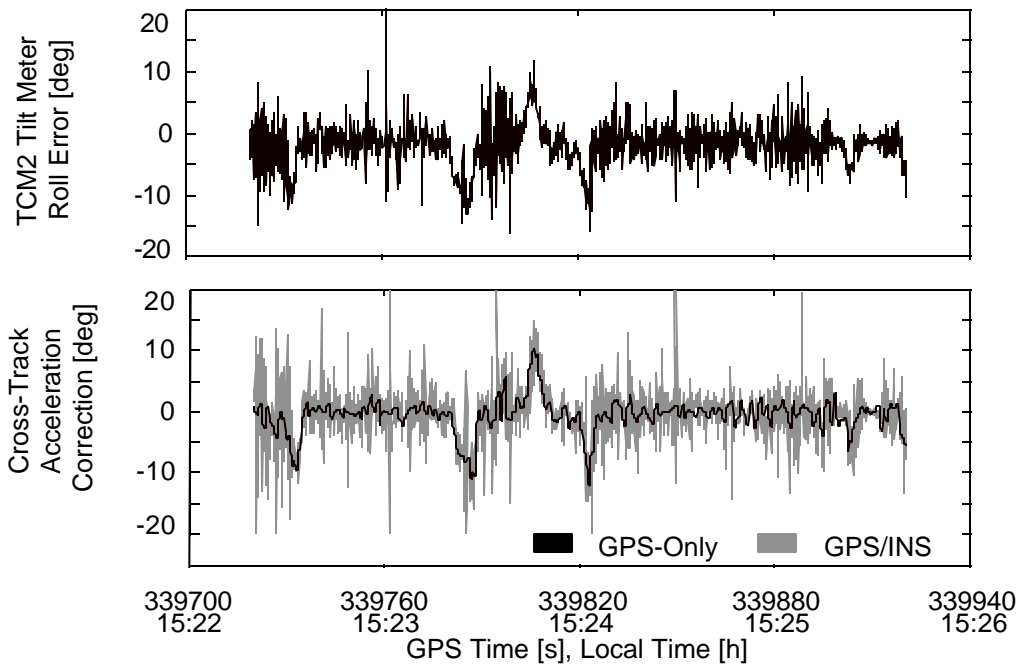


**Figure 7.11 - Raw TCM2 roll error and acceleration based correction using GPS-only and the GPS/INS reference.**

The GPS-only acceleration correction, described in Chapter 6, can be seen to emulate the low-frequency component of the vehicle acceleration but cannot capture the high frequency component obtainable with the INS. This is to be expected since the 16 Hz INS data rate is bandlimited to 8 Hz while the 1 Hz GPS measurements are limited to 0.5 Hz based on the Nyquist sampling theorem. It is also clearly evident that the long-term error in the TCM2 roll and pitch measurements is correlated with the low-frequency trends of the acceleration correction based on equation (5.14). Figure 7.12 shows the TCM2 roll and pitch measurement error after the GPS acceleration correction has been applied.

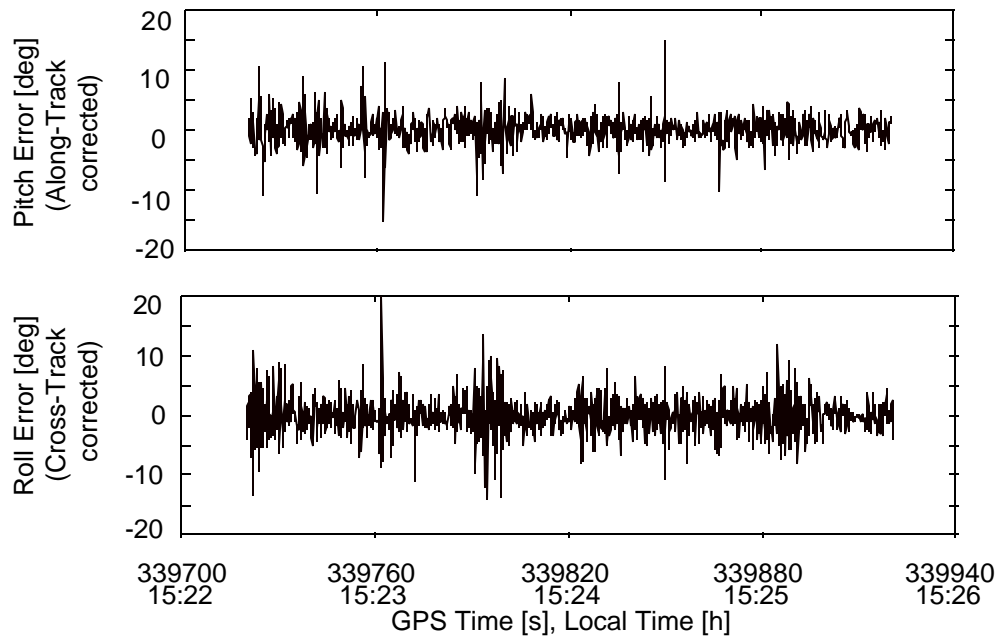


**Figure 7.12 - TCM2 roll and pitch error after GPS acceleration correction.**

The low-frequency component of the pitch and roll error in Figures 7.10 and 7.11 are no longer present in Figure 7.12. The error statistics for this test period are shown in Table 7.3 for the raw pitch and roll error and the acceleration corrected error. It can be seen

that removing the low-frequency component of the error also reduces the standard deviation of the total error by about  $1.6^\circ$  in pitch and  $0.8^\circ$  in roll.

**Table 7.3 - TCM2 pitch and roll error statistics for 180 s test period, before and after applying a GPS derived correction for acceleration.**

	Pitch Error		Roll Error	
	Raw	Acceleration Corr.	Raw	Acceleration Corr.
Mean	$0.374^\circ$	$-0.093^\circ$	$0.475^\circ$	$0.097^\circ$
Std. Dev.	$3.842^\circ$	$2.195^\circ$	$3.720^\circ$	$2.910^\circ$
RMS	$3.859^\circ$	$2.196^\circ$	$3.845^\circ$	$2.909^\circ$

Removal of the low-frequency component improves the whiteness of the resulting error as shown in Figure 7.12, and more closely approximates a zero-mean sequence as detailed in Table 7.3 because the high-frequency components have a shorter averaging time. The ability of the correction to eliminate acceleration dependent time-correlated error can be further examined through use of the autocorrelation function shown in Figure 7.13. The corrected data sequence drops to the noise level within about 0.3 s in both cases while the uncorrected case demonstrates high correlation for periods up to 5 s. As mentioned previously, the autocorrelation sequence as presented here is the inverse Fourier transform of the experimentally derived power spectral density. It is useful for demonstrating the magnitude of the correction but the results are data set specific.

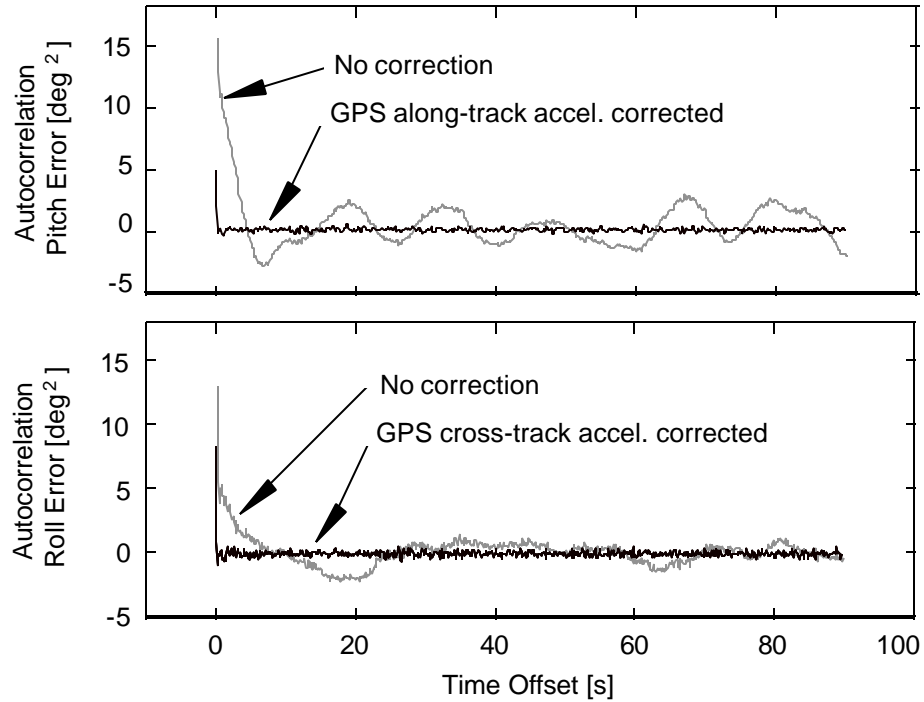


**Figure 7.13 - Effectiveness of GPS acceleration based correction at removing low-frequency error in TCM2 tilt meter measurements.**

The improvement over the entire test period after applying the acceleration correction is summarized in Table 7.4 where the original values have been repeated from Table 7.2 for convenience.

**Table 7.4 - TCM2 pitch and roll error statistics for full test period, before and after applying a GPS derived correction for acceleration.**

	Pitch Error		Roll Error	
	Raw	Acceleration Corr.	Raw	Acceleration Corr.
Mean	0.252 °	-0.080 °	0.475 °	0.141 °
Std. Dev.	3.206 °	1.873 °	3.251 °	2.589 °
RMS	3.216 °	1.873 °	3.268 °	2.585 °

## 7.4 Integrated Filter Results

The most difficult task in the implementation of a Kalman filter is in the selection of the filter parameters. In general, this is an empirical process known as tuning wherein the various parameters are chosen to optimally estimate the state of the system while accurately reflecting the true state error in the covariance and avoiding divergence. Specifically, it was necessary to define the measurement variance matrix  $\mathbf{R}_k$ , the transition matrix  $\Phi_k$  and process noise matrix  $\mathbf{Q}_k$ . For the GPS system it was necessary to define the size of the ambiguity search space and set a  $15^\circ$  elevation mask angle. To implement the innovation testing scheme described in Chapter 2, the significance level ( $\beta$ ) was set to 20% while the confidence level ( $1-\alpha$ ) was set to 99%.

A consequence of mounting the system on a vehicle was that the operational conditions, including dynamics and GPS satellite availability, could vary widely. The result was that a set of filter parameters chosen to optimize the filter performance for a given set of operational conditions would be suboptimal and perhaps even divergent as the conditions changed over time. To optimize the filter performance over all conditions an adaptive scheme was used, wherein the spectral densities of the states were set dependent on vehicle dynamics and available sensor information. The final values for the spectral densities are shown in Table 7.5. If only compass measurements were available, the spectral densities for the magnetic field error and gyro rate bias error were set very low. Effectively, these states remained fixed while the filter estimated the azimuth error based on the noisy compass measurement. With no measurements available to estimate a pitch error, the pitch process noise was set to reflect the accuracy of the nominal pitch generated using the tilt meter with no GPS acceleration correction.

**Table 7.5 - Adaptive scheme for integrated filter spectral densities.**

Spectral Density	Compass Only	Compass and GPS		
		Ambiguities first resolved	Ambiguities resolved for > 10s	Ambiguities resolved > 10s and $\omega^{\text{true}} < 0.2^\circ/\text{s}$
$q_\psi$	$(0.5^\circ)^2 / \text{s}$	$(0.3^\circ)^2 / \text{s}$	$(0.3^\circ)^2 / \text{s}$	$(0.06^\circ)^2 / \text{s}$
$q_\theta$	$(2.5^\circ)^2 / \text{s}$	$(1.2^\circ)^2 / \text{s}$	$(1.2^\circ)^2 / \text{s}$	$(1.2^\circ)^2 / \text{s}$
$q_{\text{fog}}$	$(1 \times 10^{-4} \text{ bits/s})^2 / \text{s}$	$(0.05 \text{ bits/s})^2 / \text{s}$	$(0.05 \text{ bits/s})^2 / \text{s}$	$(1.0 \text{ bits/s})^2 / \text{s}$
$q_{\text{mag}}$	$(0.006^\circ)^2 / \text{s}$	$(6.0^\circ)^2 / \text{s}$	$(12.0^\circ)^2 / \text{s}$	$(12.0^\circ)^2 / \text{s}$

With GPS available, it was possible to estimate the gyro rate and magnetic field errors. The potential hazard when using GPS, was allowing the filter to estimate the sensor errors immediately after the carrier phase integer ambiguities had been fixed. If the ambiguities were incorrectly selected and not immediately detected through the innovation sequence, the estimated error results would be compromised and a filter restart would be necessary. A worst-case scenario in this situation would be losing GPS immediately after corrupting the error states with wrong ambiguities. The improperly estimated rate bias error would be integrated over time, resulting in rapid error growth in the azimuth nominal trajectory. The magnetic field error would decay to zero following the exponential decay behaviour of the Gauss-Markov process but the compass measurements would be too noisy to reset the gyro rate error.

Examination of the filter behaviour during the test revealed that incorrect ambiguities were detected by the filter either immediately or within 5 s of resolution. To avoid corrupting the sensor error estimates during this period, a gradual scheme was implemented where for the first 10 s after GPS ambiguities were resolved, the process noise value for the gyro rate error was kept very low. After 10 s, the process noise values

were increased to allow the filter to estimate all the parameters. An additional concern was estimating the gyro rate bias error during turns where it is difficult to distinguish scale factor error from bias error, as mentioned in section 7.2.2. To avoid this, the gyro rate bias error spectral density was only increased if the azimuth rate of change, as indicated in equation (5.11), was less than  $0.2^\circ/\text{s}$ . This number was chosen based on noise present in the raw gyro measurement when the vehicle was known to be stationary or traveling in a straight line. The correlation time for the nominal pitch error was set to 0.25 s based on Figure 7.13, effectively assuming no correlation between filtering epochs when the GPS acceleration correction was available. Figure 7.8 showed significant time correlation in the magnetic field error that could not be removed. The magnetic field error correlation time was conservatively set to 10 s to account for a portion of the error, recognizing that the true correlation time was not deterministic.

The measurement variance matrix  $\mathbf{R}_k$ , was square diagonal with rank equal to the number of observations. GPS carrier phase measurement variance was set to  $(1.5 \text{ cm})^2$  based on Table 3.2 and the need to tune the innovation sequence test, discussed later. The variance for the compass measurement was set to  $(8.5^\circ)^2$  when only compass measurements were available and  $(5.5^\circ)^2$  when GPS was available. In the former case, the measurement variance had to account for the magnetic field error, while in the latter case the magnetic field error was estimated as a separate state. It should be mentioned that when both GPS and compass measurements were available, the high level of noise on the compass ensured that the filter estimate was dominated by GPS. Roughly speaking, the magnetic field error was estimated at this point based on the difference between the GPS and compass measurements.

As a final step before implementing the filter, the parameters for GPS carrier phase ambiguity resolution had to be chosen. As discussed in Chapter 4, the ambiguity search

space was centered on the approximate remote antenna location, based on the TCM2 compass azimuth, tilt meter pitch and *a priori* baseline length of 0.919 m. The size of the search space was conservatively chosen based on the accuracy of the compass and pitch measurements. Following equations (4.10) to (4.12), the azimuth uncertainty ( $\sigma_\psi$ ) was set to  $10^\circ$ , the pitch uncertainty ( $\sigma_\theta$ ) to  $5^\circ$  and the baseline uncertainty ( $\sigma_b$ ) to 5 cm.

### 7.4.1 Suburban GPS Coverage

The integrated filter output included estimates of the system states along with estimated accuracies in the form of a covariance matrix. The azimuth and pitch error for the integrated filter along with the estimated filter error in the form of a  $3\sigma$  envelope are shown in Figure 7.14. The abrupt changes in the error envelopes are due to orientation changes or loss of GPS coverage.

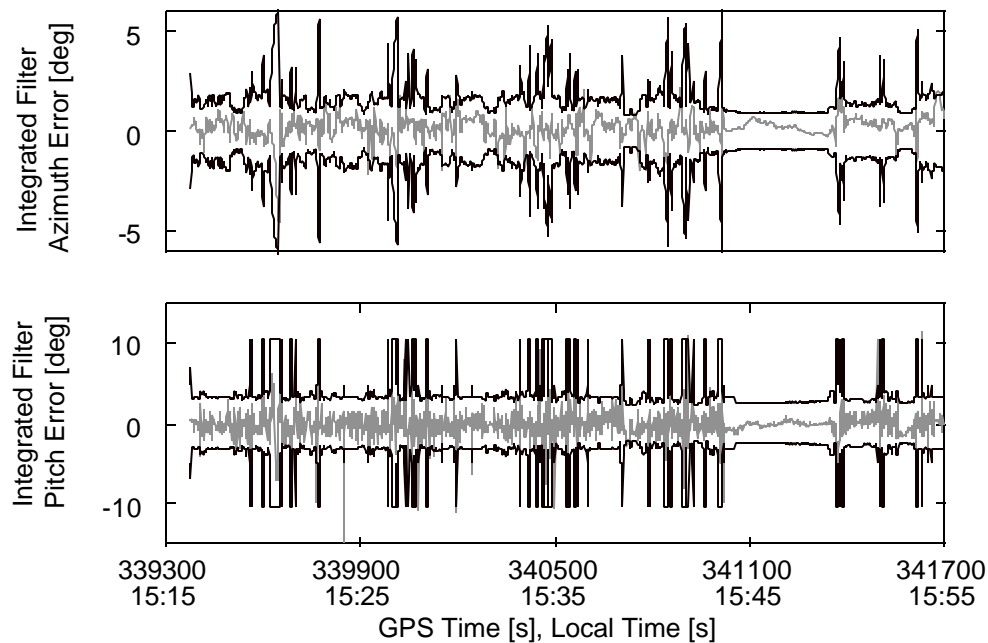


**Figure 7.14 - Integrated filter azimuth and pitch error results, including  $3\sigma$  error envelope for suburban run.**

In both graphs, it is evident that the estimated filter error accurately reflects the true error of the system. The integrated filter azimuth and pitch error results are summarized in Table 7.6.

**Table 7.6 - Integrated filter azimuth and pitch error statistics for suburban run.**

	Azimuth Error	Pitch Error
Mean	0.140 °	-0.177 °
Std.Dev.	0.641 °	1.496 °
RMS	0.656 °	1.506 °

In the following analysis, azimuth and pitch error refers to the filter value minus the reference while sensor error refers to the filter estimate of an error. The integrated filter results were seen to be much better than the TCM2 compass, slightly better than the TCM2 tilt meter and slightly worse than GPS-only results using HEAD™ with the outliers removed. However, with outliers included in the GPS-only statistics, the integrated filter was better than any independent sensor. The integrated filter also demonstrated much higher availability than GPS alone, providing a continuous solution for 100% of the test period where the GPS-only system provided 83% with outliers included and 77% with outliers removed.

The top graph in Figure 7.15 shows the integrated filter estimate of the gyro rate bias error along with the  $3\sigma$  error envelope. The bottom graph in Figure 7.15 shows the raw integrated output of the gyro repeated from Figure 7.6 versus the same output corrected using the filter estimated bias. Figure 7.16 shows the integrated filter estimated magnetic field error with associated  $3\sigma$  error envelope (top graph) as well as the estimated error versus the true compass error (bottom graph).

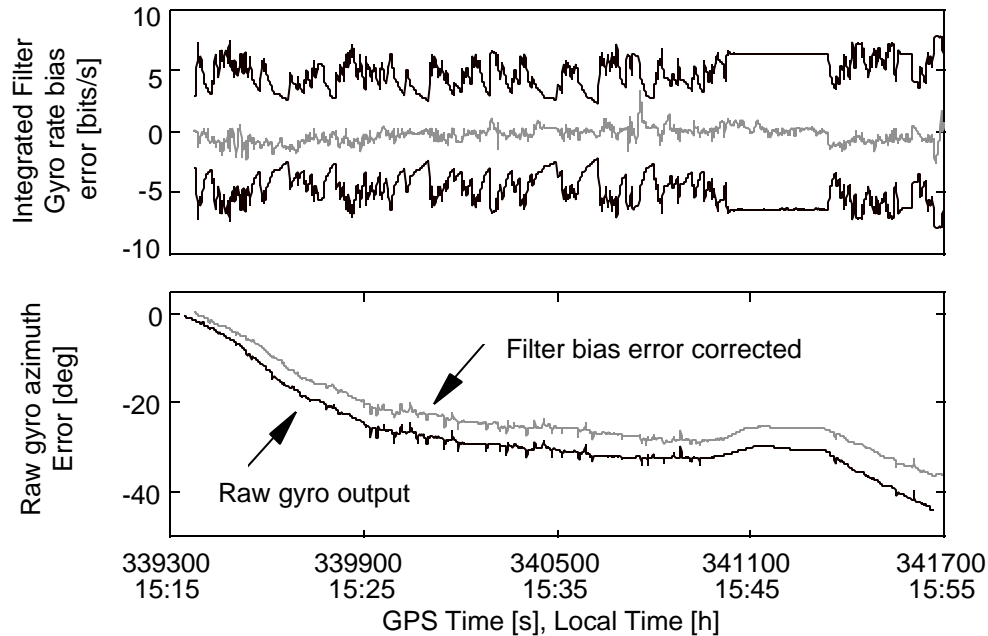


**Figure 7.15 - Integrated filter estimated gyro rate bias error, including 3s error envelope (top) and result of applying estimated bias to raw gyro output (bottom).**

Examination of the filter results reveals that the estimated rate bias error is on the same order as the resolution level of the gyro. The drift seen in Figure 7.6 is due in large part to the limited resolution of the gyro and the resulting oscillation between two consecutive quantized values. The challenge for the filter was then to estimate the overall long-term effect of an oscillation between quantized levels of the gyro as opposed to a true bias. Despite this, application of the filter estimated bias to the raw gyro output still resulted in a substantial  $10^\circ$  error reduction over the 2400 s test period as shown in the bottom graph of Figure 7.15. Also evident in the top graph of Figure 7.15 is the filter reaction to the static period between GPS time 341000 and 341350 where the variance of the bias error state was maintained high allowing the filter to estimate the bias error under full GPS visibility. This was a result of the adaptive scheme given in Table 7.5 whereby the spectral density of the gyro rate bias error was increased.

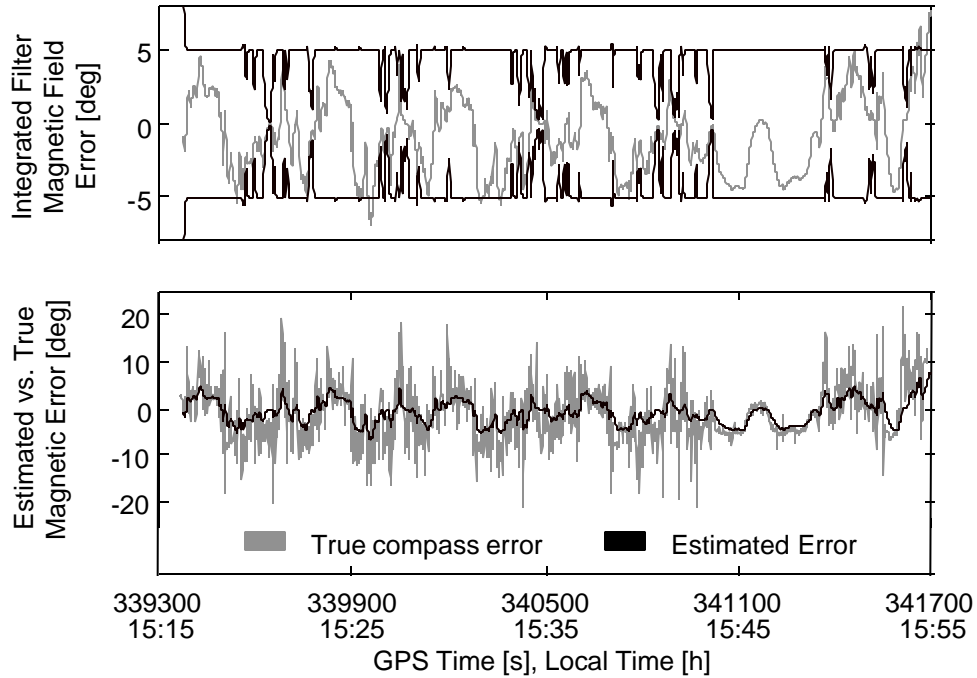


**Figure 7.16 - Integrated filter estimated magnetic field error, including 3 $\sigma$  error envelope (top) and comparison of estimated error vs. true compass error (bottom).**

The effectiveness of the integrated filter at estimating the magnetic field error is shown in the bottom graph of Figure 7.16. It is evident that the estimated error reflects the low frequency trends of the true compass error, repeated from Figure 7.7. The shape of the 3 $\sigma$  error envelope in Figure 7.16 was a result of the adaptive spectral density scheme defined in Table 7.5. With full GPS coverage, the spectral density of the magnetic field error was increased, opening up the covariance and allowing the filter to estimate the state. The dips in the error envelope represent periods where GPS coverage was compromised.

Innovation sequence testing was also implemented during the suburban run to monitor the performance of the integrated filter, primarily for the purpose of detecting wrong GPS carrier phase ambiguity sets. The results for the test statistic  $\mathbf{T}_k$  given by equation (2.28) are shown in Figure 7.17.

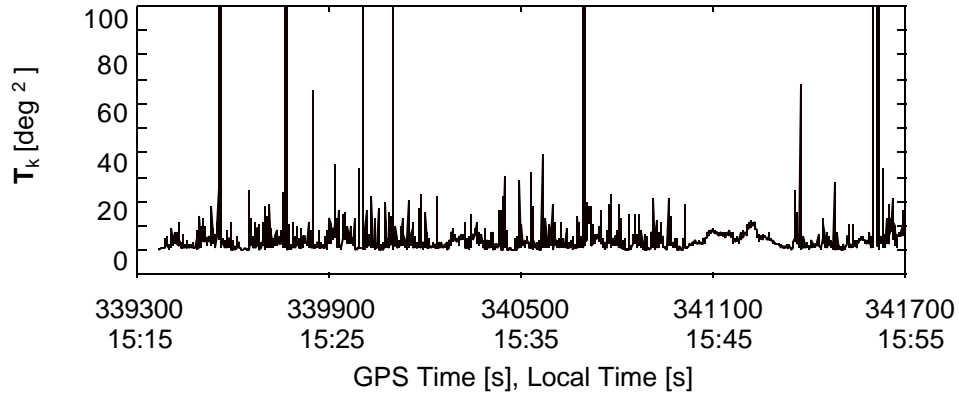


**Figure 7.17 - Innovation test statistic  $T_k$  for integrated filter during suburban run.**

Since the test statistic involves normalizing the innovation sequence by its covariance, it is possible to modulate the sensitivity of the test by adjusting the measurement variance matrix  $\mathbf{R}_k$  in equation (2.26). The GPS carrier phase measurement variance defined in the beginning of section 7.4, was chosen to generate a slightly conservative test statistic. The data points that exceed the scale of the graph in Figure 7.17 represent incorrect integer ambiguities that were rejected by the filter when they failed the Chi-squared test. As well, the filter azimuth and pitch error results shown in Figure 7.14 do not exhibit the large outliers suffered by the HEAD<sup>TM</sup> results in Figure 7.5. The integrated filter thus shows robustness that the GPS-only system was unable to provide when ambiguity resolution must take place.

External reliability measures for the integrated filter were also calculated and are shown in Figures 7.18 and 7.19. As discussed in Chapter 2, external reliability is the maximum error (ME) that could be caused in the state estimates by a single minimum detectable blunder (MDB). Figure 7.18 shows the ME values for the azimuth and pitch estimates. It can be seen that if the innovation sequence failed to detect a blunder, the resulting azimuth and pitch error would be less than  $4^\circ$ . Since no estimate of the pitch error is

possible without GPS, a blunder cannot affect the pitch during GPS outages and the pitch ME drops to zero.

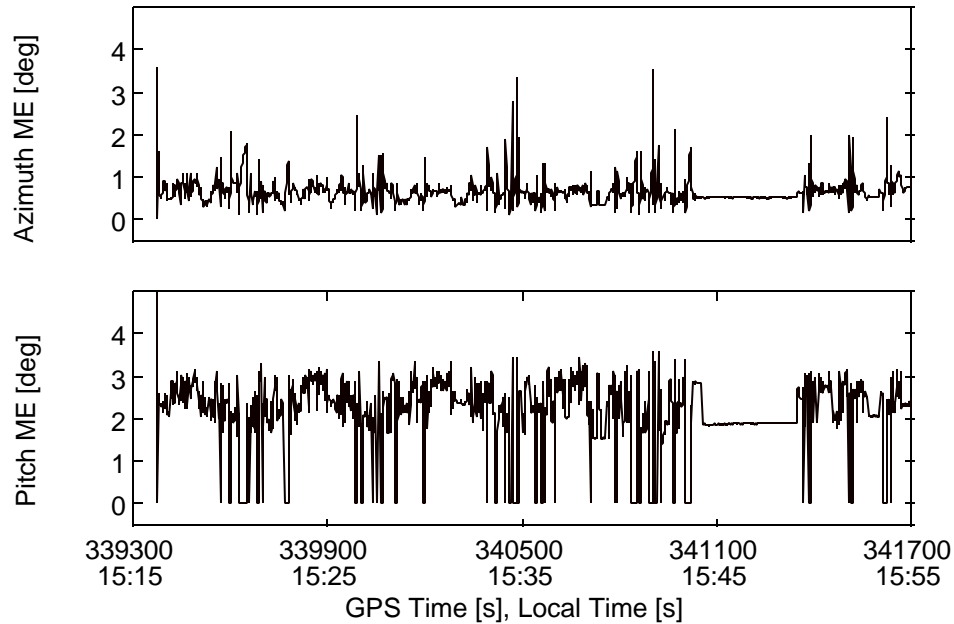


**Figure 7.18 - Maximum azimuth and pitch errors resulting from a measurement blunder not detected by the innovation sequence test.**

Figure 7.19 shows the gyro rate bias ME and the magnetic field error ME. When only compass measurements are available, the magnetic field error is essentially not estimated and the ME is drastically reduced. The gyro rate bias ME is seen to be greatest during the static period when the filter attempts to set the bias error by raising the spectral density based on the good GPS coverage and low azimuth rate.

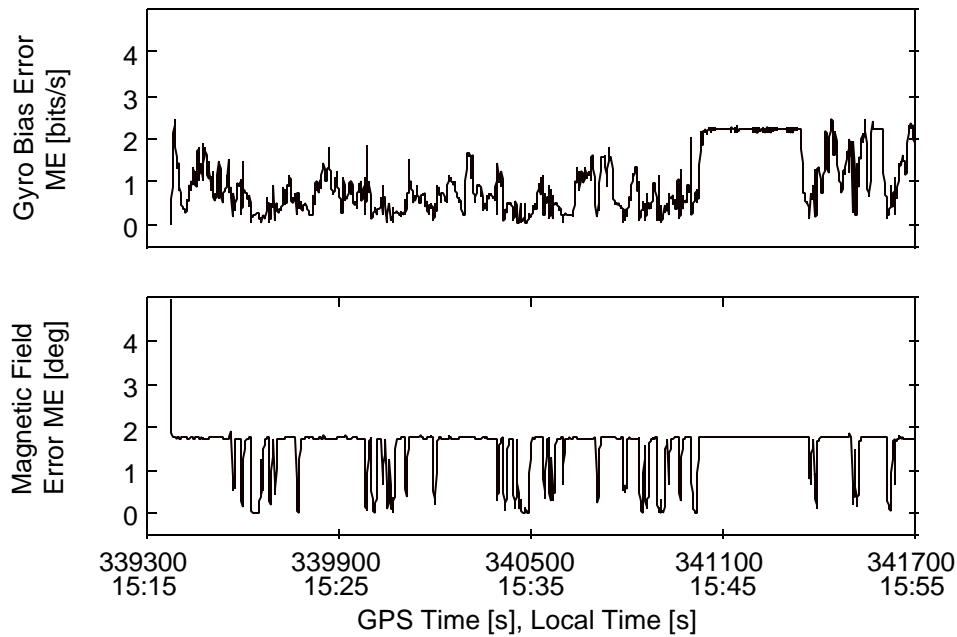


**Figure 7.19 - Maximum gyro rate bias and magnetic field errors resulting from a measurement blunder not detected by the innovation sequence test.**

#### **7.4.2 Suburban GPS Coverage with Induced Periodic 200 s GPS Outages**

To examine the benefit of the adaptive spectral density scheme, 200 s periodic GPS outages were induced in the suburban test in post-mission and the integrated filter results analyzed. In practice, these conditions could be experienced while operating in urban canyons, tunnels and areas of dense foliage. The azimuth and pitch error results are shown in Figure 7.20 along with their  $3\sigma$  error envelopes, with statistics for the whole test period given in Table 7.7. With no GPS, the accuracy of the azimuth estimate was limited in the long-term by the correlated magnetic error of the compass, although the short-term accuracy of the gyro was able to reduce high-frequency noise. The dramatic increase in the estimated error was caused by the single available compass measurement having a large measurement variance. Under these severe operational conditions the estimated error is still able to reflect the true error of the system except near the very end

of the test run. This deviation is caused by a large magnetic field error in the compass measurement which cannot be removed without GPS. The estimate of the pitch during these periods was based solely on the raw tilt measurement with no GPS acceleration correction. The estimated error generated by the filter can be seen to grow in accordance with the true error of the system when the vehicle was in motion.

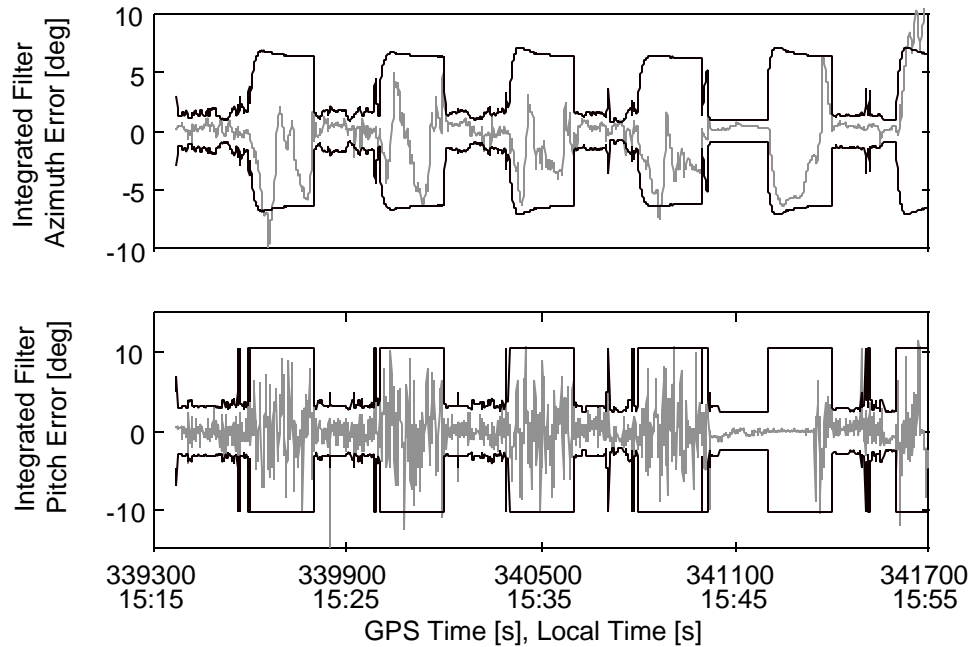


**Figure 7.20 - Integrated filter azimuth and pitch error results including 3s error envelope for suburban run with 200 s periodic GPS outages.**

**Table 7.7 - Integrated filter azimuth and pitch error statistics for suburban run with 200 s periodic GPS outages.**

	Azimuth Error	Pitch Error
Mean	-0.562 °	-0.055 °
Std.Dev.	2.882 °	2.603 °
RMS	2.936 °	2.603 °

During the static period, the true error with GPS available was worse than with the tilt meter alone, but this was not reflected in the filter estimated error. In the filter design, no provision was made to select parameters based on whether the vehicle was static, under the assumption that GPS was the most accurate sensor and without GPS there was no way to determine the vehicle's velocity. Future work could involve examining the tilt meter behaviour under static conditions, for instance while the vehicle was being loaded or unloaded with heavy cargo.

The integrated filter results for the gyro rate bias error are shown in Figure 7.21 along with the effect of applying the estimated bias to the raw gyro error. When only the compass was available, the covariance of the rate bias error was seen to drop, reflecting the inability of the filter to set the gyro bias based on such a noisy measurement. Applied to the raw gyro output, the estimated bias resulted in about 8° less error over 2400 s.

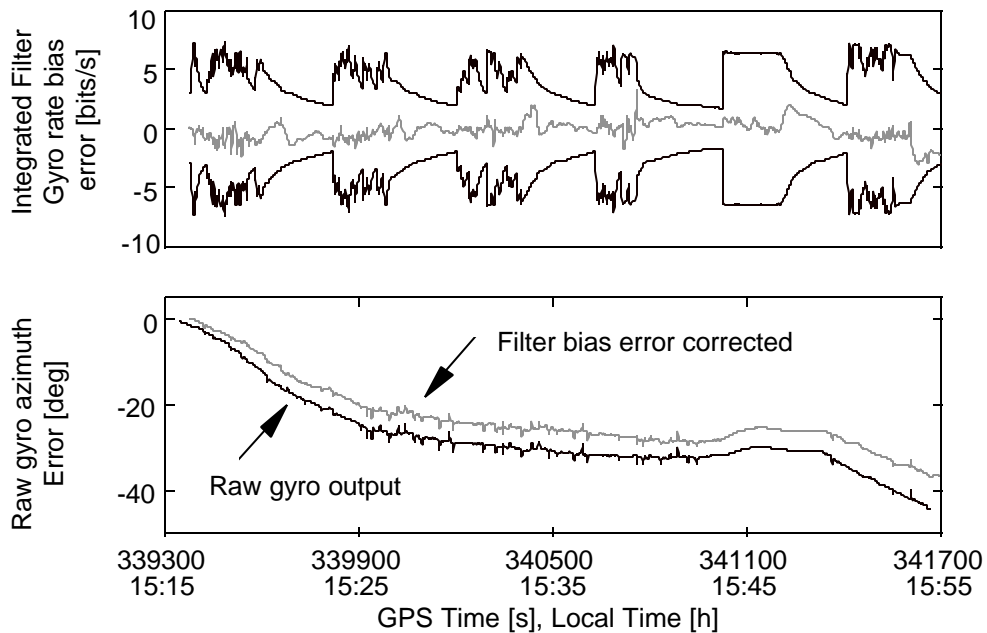


**Figure 7.21 - Integrated filter estimated gyro rate bias error, including 3s error envelope (top) and result of applying estimated bias to raw gyro output (bottom).**

At the end of the test run, the bias error is seen to jump significantly when GPS is not available. This was a direct result of the large azimuth error that exceeded the estimated error envelope at the end of the top graph in Figure 7.20. Since the filter error covariance was too optimistic during this period, the resulting estimation of the rate bias error was suboptimal. This stresses the importance of correctly choosing the filter parameters to estimate the true error of the system. Figure 7.22 shows the estimated magnetic field error and a comparison between the estimated error and the true compass error. When GPS was available, the results were almost identical to Figure 7.16. Without GPS, the magnetic field error was not estimated and the measurement variance for the compass was increased to reflect the larger possible error as discussed in the beginning of section 7.4.

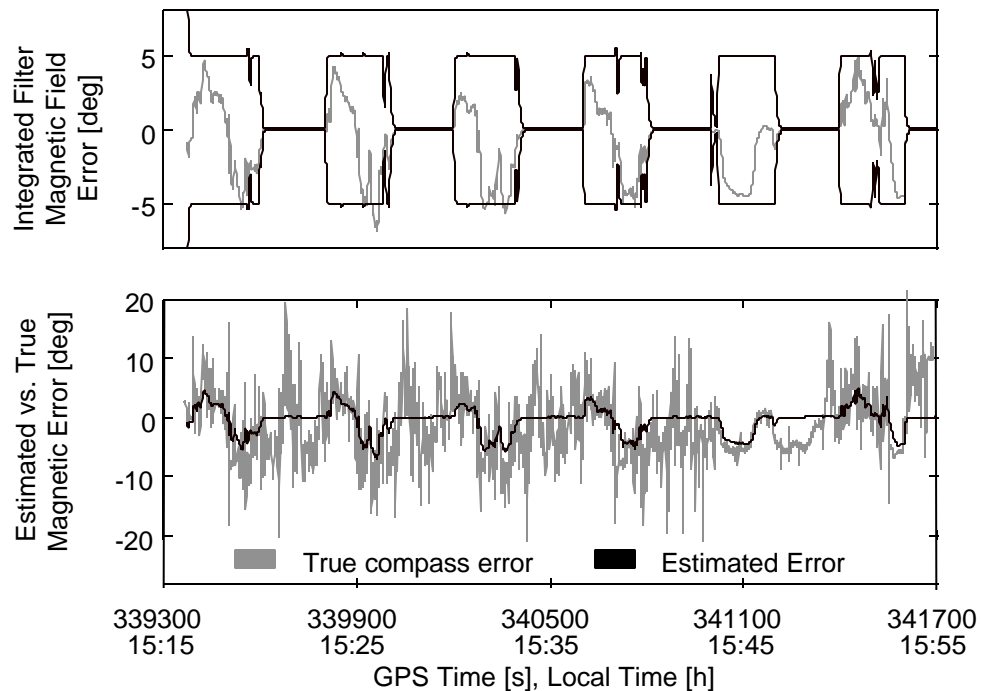


**Figure 7.22 - Integrated filter estimated magnetic field error, including 3s error envelope (top) and comparison of estimated error vs. true compass error (bottom).**

Figure 7.23 shows the results of the innovation sequence testing during the test run with periodic GPS outages. The spikes associated with incorrect ambiguities seen in Figure 7.17 are evident during periods where GPS was available and were similarly rejected.

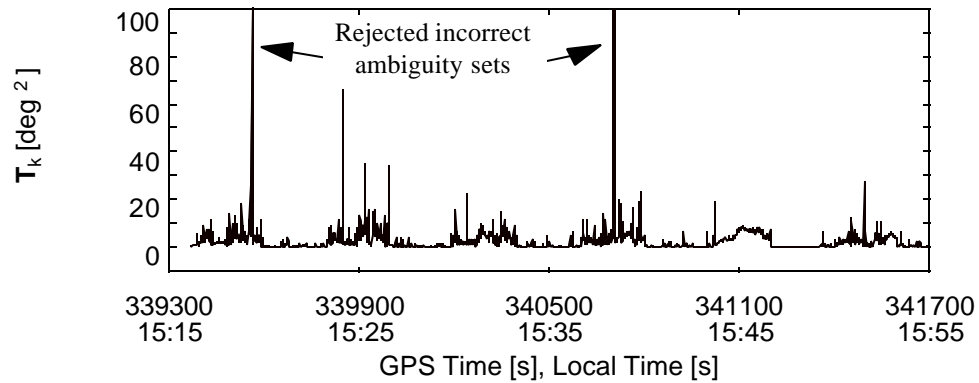


**Figure 7.23 - Innovation test statistic  $T_k$  for integrated filter during suburban run with 200 s periodic GPS outages.**

The effectiveness of the innovation test was limited during periods of GPS outage due to the large measurement variance of the compass. Testing of the innovation sequence was more important with GPS available, to check for incorrect ambiguities which could cause severe errors in the filter estimates.

The maximum errors (ME) in the azimuth and pitch that would be caused by a single minimum detectable blunder (MDB) as defined in Chapter 2 on external reliability are shown in Figure 7.24. Figure 7.25 shows the ME values for the rate bias error and the magnetic field error. With GPS available, the results are very similar to Figure 7.18. The azimuth ME is shown to grow after GPS was lost since blunder detection was more difficult with only the noisy compass measurements. Since the filter does not estimate a correction to the nominal pitch when GPS is not available, it is impossible to introduce a filter error into the pitch estimate and the corresponding ME is zero.

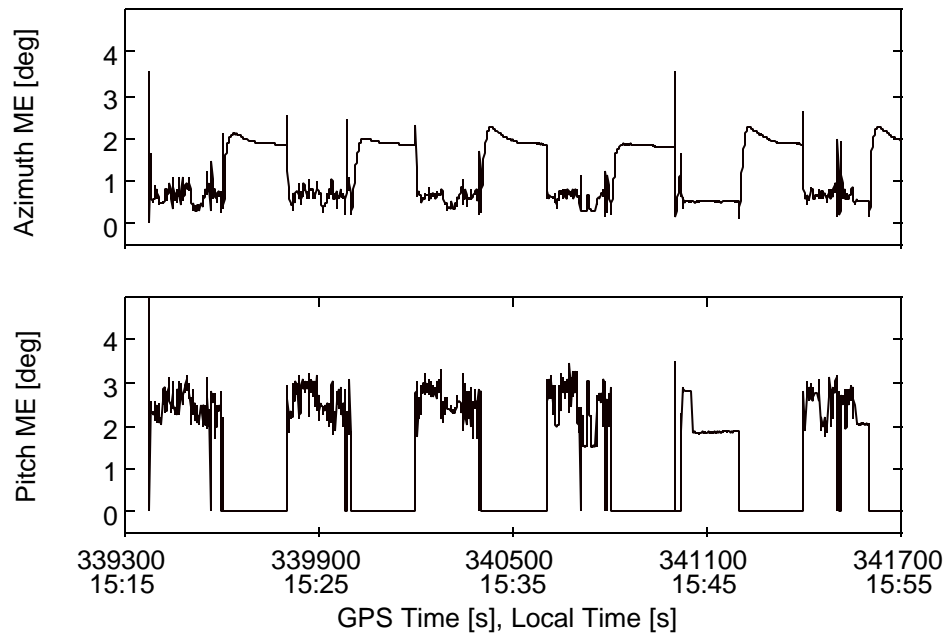


**Figure 7.24 - Maximum azimuth and pitch errors resulting from a measurement blunder not detected by the innovation sequence test (200 s periodic GPS outages).**

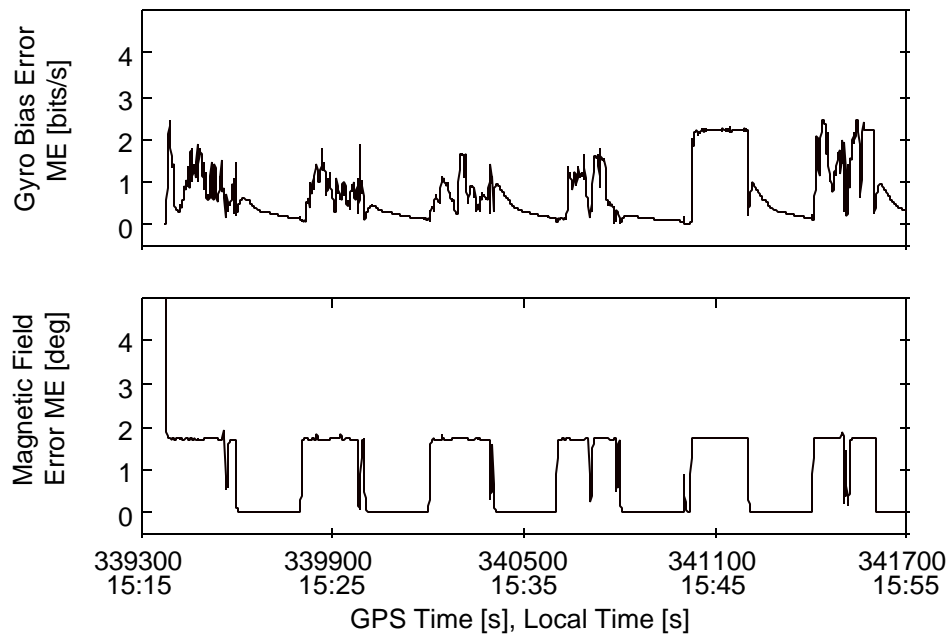


**Figure 7.25 - Maximum gyro rate bias and magnetic field errors resulting from a single undetected measurement blunder (200 s periodic GPS outages).**

The ME that could be induced in the magnetic field error was zero when GPS was not available since the filter did not estimate the state. The ME induced in the gyro rate bias is seen to be smaller during periods of GPS outage, reflecting the lower covariance of the estimate and corresponding increased difficulty in changing it.

### 7.4.3 Suburban GPS Coverage with Induced Long-Term GPS Outage

The effect of a 30 minute prolonged GPS outage was examined by rejecting all GPS records after GPS time 340000 s. This also allowed a comparison of the integrated filter using the compass and gyro versus the raw compass results shown in Figure 7.7. For all graphs in this section, the filter behaviour before GPS time 340000 s was exactly the same as in section 7.4.1. The azimuth and pitch errors for this test are shown in Figure 7.26.

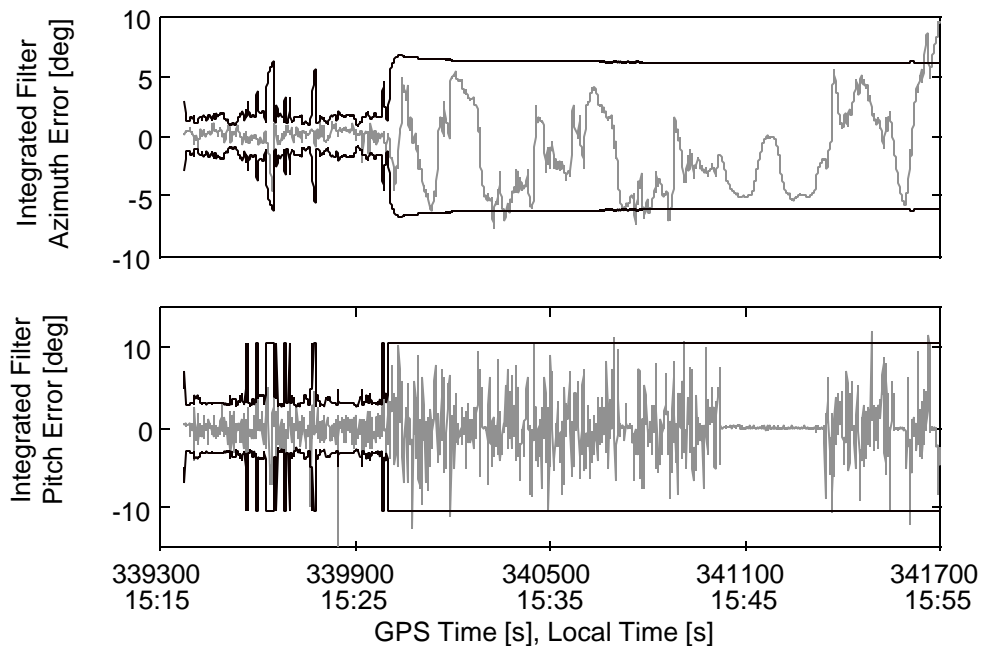


**Figure 7.26 - Integrated filter azimuth and pitch error results including 3s error envelope for suburban run with no GPS after 340000 s.**

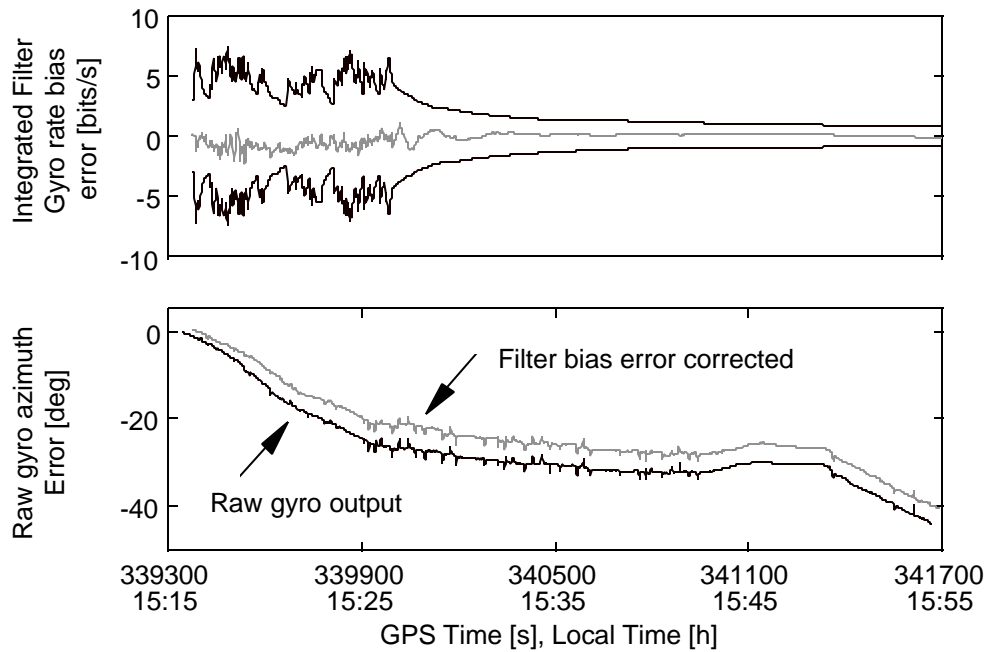
In azimuth, the error envelope is seen to accurately reflect the true error of the estimate for the majority of the test period. The filter suffered from a severe magnetic error near the end of the test which was outside of the error envelope, similar to Figure 7.20. The true pitch error was well within the estimated error envelope, but was drastically overestimated during the static period. As mentioned in the previous section, there was no way to determine when the vehicle was static without GPS. Filter azimuth error statistics for the period after GPS time 340000 s are given in Table 7.8, along with the raw compass results taken from Figure 7.7 for the same period.

**Table 7.8 - Comparison of raw compass error versus filter error when using the compass and gyro to estimate azimuth, after GPS time 340000 s.**

	Raw compass azimuth error	Filter azimuth error using compass and gyro
Mean	-1.095 °	-1.357 °
Std.Dev.	5.770 °	3.590 °
RMS	5.872 °	3.837 °

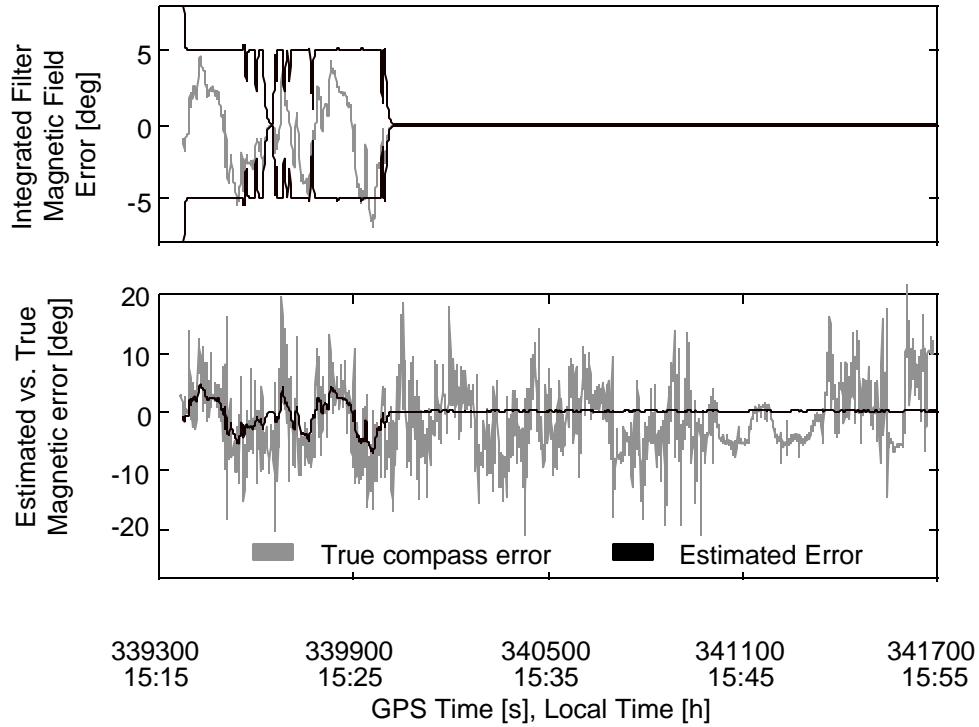
It can be seen that the filter results are significantly better, mostly due to the removal of high-frequency noise through use of the gyro. The estimated rate bias error is shown in Figure 7.27, along with the effect of applying the estimated bias to the raw gyro output. The error envelope is seen to decay after GPS was lost and restricted the bias error from changing. The sudden jump in the bias error at the end of the top graph of Figure 7.21 is not evident in Figure 7.27. The jump occurred because the estimated azimuth error was too optimistic and the filter placed too much confidence in the measurement. In this case,

the bias error filter variance was low enough that the over-optimistic measurement could not adversely effect the bias error. The improvement in the raw gyro output reached about  $5^\circ$  but was constant after GPS time 340000 s. This was to be expected since the compass measurement was too noisy to accurately set the bias.



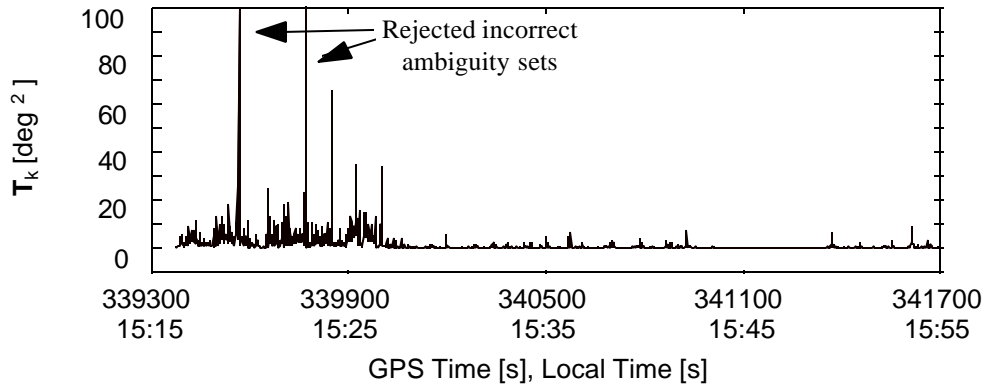
**Figure 7.27 - Integrated filter estimated gyro rate bias error, including 3s error envelope (top) and result of applying estimated bias to raw gyro output (bottom).**

Figure 7.28 shows the estimated magnetic field error and associated error envelope, along with a comparison between the true and estimated compass error. Without GPS, the magnetic field error was not estimated.



**Figure 7.28 - Integrated filter estimated magnetic field error, including 3s error envelope (top) and comparison of estimated error vs. true compass error (bottom).**

Results of the innovation sequence testing were very similar to section 7.4.2 when no GPS was available. The innovation sequence test statistic  $T_k$  is shown in Figure 7.29. The external reliability measures from Chapter 4 are given in Figures 7.30 and 7.31 for the case of a single undetected measurement blunder. Without GPS, the maximum error (ME) that could be induced into the pitch and magnetic field error is zero. The ME for the gyro rate bias error decays rapidly and reflects the resistance to change mentioned for Figure 7.27.



**Figure 7.29 - Innovation test statistic  $T_k$  for integrated filter during suburban run with no GPS after 340000 s.**

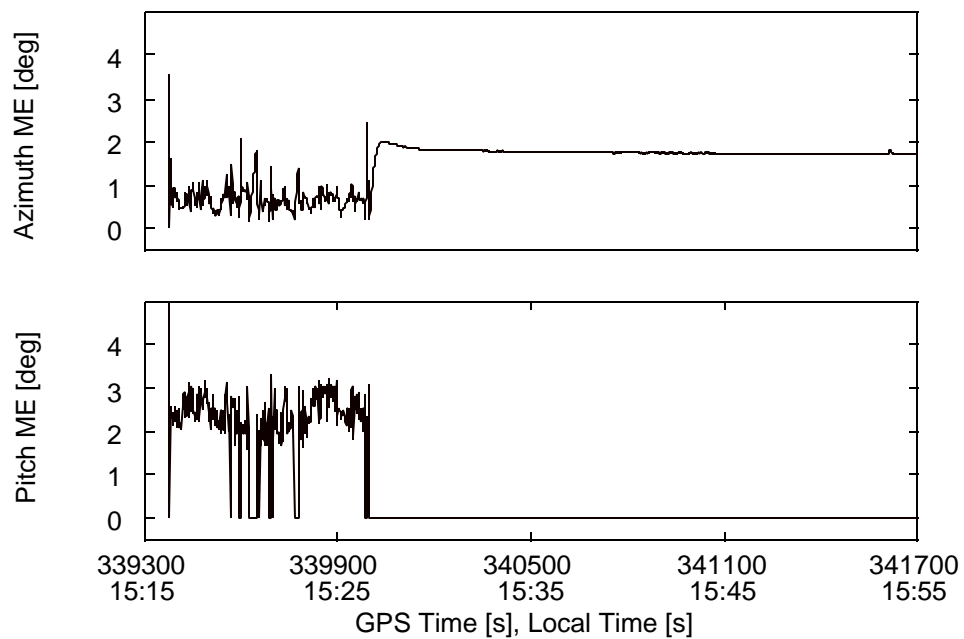


**Figure 7.30 - Maximum azimuth and pitch errors resulting from a measurement blunder not detected by the innovation sequence test (no GPS after 340000 s).**

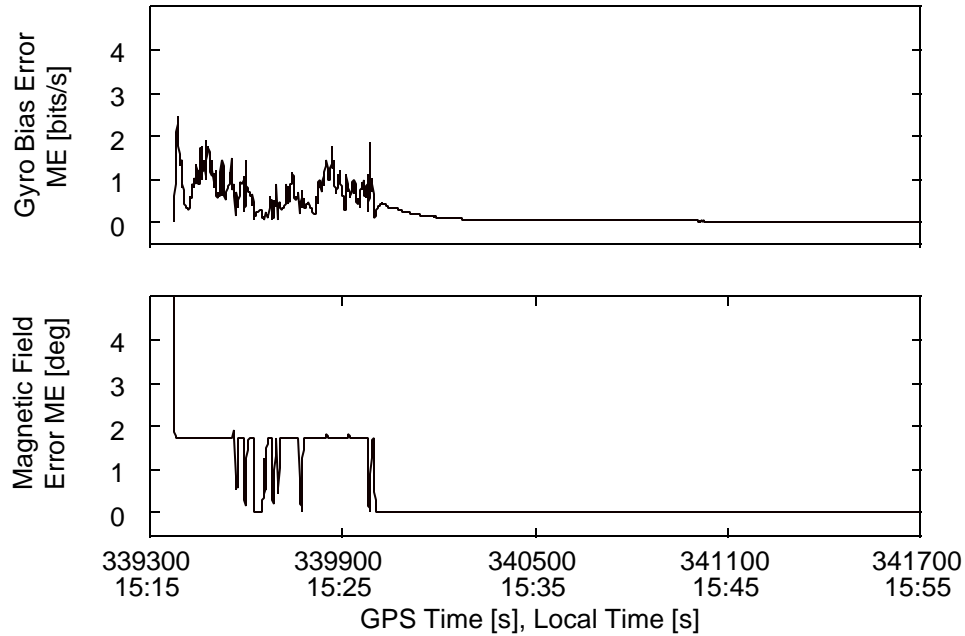


**Figure 7.31 - Maximum gyro rate bias and magnetic field errors resulting from a measurement blunder not detected by the innovation sequence test (no GPS after 340000 s).**

#### 7.4.4 Suburban GPS Coverage using a 25° and 35° Mask Angle

Another consideration when testing the system was the ability of the integrated filter to operate in urban canyon situations. These conditions are characterized by a high satellite elevation cut-off angle caused by buildings and other obstructions that restrict line-of-sight for satellites closer to the horizon. Two cases are considered here, first for a 25° mask angle and second for a 35° mask angle. The number of satellites visible using a 25° mask angle is shown in Figure 7.32. The integrated filter must have a minimum of four satellites, but if the visible number drops below four then ambiguities are lost. To resolve the ambiguities, five visible satellites are required. It can be seen that the integrated filter azimuth solution in Figure 7.33 reverts to the compass measurement when the number of visible satellites degrades below four at about GPS time 341400 s. Since five satellites are not tracked simultaneously after this point, ambiguity resolution was not possible. In

addition there are increased instances of GPS outage prior to this period when compared to Figure 7.14, indicated by the variance envelope. The pitch estimate is given by the tilt meter. The results are identical to Figure 7.26 for this period.

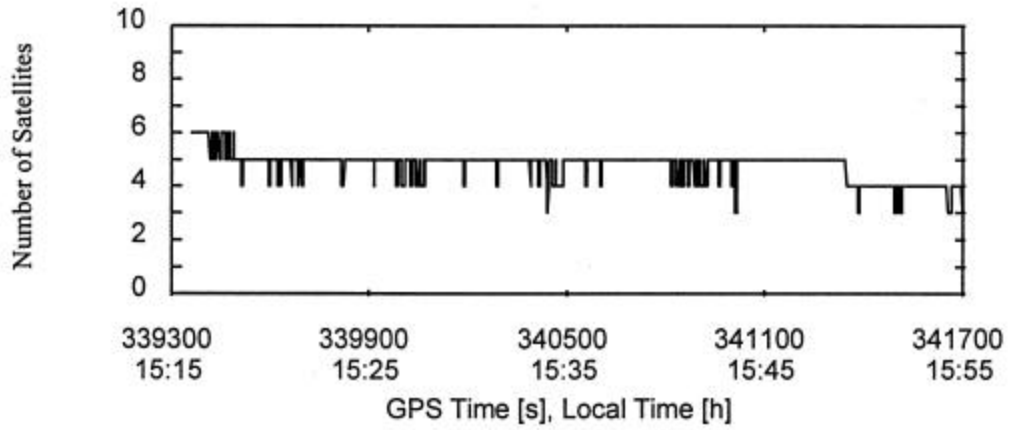


**Figure 7.32 – Number of visible satellites above 25° mask angle**

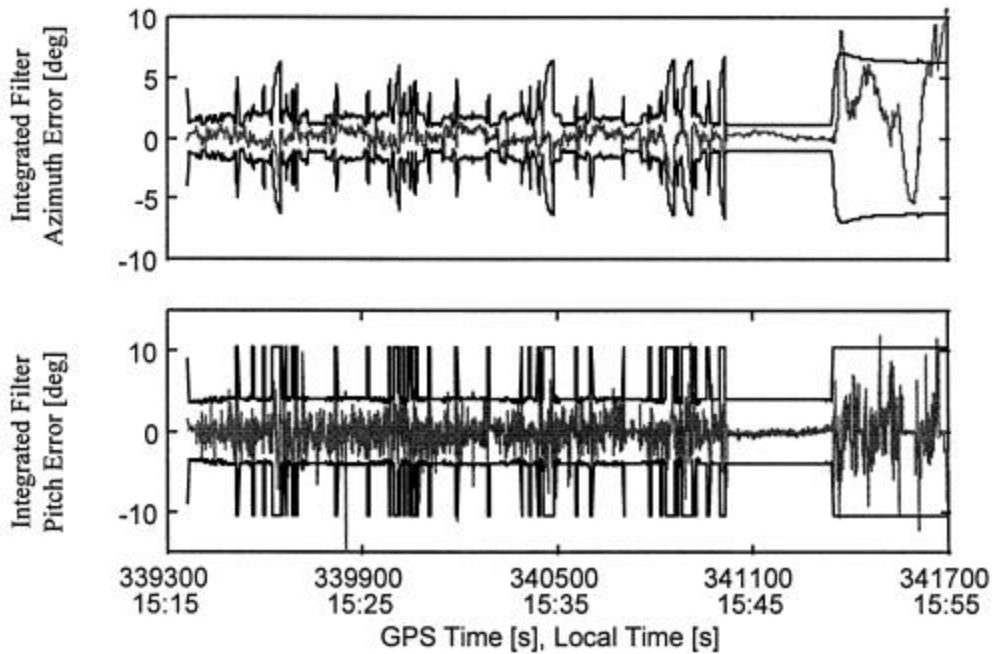


**Figure 7.33 – Integrated filter azimuth and pitch error results, including 3s error envelope for suburban run and 25° mask angle.**

The number of satellites visible for a 35° mask angle is shown in Figure 7.34. The number of visible satellites drops below four at about GPS time 339850 s. The integrated filter results for this period are shown in Figure 7.35. It can be seen that the effects of the 35° mask angle is very similar to the results shown in section 7.4.3 when GPS was denied after GPS time 340000 s. As mentioned in Chapter 6, no attempt was made to use GPS measurements when less than four satellites were visible. It can be seen in Figure 7.32 and 7.34 that even with a high mask angle there are still a number of GPS measurements which are available and, in this case, not used. In future, an attempt could be made to augment the integrated system to accept GPS measurements under reduced coverage to take advantage of this information and improve the pointing solution.

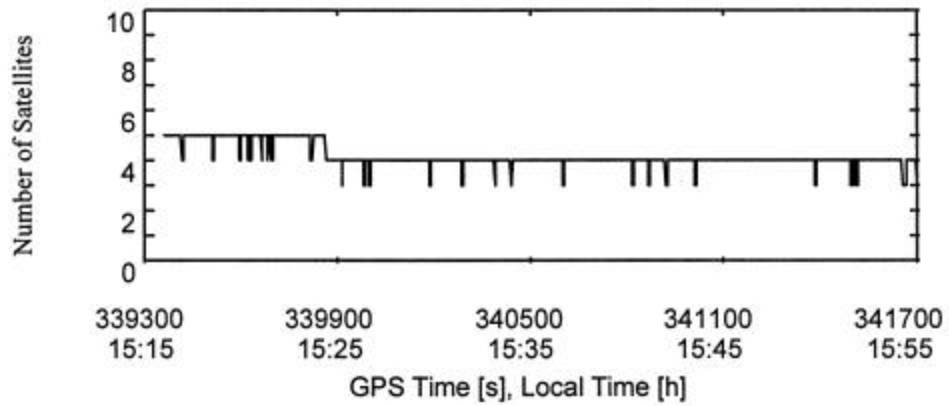


Figure 7.34 – Number of visible satellites above 35° mask angle

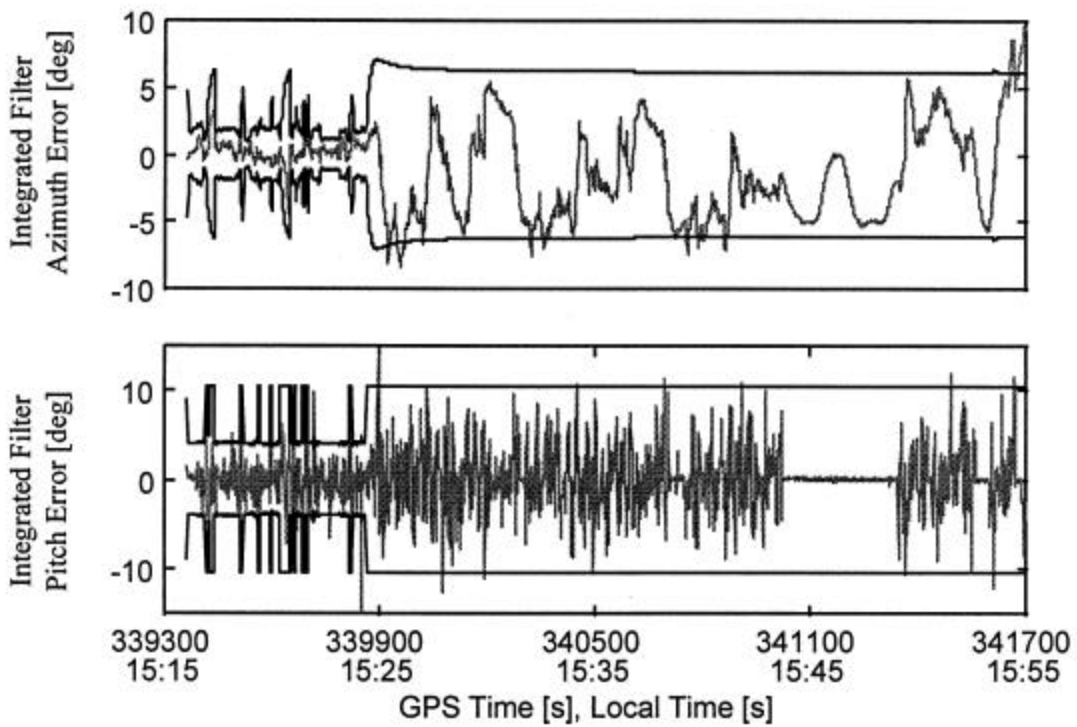


Figure 7.35 – Integrated filter azimuth and pitch error results, including 3s error envelope for suburban run and 35° mask angle.

## **CHAPTER 8**

### **CONCLUSIONS AND RECOMMENDATIONS**

A precision pointing system using an integrated multi-sensor approach was developed and tested. The primary sensor is GPS, in the form of a dual-antenna fixed baseline system. This was augmented by a fiber-optic gyro and a combined electronic compass and tilt meter. The non-GPS sensors were used to bridge periods of GPS outage and reduce the size of the carrier phase ambiguity search space. To collect and properly time-tag the sensor data, a hardware system was developed and tested.

A software processing package was developed which followed an aided sensor approach. GPS and compass measurements were used in an extended centralized Kalman filter to estimate the errors in a nominal orientation generated using the fiber-optic gyro and tilt meter pitch measurement. Innovation sequence testing was implemented to monitor filter performance along with external reliability measures to determine the effect of a single undetected measurement blunder. To improve the performance of the system, certain sensor errors were also included as filter states to be estimated when GPS was fully available. To avoid corrupting the sensor error states when incorrect ambiguities were chosen an adaptive spectral density scheme was developed. The system output included the azimuth, pitch, compass magnetic field error and gyro rate bias error along with the estimated variance for each state. The centralized filter, innovation sequence test and adaptive spectral density scheme were described in detail.

To validate the system, a test run through a suburban area of Calgary was executed in October, 1997 and the results compared to an accurate GPS/INS reference. The performance capabilities and error behaviour of the individual sensors were examined in detail. A GPS-only system, using an independent processing software package called HEAD™, demonstrated the highest accuracy but suffered from large outliers due to incorrect ambiguities and a loss of solution when GPS was unavailable.

The tilt meter measurement error demonstrated a high degree of time-correlation due to vehicle acceleration. GPS derived accelerations were used successfully to remove most of the time-correlation in the error caused by motion of the vehicle. Additionally, using the GPS correction, the total tilt meter pitch error was reduced by over 40%, from 3.21° rms to 1.87° rms while the roll error was reduced by about 20%, from 3.27° rms to 2.59° rms.

The compass performance was shown to be significantly worse than expected, having an rms error of 6° when compared to the reference. The compass error was also shown to exhibit high time correlation due to slowly varying magnetic effects. No correction was available with the current hardware to remove this error. To maintain the assumption that all measurements to the Kalman filter be white, the correlated part of the magnetic field error was included as a state in the filter. A new temperature dependent scale factor for the FOG was developed to reduce scale factor error. The FOG suffered from an integrated measurement bias error caused mainly by the quantization level. The effect of the bias error was included as a filter state to try and reduce drift error when GPS was not available.

The integrated filter error over the suburban test was 0.66° rms in azimuth and 1.51° rms in pitch. The estimated error was shown to be reflective of the true error of the system. Compared to the GPS-only system with correct ambiguities and full view of the sky, the filter performance was slightly worse. The GPS-only system, however, suffered from outliers caused by incorrect ambiguities which the filter did not. Over the whole test period with the outliers included, the filter performance was superior. With the innovation sequence testing in place, the filter was able to detect incorrect ambiguities before corrupting the filter states. The integrated filter also provided a solution for 100%

of the test period compared to 77% for the GPS-only system after the outliers were removed.

In terms of the sensor errors, the estimated magnetic field error was shown to reflect the low-frequency component of the compass error. The estimated gyro rate bias error when applied to the raw gyro output resulted in a  $34^\circ$  error over 2400 s as opposed to a  $44^\circ$  error.

To test the effectiveness of the system when GPS was not available, GPS outages were induced in the suburban test. The estimated error growth of the filter was shown to grow and reflect the true error of the system when GPS was not available. An examination of the filter results for a twenty-five minute period with no GPS showed an azimuth error of  $3.8^\circ$  rms compared to  $5.8^\circ$  rms with the compass alone. This was due to the reduction of high frequency error caused by the integration of the gyro. The error behaviour of the pitch result was the same as for the raw tilt meter since no correction was estimated by the filter.

In terms of improving the performance of the system, the following recommendations and modifications could be made:

1. Test the filter for the case of reduced satellite coverage. This would involve augmenting the adaptive spectral density scheme for the reduced GPS case and ensuring that the correct carrier phase ambiguities would be maintained.
2. Develop a method for more accurate calibration of the TCM2 compass in the vertical direction. This could potentially improve the performance of the magnetic anomaly detector.
3. The system performance should be tested for different GPS inter-antenna baselines.

4. When the vehicle is stationary, a method could be developed for taking advantage of the highly precise tilt meter measurements. A velocity or distance sensor would be necessary if GPS were not available, potentially a vehicle odometer.
5. The effect of replacing the current gyro with a better quality one should also be examined. This gyro could have a checksum to aid in data integrity. This could increase the short term bridging ability when GPS is not available. The effect of a longer GPS baseline on predicting the new gyro bias should also be examined as this could increase the effectiveness of the system for long-term use.
6. The temperature dependent scale factor and bias effects could be examined in more detail. For a higher quality gyro the quantization error would be considerably less and temperature effects could be the dominant error.
7. The current GPS receivers could be replaced with less expensive receivers to reduce the overall cost of the system. This would most likely increase the magnitude of the multipath error which could be countered by increasing the baseline length.
8. The system estimate of pitch could be improved when GPS is not available and the vehicle is moving. Another sensor could be considered to increase the pitch accuracy.
9. A real-time system could be developed. This would involve redeveloping the hardware data logging architecture presented in this thesis. A dedicated timing and I/O board would be an asset to remove some of the processing load and interrupt routines in the PC.
10. The current system could also be augmented to accept differential corrections to allow for more precise positioning of the vehicle. This would increase the functionality of the system since both precise pointing and precise positioning would be available.
11. A more robust innovation sequence testing procedure could be developed to try and identify multiple measurement blunders.

## REFERENCES

- Abbott, E., D. Powell, (1995) : *An Examination of the Relative Merits of Various Sensors for Vehicle Navigation*, **ION GPS-95**, Palm Springs, CA, Sept. 1995. pp.1269-1284.
- Abousalem, M.A. (1993) : **Development of a Robust GPS Kinematic Positioning Module for Automatic Vehicle Location and Navigation Systems**, M.Sc. Thesis, UCGE report 20077, Department of Geomatics Engineering, The University of Calgary, Alberta, Canada.
- Andrew Corporation (1994) : **AUTOGYRO™ Installation Manual**, Document 237318, rev. A, November.
- Braasch. M. (1995) : *Multipath Effects, Global Positioning System : Theory and Applications, Progress in Astronautics and Aeronautics (AIAA)*, Vol. 163, Washington, D.C., 1996. pp.547-568.
- Brown, R.G., P.Y.C. Hwang, (1992) : **Introduction to Random Signals and Applied Kalman Filtering**, 2nd Edition, John Wiley and Sons Inc., Toronto, Canada.
- Cannon, M.E, J.B. Schleppe, J.F. McLellan, (1992) : *Real-Time Heading Determination Using an Integrated GPS-Dead Reckoning System*, **ION GPS-92**, Albuquerque, NM, September 1992. pp.767-773.
- Cannon, M.E., M. Haverland, (1993) : *Experiences of GPS Attitude Determination within a Helicopter Pod*, **ION GPS-93**, Salt Lake City, UT, September 1993. pp. 633-642.
- Cannon, M.E., H. Sun, T.E. Owen, M.A. Meindl (1994) : *Assessment of a Non-Dedicated GPS receiver System for Precise Airborne Attitude Determination*, **ION GPS-94**, Salt Lake City, UT, September 1994. pp. 645-653.
- Cannon, M.E., G. Lachapelle, R.S. Harvey (1996) : **Development of a Low Cost GPS Attitude Determination System**, Report for the Defence Research Establishment, Department of Geomatics Engineering, University of Calgary, Alberta, Canada.
- Chelsey, B., P. Axelrad, (1994) : *An Integrated GPS Attitude Determination System for JAWSAT*, **ION GPS-94**, Salt Lake City, UT, September 1994. pp.1251-1261.
- Chen, D.S., G. Lachapelle (1994) : *A Comparison of the FASF and Least-Squares Search Algorithms for Ambiguity Resolution On the Fly*, **Kinematic Systems in Geodesy, Surveying, and Remote Sensing**, KIS94, Banff, Alberta, Canada. pp.241-253.
- Cohen, C. (1992) : **Attitude Determination using GPS**, Ph.D. Thesis, Department of Aeronautics and Astronautics, Stanford University, California, U.S.A.

Counselman, C.C., S.A. Gourevitch (1981) : *Miniature Interferometer Terminals for Earth Surveying: Ambiguity and Multipath with Global Positioning System*, **IEEE Transactions on Geoscience and Remote Sensing**, Vol. GE-19, No 4. pp.244-252.

Dumaine, M. (1996) : *High Precision Attitude Using Low Cost GPS Receivers*, **ION GPS-96**, Kansas City, KS, September 1996. pp.1029-1035.

Duval, R., P. Heroux, N. Beck (1996) : *Canadian Active Control System - Delivering the Canadian Spatial Reference System*, **GIS '96**, Vancouver, Canada, March 1996.

El-Mowafy, A. (1994) : **Kinematic Attitude Determination from GPS**, Ph.D. Thesis, UCGE report 20074, Department of Geomatics Engineering, The University of Calgary, Alberta, Canada.

Euler, I.H., C. Hill, (1995) : *Attitude Determination : Exploiting all Information for Optimal Ambiguity Resolution*, **ION GPS-95**, Palm Springs, CA, September 1995. pp.1751-1756.

Ford, T., W. Kunysz, R. Morris, J. Nuemann, J. Rooney, T. Smit (1997) : *Beeline RT-20 - A Compact, Medium Precision Positioning System with an Attitude*, **ION GPS-97**, Kansas City, MO, September 1997. pp.687-695.

Frei, E., G. Beutler (1990) : *Rapid Static Positioning Based on the Fast Ambiguity Resolution Approach 'FARA' : Theory and First Results*, **Manuscript Geodetica**, Vol. 15. pp.325-356.

Gao, Y. (1992) : **A Robust Quality Control System for GPS Navigation and Kinematic Positioning**, Ph.D. Thesis, UCGE report 20075, Department of Geomatics Engineering, The University of Calgary, Alberta, Canada.

Geier, G.J., (1995) : **Special Studies in GPS Integration with Low Cost Sensors**, Department of Geomatics Engineering, The University of Calgary, Alberta, Canada, August.

Gelb, A., (1974) : **Applied Optimal Estimation**, The M.I.T. Press, Cambridge, MA.

Gilkey, J., D. Richardson, C. Terndrup, (1995) : *A Single-Baseline Attitude Measurement System Using Low-Cost C/A Code Receivers*, **ION GPS-95**, Palm Springs, CA, September 1995. pp.1723-1731.

Harvey, R., M.E. Cannon (1997) : *Operational Results of a Closely Coupled Integrated Vehicle Heading System*, **ION GPS-97**, Kansas City, MO, September 1997. pp.279-288.

Hatch, R. (1990) : *Instantaneous Ambiguity Resolution*, **Kinematic Systems in Geodesy, Surveying, and Remote Sensing**, KIS90, Symposium no. 107, Banff, Alberta, Canada. pp.299-308.

Hayashi, N. (1996) : **Augmentation of GPS with a Barometer and a Heading Rate Gyroscope for Urban Vehicular Navigation**, M. Sc. Thesis, UCGE report 20098, Department of Geomatics, The University of Calgary, Alberta, Canada.

Hayward, R.C., D. Gebre-Egziabher, M. Schwall, J.D. Powell (1997) : *Inertially Aided GPS Based Attitude Heading and Reference System (AHRS) for General Aviation Aircraft*, **ION GPS-97**, Kansas City, MO, September 1997. pp.289-298.

Hofmann-Wellenhof, B., H. Lichtenegger, J. Collins (1994) : **Global Positioning System: Theory and Practice**, Springer-Verlag, New York, NY.

Howell, G., W. Tang, (1995) : *Tightly Coupled Attitude Determination Using GPS Carrier Phase Observables*, **ION GPS-95**, Palm Springs, CA, September 1995. pp.1759-1766.

Jurgens, R.D., C.E. Rodgers, L.C. Fan (1991) : *Advances in GPS Attitude Determining Technology as Developed for the Strategic Defense Command*, **ION GPS-91**, Albuquerque, NM, September 1991. pp.991-999.

Kalman, R.E., (1960) : *A New Approach to Linear Filtering and Prediction Problems*, **Journal of Basic Engineering (ASME)**, Vol. 82D, March 1960. pp.35-45.

Klobuchar, J.A. (1996) : *Ionospheric Effects on GPS*, **Global Positioning System : Theory and Applications, Progress in Astronautics and Aeronautics (AIAA)**, Vol. 163, Washington, D.C., 1996. pp.485-516.

Knight, J., R. Hatch, (1990) : *Attitude Determination using GPS*, **Kinematic Systems in Geodesy, Surveying, and Remote Sensing**, KIS90, Banff, Alberta, Canada, June. pp.168-177.

Krakiwsky, E.J. (1990) : **The Method of Least Squares: A Synthesis of Advances**, UCGE Report 10003, Department of Geomatics Engineering, The University of Calgary, Alberta, Canada.

Krakiwsky, E.J., M.A. Abousalem, (1995) : **Adjustment of Observations**, UCGE Report 10015, Department of Geomatics Engineering, The University of Calgary, Alberta, Canada.

Kruczynski, L., J. Delucchi, (1995) : *Results of DC-10 Tests Using GPS Attitude Determination*, **ION GPS-95**, Palm Springs, CA, September 1995. pp.1743-1750.

Lachapelle, G. (1995) : **ENGO 625 GPS Theory and Applications**, Department of Geomatics Engineering, The University of Calgary, Alberta, Canada, Fall.

Lachapelle, G., G. Lu, B. Loncarevic, (1994) : *Precise Shipborne Attitude Determination Using Wide Antenna Spacing*, **Kinematic Systems in Geodesy, Surveying, and Remote Sensing**, KIS94, Banff, Alberta, Canada. pp.323-330.

Lan, H. (1996) : **Development of a Real-Time Kinematic GPS System: Design, Performance and Results**, M.Sc. Thesis, UCGE report 20107, Department of Geomatics Engineering, The University of Calgary, Alberta, Canada.

Liu, R.Y., G.W. Adams (1995) : *Interferometric Fiber-Optic Gyroscopes: A Summary of Progress*, **IEEE Position, Location and Navigation Symposium**, PLANS 1990. pp.31-35.

Lu, G. (1995) : **Development of a GPS Multi-Antenna System for Attitude Determination**, Ph.D. Thesis, UCGE Report 20073, Department of Geomatics Engineering, The University of Calgary, Alberta, Canada.

Lu, G., G. Lachapelle, (1990) : *Reliability Analysis Applied to Kinematic GPS Position and Velocity Estimation*, **Kinematic Systems in Geodesy, Surveying, and Remote Sensing**, KIS90, Symposium no. 107, Banff, Alberta, Canada. pp.273-284.

Lu, G., G. Lachapelle, M.E. Cannon, (1993) : *Attitude Determination in a Survey Launch Using Multi-Antenna GPS Technology*, **ION National Technical Meeting 1993**, San Francisco, CA, January 1993. pp.251-260.

Mader, G.L. (1990) : *Ambiguity Function Techniques for GPS Phase Initialization and Kinematic Solutions*, **Proceedings of the Second International Symposium on Precise Positioning System**, The Canadian Institute of Surveying and Mapping, Ottawa, September. pp.1233-1247.

Malys, S., J.A. Slater, R.W. Smith, L.E. Kunz, S.C. Kenyon (1997) : *Status of the World Geodetic System 1984*, **Kinematic Systems in Geodesy, Surveying, and Remote Sensing**, KIS97, Banff, Alberta, Canada, March 1997. pp.25-34.

Martinelli, V., R. Ikeda (1995) : *Next Generation Fiber Optic Gyroscopes for Use with GPS in Vehicle Navigation and Location Systems*, **ION GPS-95**, Palm Springs, CA, September 1995. pp.1295-1299.

McBurney, P.W. (1990) : *A Robust Statistical Approach to Reliable Real-Time Kalman Filtering*, **IEEE Position, Location and Navigation Symposium**, PLANS 1990. pp.549-556.

McLellan, J.F. (1992) : **Design and Analysis of a Low Cost GPS Aided Navigation System**, M. Sc. Thesis, UCGE Report 20097, Department of Geomatics Engineering, The University of Calgary, Alberta, Canada.

NovAtel Communications Ltd. (1995) : **GPSCard™ Commands Descriptions Manual**, Revision 2.0.

Newby, S., P. Fenton, J. Neumann, B. Townsend (1996) : *Core Technology Developments and End-user Products at NovAtel*, **ION GPS-96**, Kansas City, MO, September 1996. pp.117-123.

Parkinson, B.W., (1994) : *Introduction and Heritage of NAVSTAR, the Global Positioning System*, **Global Positioning System : Theory and Applications, Progress in Astronautics and Aeronautics (AIAA)**, Vol. 163, Washington, D.C., 1996. pp.3-28.

Precision Navigation, Inc. (1997) : **TCM2 Electronic Compass Module, User's Manual**, Revision 1.03, May.

Qiu, W. (1993) : **An Analysis of Some Critical Error Sources in Static GPS Surveying**, M.Sc. Thesis, UCGE Report 20054, Department of Geomatics Engineering, The University of Calgary, Alberta, Canada.

Remondi, B.W. (1984) : **Using the Global Positioning System (GPS) Phase Observable for Relative Geodesy: Modeling, Processing and Results**, Ph.D Thesis, Center for Space Research, The University of Texas, Austin.

Schleppe, J.B. (1996) : **Development of a Real-Time Attitude system Using a Quaternion Parameterization and Non-Dedicated GPS Receivers**, M.Sc. Thesis, UCGE report 20096, Department of Geomatics Engineering, The University of Calgary, Alberta, Canada.

Schwarz, K.P., M. Wei (1997) : **ENGO 623 : INS/GPS Integration for Geodetic Applications**, Department of Geomatics Engineering, The University of Calgary, Alberta, Canada, Winter.

Schwarz, K.P., A. El-Mowafy, M. Wei, (1992) : *Testing a GPS Attitude System in Kinematic Mode*, **ION GPS-92**, Albuquerque, NM, September 1992. pp.801-809.

Siouris, G.M. (1993) : **Aerospace Avionics Systems : A Modern Synthesis**, Academic Press, Inc, San Diego, CA.

Skaloud, J. (1995) : **Strapdown INS Orientation Accuracy with GPS Aiding**, M. Sc. Thesis, UCGE report 20079, Department of Geomatics Engineering, The University of Calgary, Alberta, Canada.

Spilker, J.J., (1994) : *Tropospheric Effects on GPS*, **Global Positioning System : Theory and Applications, Progress in Astronautics and Aeronautics (AIAA)**, Vol. 163, Washington, D.C., 1996. pp.517-546.

St. Lawrence, W. (1993) : **Understanding Tilt Vectors and Processing Tiltmeter Data**, Applied Geomechanics Inc, Santa Cruz, CA, February.

Sun, H., M.E. Cannon (1995) : **HEAD™ Operator's manual**, Department of Geomatics Engineering, The University of Calgary, August.

Townsend, B.R., P.C. Fenton, K.J. Van Dierendonck, D.J.R. Van Nee (1995) : *L1 Carrier Phase Multipath Error Reduction Using MEDLL Technology*, **ION GPS-95**, Palm Springs, CA, September 1995. 1539-1544.

Teunissen, P.J.G., (1990) : *Quality Control in Integrated Navigation Systems*, **IEEE Position, Location and Navigation Symposium**, PLANS 1990. pp.158-165.

Vanicek, P., E.J. Krakiwsky (1981) : **Geodesy: The Concepts**, North-Holland, Amsterdam, The Netherlands.

Van Graas, F. (1996) : *Signals Integrity, System Implications and Innovative Applications of Satellite Navigation*, AGARD lecture series 207, Neuilly-Sur-Seine, France. pp.7.1-7.12.

Van Graas, F., M. Braasch (1991): *GPS Interferometric Attitude and Heading Determination: Initial Flight Test Results*, **Navigation: Journal of The Institute of Navigation**, Vol. 38, No. 4, Winter 1991. pp.297-316.

Van Graas, F., M. Braasch (1994) : *Selective Availability, Global Positioning System : Theory and Applications*, **Progress in Astronautics and Aeronautics (AIAA)**, Vol. 163, Washington, D.C., 1996. pp.601-622.

Van Graas, F., J.L. Farrell, (1993) : *Baseline Fault Detection and Exclusion Algorithm*, **ION 49th Annual Meeting**, Cambridge, MA, June 1993. pp.413-419.

Van Graas, F., K. Dutton (1997) : *Experiments With Two-Satellite Instantaneous Attitude Determination*, **ION GPS-97**, Kansas City, MO, September 1997. pp.261-268.

Vinnins, M., L.D. Gallop (1997) : *GPS as a Method of Heading Determination in a Short Baseline Application in the Canadian Arctic*, **Kinematic Systems in Geodesy, Surveying, and Remote Sensing**, KIS97, Banff, Alberta, Canada, March 1997. pp.389-394.

Wanninger, L. (1993) : *Effects of the Equatorial Ionosphere on GPS*, **GPS World**, Advanstar Communications, July 1993. pp.48-54.

Wells, D.E., N. Beck, D. Delikaraoglou, A. Kleusberg, E.J. Krakiwsky, G. Lachapelle, R.B. Langley, M. Nakiboglu, K.P. Schwarz, J.M. Tranquilla, P. Vanicek (1987) : **Guide to GPS Positioning**, Canadian GPS Associates, Fredericton, N.B.

White House (1996) : **U.S. Global Positioning Position Policy**, Presidential Decision Directive, March 26.

Zhang, G. (1995) : **A Low-Cost Integrated INS/GPS System**, M.Sc. Thesis, UCGE report 20078, Department of Geomatics Engineering, The University of Calgary, Alberta, Canada.

Zhang, Z. (1997) : **Impact of Rubidium Clock Aiding on GPS Augmented Vehicular Navigation**, M.Sc. Thesis, UCGE Report 200112, Department of Geomatics Engineering, The University of Calgary, Alberta, Canada.

## APPENDIX

### Derivation of Design Matrix for Single Point GPS Position and Velocity Calculation

In Chapter 6, a method is described for determining the vehicle position and velocity based on the monitor antenna pseudorange and Doppler measurements. Since both equation (3.1) for the pseudorange and equation (3.4) for the Doppler must be linearized, the design matrix  $\mathbf{H}_k$  is given by equation (2.18). The design matrix ( $\mathbf{H}_k$ ) was defined in Chapter 6 as a hypermatrix, repeated from equation (6.5) as

$$\mathbf{H} = \begin{bmatrix} \mathbf{H}_{11} & \vdots & \mathbf{0} \\ \dots & & \dots \\ \mathbf{H}_{21} & \vdots & \mathbf{H}_{22} \end{bmatrix} \quad (\text{A.1})$$

The submatrix  $\mathbf{0}$  is a  $m \times 4$  null matrix, where  $m$  is the number of satellites tracked.  $\mathbf{H}_{11}$  is a  $m \times 4$  matrix based on the pseudorange measurements while  $\mathbf{H}_{21}$  and  $\mathbf{H}_{22}$  are also  $m \times 4$  but based on the Doppler measurements. Linearizing equation (3.1) using equation (2.18) gives  $\mathbf{H}_{11}$  for the case of  $m$  pseudorange measurements

$$\mathbf{H}_{11} = \begin{bmatrix} -\frac{(x^1 - x_r)}{\mathbf{r}_r^1} & -\frac{(y^1 - y_r)}{\mathbf{r}_r^1} & -\frac{(z^1 - z_r)}{\mathbf{r}_r^1} & -1 \\ -\frac{(x^2 - x_r)}{\mathbf{r}_r^2} & -\frac{(y^2 - y_r)}{\mathbf{r}_r^2} & -\frac{(z^2 - z_r)}{\mathbf{r}_r^2} & -1 \\ \vdots & \vdots & \vdots & \vdots \\ -\frac{(x^m - x_r)}{\mathbf{r}_r^m} & -\frac{(y^m - y_r)}{\mathbf{r}_r^m} & -\frac{(z^m - z_r)}{\mathbf{r}_r^m} & -1 \end{bmatrix} \quad (\text{A.2})$$

where,  $\mathbf{r}_r^i$  is the distance from the receiver ( $r$ ) to the satellite ( $i$ ),  $(x^i, y^i, z^i)$  is the ECEF satellite position from the navigation message and  $(x_r, y_r, z_r)$  is the desired location of the

receiver. The case for the Doppler measurements is slightly more complicated. Taking the Doppler measurement equation and ignoring the states that are not estimated results in

$$\dot{\mathbf{f}}_r^i = \dot{\mathbf{r}}_r^i - cd\dot{T}_r \quad (\text{A.3})$$

where,  $\dot{\mathbf{f}}_r^i$  is the Doppler measurement from the receiver  $r$  to the satellite  $i$ , [m/s]

$\dot{\mathbf{r}}_r^i$  is the true rate of change of the range [m/s]

and  $cd\dot{T}_r$  is the receiver clock rate of change [m/s].

The range to the satellite is given in equation (3.2), repeated here for convenience

$$\mathbf{r}_r^i = \sqrt{(x^i - x_r)^2 + (y^i - y_r)^2 + (z^i - z_r)^2} \quad (\text{A.4})$$

where  $(x^i, y^i, z^i)$  is the position of the satellite given by the navigation message and  $(x_r, y_r, z_r)$  is the unknown position of the receiver in the Earth-centered, Earth-fixed (ECEF) Cartesian frame defined by WGS-84. The time derivative of the true range can then be written in terms of partial derivatives as

$$\dot{\mathbf{r}}_r^i = \frac{\partial \mathbf{r}_r^i}{\partial t} = \frac{\partial \mathbf{r}_r^i}{\partial x^i} \frac{\partial x^i}{\partial t} + \frac{\partial \mathbf{r}_r^i}{\partial y^i} \frac{\partial y^i}{\partial t} + \frac{\partial \mathbf{r}_r^i}{\partial z^i} \frac{\partial z^i}{\partial t} + \frac{\partial \mathbf{r}_r^i}{\partial x_r} \frac{\partial x_r}{\partial t} + \frac{\partial \mathbf{r}_r^i}{\partial y_r} \frac{\partial y_r}{\partial t} + \frac{\partial \mathbf{r}_r^i}{\partial z_r} \frac{\partial z_r}{\partial t} \quad (\text{A.5})$$

or rewriting the time derivatives of the satellite and receiver position coordinates

$$\dot{\mathbf{r}}_r^i = \frac{\partial \mathbf{r}_r^i}{\partial x^i} \dot{x}^i + \frac{\partial \mathbf{r}_r^i}{\partial y^i} \dot{y}^i + \frac{\partial \mathbf{r}_r^i}{\partial z^i} \dot{z}^i + \frac{\partial \mathbf{r}_r^i}{\partial x_r} \dot{x}_r + \frac{\partial \mathbf{r}_r^i}{\partial y_r} \dot{y}_r + \frac{\partial \mathbf{r}_r^i}{\partial z_r} \dot{z}_r \quad (\text{A.6})$$

where,  $(\dot{x}^i \ \dot{y}^i \ \dot{z}^i)$  is the vector of satellite velocities provided in the navigation message and  $(\dot{x}_r \ \dot{y}_r \ \dot{z}_r)$  is the vector of desired receiver velocities. An examination of equation (A.4) reveals that

$$\frac{\mathbf{f}_{\mathbf{r}_r^i}}{\mathbf{f}_{x^i}} = -\frac{\mathbf{f}_{\mathbf{r}_r^i}}{\mathbf{f}_{x_r}}, \quad \frac{\mathbf{f}_{\mathbf{r}_r^i}}{\mathbf{f}_{y^i}} = -\frac{\mathbf{f}_{\mathbf{r}_r^i}}{\mathbf{f}_{y_r}} \quad \text{and} \quad \frac{\mathbf{f}_{\mathbf{r}_r^i}}{\mathbf{f}_{z^i}} = -\frac{\mathbf{f}_{\mathbf{r}_r^i}}{\mathbf{f}_{z_r}}. \quad (\text{A.7})$$

Substitution of equation (A.7) into (A.6) followed by some rearranging of terms results in

$$\dot{\mathbf{r}}_r^i = \frac{\mathbf{f}_{\mathbf{r}_r^i}}{\mathbf{f}_{x_r}}(\dot{x}_r - \dot{x}^i) + \frac{\mathbf{f}_{\mathbf{r}_r^i}}{\mathbf{f}_{y_r}}(\dot{y}_r - \dot{y}^i) + \frac{\mathbf{f}_{\mathbf{r}_r^i}}{\mathbf{f}_{z_r}}(\dot{z}_r - \dot{z}^i). \quad (\text{A.8})$$

The Doppler measurement relation in equation (A.3) can then be rewritten using equation (A.8) as

$$\dot{\mathbf{f}}_r^i = \frac{\mathbf{f}_{\mathbf{r}_r^i}}{\mathbf{f}_{x_r}}(\dot{x}_r - \dot{x}^i) + \frac{\mathbf{f}_{\mathbf{r}_r^i}}{\mathbf{f}_{y_r}}(\dot{y}_r - \dot{y}^i) + \frac{\mathbf{f}_{\mathbf{r}_r^i}}{\mathbf{f}_{z_r}}(\dot{z}_r - \dot{z}^i) - cd\dot{T}_r. \quad (\text{A.9})$$

To obtain the design matrix for the Doppler measurements, equation (A.9) must be linearized with respect to the parameters found in equation (6.1), namely the receiver position, receiver velocity and receiver clock terms. Following equation (2.18) the design matrix for  $m$  measurements must be of the form

$$\mathbf{H} = [\mathbf{H}_{21} \quad \vdots \quad \mathbf{H}_{22}] = \begin{bmatrix} \frac{\mathbb{H}h_r^1}{\mathbb{H}x_r} & \frac{\mathbb{H}h_r^1}{\mathbb{H}y_r} & \frac{\mathbb{H}h_r^1}{\mathbb{H}z_r} & \frac{\mathbb{H}h_r^1}{\mathbb{H}cdT_r} & \frac{\mathbb{H}h_r^1}{\mathbb{H}\dot{x}_r} & \frac{\mathbb{H}h_r^1}{\mathbb{H}\dot{y}_r} & \frac{\mathbb{H}h_r^1}{\mathbb{H}\dot{z}_r} & \frac{\mathbb{H}h_r^1}{\mathbb{H}cd\dot{T}_r} \\ \frac{\mathbb{H}h_r^2}{\mathbb{H}x_r} & \frac{\mathbb{H}h_r^2}{\mathbb{H}y_r} & \frac{\mathbb{H}h_r^2}{\mathbb{H}z_r} & \frac{\mathbb{H}h_r^2}{\mathbb{H}cdT_r} & \frac{\mathbb{H}h_r^2}{\mathbb{H}\dot{x}_r} & \frac{\mathbb{H}h_r^2}{\mathbb{H}\dot{y}_r} & \frac{\mathbb{H}h_r^2}{\mathbb{H}\dot{z}_r} & \frac{\mathbb{H}h_r^2}{\mathbb{H}cd\dot{T}_r} \\ \vdots & \vdots \\ \frac{\mathbb{H}h_r^m}{\mathbb{H}x_r} & \frac{\mathbb{H}h_r^m}{\mathbb{H}y_r} & \frac{\mathbb{H}h_r^m}{\mathbb{H}z_r} & \frac{\mathbb{H}h_r^m}{\mathbb{H}cdT_r} & \frac{\mathbb{H}h_r^m}{\mathbb{H}\dot{x}_r} & \frac{\mathbb{H}h_r^m}{\mathbb{H}\dot{y}_r} & \frac{\mathbb{H}h_r^m}{\mathbb{H}\dot{z}_r} & \frac{\mathbb{H}h_r^m}{\mathbb{H}cd\dot{T}_r} \end{bmatrix} \quad (\text{A.10})$$

where,  $h_r^i$  is the function defined in equation (A.9) for the receiver  $r$  and satellite  $i$ . The derivative of  $h$  with respect to the receiver clock offset terms is given by

$$\frac{\mathbb{H}h_r^i}{\mathbb{H}cdT_r} = 0, \quad \frac{\mathbb{H}h_r^i}{\mathbb{H}cd\dot{T}_r} = -1. \quad (\text{A.11})$$

The remaining terms are given as

$$\frac{\mathbb{H}h_r^i}{\mathbb{H}x_r} = \frac{\mathbb{H}^2 \mathbf{r}_r^i}{\mathbb{H}x_r^2} (\dot{x}_r - \dot{x}^i) + \frac{\mathbb{H}^2 \mathbf{r}_r^i}{\mathbb{H}x_r \mathbb{H}y_r} (\dot{y}_r - \dot{y}^i) + \frac{\mathbb{H}^2 \mathbf{r}_r^i}{\mathbb{H}x_r \mathbb{H}z_r} (\dot{z}_r - \dot{z}^i)$$

$$\frac{\mathbb{H}h_r^i}{\mathbb{H}y_r} = \frac{\mathbb{H}^2 \mathbf{r}_r^i}{\mathbb{H}x_r \mathbb{H}y_r} (\dot{x}_r - \dot{x}^i) + \frac{\mathbb{H}^2 \mathbf{r}_r^i}{\mathbb{H}y_r^2} (\dot{y}_r - \dot{y}^i) + \frac{\mathbb{H}^2 \mathbf{r}_r^i}{\mathbb{H}y_r \mathbb{H}z_r} (\dot{z}_r - \dot{z}^i)$$

$$\frac{\mathbb{H}h_r^i}{\mathbb{H}z_r} = \frac{\mathbb{H}^2 \mathbf{r}_r^i}{\mathbb{H}x_r \mathbb{H}z_r} (\dot{x}_r - \dot{x}^i) + \frac{\mathbb{H}^2 \mathbf{r}_r^i}{\mathbb{H}y_r \mathbb{H}z_r} (\dot{y}_r - \dot{y}^i) + \frac{\mathbb{H}^2 \mathbf{r}_r^i}{\mathbb{H}z_r^2} (\dot{z}_r - \dot{z}^i)$$

$$\frac{\mathbb{H}h_r^i}{\mathbb{H}\dot{x}_r} = \frac{\mathbb{H}\mathbf{r}_r^i}{\mathbb{H}\dot{x}_r}$$

$$\frac{\mathbb{H}h_r^i}{\mathbb{H}\dot{y}_r} = \frac{\mathbb{H}\mathbf{r}_r^i}{\mathbb{H}\dot{y}_r}$$

$$\frac{\mathbb{H}h_r^i}{\mathbb{H}\dot{z}_r} = \frac{\mathbb{H}\mathbf{r}_r^i}{\mathbb{H}\dot{z}_r}$$

where,

$$\frac{\mathfrak{I}^2 \mathbf{r}_r^i}{\mathfrak{I}x_r^2} = \frac{1}{\mathbf{r}_r^i} - \frac{(x_r - x^i)^2}{(\mathbf{r}_r^i)^3}$$

$$\frac{\mathfrak{I}^2 \mathbf{r}_r^i}{\mathfrak{I}y_r^2} = \frac{1}{\mathbf{r}_r^i} - \frac{(y_r - y^i)^2}{(\mathbf{r}_r^i)^3}$$

$$\frac{\mathfrak{I}^2 \mathbf{r}_r^i}{\mathfrak{I}z_r^2} = \frac{1}{\mathbf{r}_r^i} - \frac{(z_r - z^i)^2}{(\mathbf{r}_r^i)^3}$$

$$\frac{\mathfrak{I}^2 \mathbf{r}_r^i}{\mathfrak{I}x_r \mathfrak{I}y_r} = -\frac{(x_r - x^i)(y_r - y^i)}{(\mathbf{r}_r^i)^3}$$

$$\frac{\mathfrak{I}^2 \mathbf{r}_r^i}{\mathfrak{I}x_r \mathfrak{I}z_r} = -\frac{(x_r - x^i)(z_r - z^i)}{(\mathbf{r}_r^i)^3}$$

$$\frac{\mathfrak{I}^2 \mathbf{r}_r^i}{\mathfrak{I}y_r \mathfrak{I}z_r} = -\frac{(y_r - y^i)(z_r - z^i)}{(\mathbf{r}_r^i)^3}.$$